Study of interface evolution between two immiscible fluids due to a time periodic electric field in a microfluidic channel

Manik Mayur

N° d'ordre: 4947

THESIS

SUBMITTED TO

UNIVERSITÉ BORDEAUX I

ÉCOLE DOCTORALE
DES SCIENCES PHYSIQUES ET DE L'INGÉNIEUR

by **Manik MAYUR**

TO OBTAIN THE DEGREE OF

DOCTOR OF PHILOSOPHY

SPECIALITY : MECHANICAL ENGINEERING

STUDY OF INTERFACE EVOLUTION BETWEEN TWO IMMISCIBLE FLUIDS DUE TO A TIME PERIODIC ELECTRIC FIELD IN A MICROFLUIDIC CHANNEL

ON

9th of DECEMBER 2013

Graduation Committee:

Dr.	S. Colin, Professor, INSA Toulouse	Reporter
Dr.	M. Bestehorn, Professor, BTU Cottbus	Reporter
Dr.	A. Colin, Professor, Université Bordeaux 1	Examiner
Dr.	F. Zoueshtiagh, Associate Professor, Université Lille 1	Examiner
Dr.	S. Amiroudine, Professor, Université Bordeaux 1	Thesis Director
Dr.	D. Lasseux, CNRS Research Scientist, I2M	Thesis Co-Director

– 2013 –

Dedicated to my parents

Résumé

Les écoulements multiphasiques dans les systèmes microfluidiques ont récemment trouvé de nombreuses applications dans des domaines tels que le traitement biochimique (par exemple les réacteurs dans des puces, les mélangeurs, l'extraction de l'ADN, et administration de médicaments), ou l'extraction de pétrole à partir de formations rocheuses poreuses. Une des caractéristiques de ces écoulements microfluidiques est sa grande surface par rapport au volume, ce qui met en évidence, de façon significative, le rôle des interfaces multiphasiques dans cette dynamique. Les interfaces entre les phases peuvent être définies comme des surfaces continues, perpendiculairement auxquelles il y a une transition nette des propriétés intensives d'une phase à l'autre. Ces interfaces peuvent être classées en grande partie par la nature des phases en interaction tels que le gaz-liquide, le liquide-liquide ou le liquide-solide. La présence de ces interfaces apporte la possibilité de transport de la phase passive par cisaillement à l'interface. Ces mécanismes de transport sont actuellement explorés en détail pour les problèmes de transport aux micro-nano échelles. L'un des principaux défis dans les phénomènes de transport à la micro-échelle est d'avoir un actionnement fiable du débit. Le mécanisme d'actionnement d'écoulement le plus couramment utilisé dans des dispositifs à micro-échelle est de créer un gradient de pression en utilisant une pompe. Ces dispositifs sont volumineux avec une utilisation des pièces en mouvement pour créer un écoulement, et nécessitent donc un entretien fréquent. Au cours de la dernière décennie, l'utilisation de l'électrocinétique grâce à un champ électrique appliqué aux bornes du micro-canal est un mécanisme de génération d'écoulement de plus en plus populaire. Ce type d'écoulement est réalisé grâce aux interactions entre une couche de paroi adhésive chargée électriquement (également connu sous le nom de double couche électrique) et d'un champ électrique appliqué aux bornes du micro-canal, écoulement qualifié d'électroosmotique (EO). Ce type de mécanisme a un avantage durable par rapport aux pompes puisqu'ils ne nécessitent pas de composants mobiles. Les écoulements électroosmotiques dans des micro-canaux ayant un potentiel électrique axialement invariant ont typiquement un profil de vitesse quasi-uniforme (écoulement dit de « bouchon »), ce qui réduit la possibilité de dispersion de l'espèce transportée et par conséquent, peuvent se révéler efficaces pour le transport d'espèces biologiques dans ces micro-canaux. On considère en général un champ électrique constant, mais il entraîne des réactions électrochimiques aux électrodes (phénomène d'électrolyse non souhaitée pour certaines expériences puisque cela entraîne des fluctuations au niveau du débit d'écoulement et peut parfois arrêter l'écoulement tout en en isolant complètement l'électrode). Un autre problème associé aux réactions électrochim-

iques au niveau des électrodes est la variation de pH dans les réservoirs où sont posées les électrodes. Un tel phénomène crée un gradient de pH dans le canal affectant l'électrochimie du système et peut éventuellement affecter la mobilité des ions dans le liquide. Des études antérieures ont montré que l'utilisation d'un champ électrique oscillatoire contribue à diminuer les réactions chimiques au niveau des électrodes avec un contrôle spatio-temporel effectif sur l'écoulement de liquide et du mélange. Un tel utilitaire d'écoulement électroosmotique oscillatoire a conduit à de nombreuses études récentes dont, entre autres, l'actionnement de l'écoulement, le stockage de l'énergie, etc... Bien que l'écoulement électroosmotique a été prouvé être le mécanisme le plus pratique pour le transport des liquides dans des microcanaux, un des inconvénients pour son utilisation dans les applications habituelles vient du fait que ce liquide transporté doit être électriquement conducteur. Pour le transport d'un liquide non-conducteur on le fait généralement à l'aide d'un liquide immiscible conducteur par cisaillement à l'interface fluide-fluide. L'étude des systèmes électroosmotiques à deux phases, tels que les systèmes air-eau a mis en évidence le rôle des charges à l'interface sur le profil de vitesse (vitesses différentes à l'interface et dans le cœur du fluide), une fonctionnalité qui est inattendu dans un EO classique. Un tel profil de vitesse très dispersif peut affecter le transport des espèces par EO. Les études mentionnées ont été réalisées entre deux couches de fluide tout en tenant compte des conditions classiques à l'interface telles que la continuité de la vitesse et de la contrainte de cisaillement à cette interface fluide-fluide. La présence d'une interface liquide-liquide dans un EO nécessite la caractérisation des paramètres responsables de l'instabilité de tels systèmes, dont il faudra trouver la solution de l'état de base du système non perturbé. La modélisation d'un tel système n'est pas triviale et comporte quelques subtilités attribuées à l'existence des tensions de Maxwell à l'interface qui changent les conditions aux limites de cette dernière. Ceci est en contraste avec les écoulements dans des canaux entre deux parois rigides pour lesquelles on impose une condition à la limite de vitesse (généralement pas de glissement sur les parois) indépendamment de toute considération sur les tensions de Maxwell. En outre, dans le cas d'un écoulement symétrique entre deux parois rigides, les contraintes hydrodynamique et de Maxwell sont individuellement nuls à la ligne de symétrie. Cependant, pour un écoulement à surface libre, c'est la contrainte totale (hydrodynamique et Maxwell) qui doit être nulle à l'interface. Dans la plupart des micro-dispositifs, l'utilisation du champ électrique pour le transport de fluides est limitée par la nature non-conductrice d'un grand nombre de fluides (par exemple, les liquides biologiques, les liquides polymériques...). En outre, le comportement d'un tel système lorsqu'il rencontre une discontinuité sous la forme d'une interface est encore sous-explorée. L'un des principaux défis dans la dynamique du film est de comprendre et de modéliser le seuil de stabilité de l'interface sous l'influence d'un large éventail de phénomènes physiques inhérents à ce système comme la tension superficielle, la viscosité, les forces de van der Waals et des phénomènes statiques ou dépendants du temps comme la gravité, les gradients de température et les champs électriques. Une analyse détaillée et globale est par conséquent nécessaire, ce qui constitue l'objet de cette thèse.

Le travail présenté dans cette thèse se concentre sur le rôle des tensions de Maxwell constant et dépendant du temps, des forces capillaires et de la pression de disjonction sur la stabilité de l'interface. Afin d'étudier l'effet des tensions de Maxwell à l'interface dans des configurations classiques à plaques planes parallèles ainsi que pour des configurations réalistes de canaux rectangulaires, la solution d'un EO à surface libre a été obtenue analytiquement. En prenant en compte une expression complète de la condition limite à la surface libre qui inclut les tensions de Maxwell à cette interface, une analyse paramétrique de l'écoulement en termes de l'épaisseur de la double couche électrique, du rapport de forme du canal et des différentes valeurs du potentiel zêta « fluide – fluide » et « solide – liquide » a été entreprise. Grâce au champ de vitesse 2D, il a été montré que les parois ont un effet significatif sur la distribution des vitesses dans un micro-canal rectangulaire. Les paramètres de contrôle de l'écoulement dans un EO sont, non seulement les propriétés électrochimiques des électrolytes qui contrôlent l'épaisseur de la double couche électrique et les valeurs des potentiels zêta au mur et à l'interface, mais aussi la géométrie du canal à travers son rapport de forme. Une telle étude permet d'identifier les paramètres appropriés pour imposer un débit d'écoulement et une distribution des vitesses souhaitée dans un dispositif microfluidique. Une analyse de stabilité linéaire basée sur une perturbation à l'interface a été réalisée pour un film mince d'électrolyte sous des champs électriques continus (constants) et alternatifs (dépendant du temps). Une analyse asymptotique avec une hypothèse de grande longueur d'onde des équations d'Orr-Sommerfeld a été appliquée afin de déterminer les seuils de stabilité paramétriques d'un film mince aqueux. L'accent a été mis sur les effets de la tension de surface, de la pression de disjonction pour l'interaction gaz-liquide-substrat, de l'amplitude et de la fréquence du champ électrique appliqué, ainsi que du potentiel zêta du substrat et de la surface libre. En outre, un dispositif expérimental a été conçu et monté afin de caractériser l'écoulement électroosmotique dans un micro-canal rectangulaire. Avec l'aide d'une analyse PTV (« Particle Tracking Velocimetry »), les distributions de vitesse ont été obtenues et comparées aux prédictions théoriques. Cette comparaison a permis d'estimer le potentiel zêta du PDMS utilisé, valeur conforme à la valeur indiquée dans la littérature. En outre, afin d'étudier l'instabilité de l'interface liquide-liquide sous champ électrique périodique en temps, deux cas ont été considérés : le premier cas correspondait à deux fluides miscibles et le second à deux fluides immiscibles.

Une analyse comparative des profils de vitesse de l'état de base avec et sans contraintes de Maxwell à l'interface, a montré que les gradients de vitesse étaient importants à l'interface liquide-liquide avec les contraintes de Maxwell. De tels gradients sont essentiels à l'instabilité interfaciale sous l'action d'un champ électrique périodique car ils peuvent atténuer ou amplifier les ondes à l'interface. L'influence du cœur du fluide à partir des oscillations proches paroi est inversement proportionnelle à la fréquence d'excitation. A de basses fréquences, la dispersion du champ de vitesse s'affaiblit et tend vers le champ de vitesse classique dans un écoulement électroosmotique continu. Par la variation de la polarité à l'interface on a constaté que, non

seulement on peut contrôler la vitesse à l'interface ainsi que le taux de cisaillement, mais également établir une différence de phase significative de la vitesse du fluide en différents emplacements transversaux dans le fluide. Ceci a pour conséquences d'augmenter les effets de dispersion du champ de vitesse et peut être effectivement utilisé dans le transport contrôlé des espèces dans des dispositifs microfluidiques. (a) Les paramètres avec un effet stabilisateur sur la dynamique du film sont la tension de surface, la pression de disjonction répulsive ($A < 0$), la pression osmotique due à la double couche électrique aux interfaces et la dissipation visqueuse. (b) Les phénomènes qui contribuent à l'instabilité du film sont la pression de disjonction attractive ($A > 0$), des doubles couches électriques plus minces (nombre de Debye $De << 1$), du champ électrique externe conduisant à l'écoulement électroosmotique et des basses fréquences. La stabilité du film décroît lorsqu'on augmente l'amplitude du champ électrique appliqué et qui est dû à une augmentation des tensions de Maxwell à l'interface. (c) Lorsque la valeur du potentiel zêta du substrat augmente l'écoulement tend à se stabiliser et la composante osmotique de la pression augmente. (d) Dans le cas des fluides miscibles, l'objectif était d'étudier la déformation de l'interface liquide-liquide soumise à un EO périodique dans le temps et en présence des transports convectif et diffusif. Pour obtenir une interface plane (non perturbée) avec une diffusion limitée de ces liquides miscibles, un débit a été imposé au niveau des deux liquides de sorte que ce flux de convection peut atténuer le mélange des deux liquides par diffusion interfaciale. Le débit imposé était pris identique dans les deux liquides. Il a été observé que pour une valeur donnée du champ électrique appliqué, l'amplitude des déformations à l'interface diminuait avec l'augmentation du débit imposé, ce qui détermine l'effet stabilisant de la vitesse d'écoulement imposée. En outre, il a également été observé que la réactivité de l'interface (c'est à dire l'amplitude de l'interface perturbée) à la fréquence du champ électrique appliqué, était la plus sensible dans la gamme de 1-5Hz. (e) Dans le cas des fluides non miscibles, l'objectif était d'étudier la déformation de l'interface liquide-liquide sous un EO périodique dans le temps et en présence de la force capillaire et du transport convectif. Pour obtenir une interface plane (non-perturbée) contre la force capillaire à l'interface, un débit a été imposé au niveau des liquides pour contrer les instabilités de ces forces de tension de surface à l'origine de la génération des bulles. On a observé qu'il existait une valeur critique du débit d'écoulement au-dessus de laquelle le système reste stable pour la gamme des valeurs du champ électrique appliqué. Cela suggère l'existence d'une compétition dynamique entre l'inertie convective et les contraintes de Maxwell. Pour une valeur donnée de débit d'écoulement, la stabilité du système diminue lors de l'augmentation de l'amplitude du champ électrique. Enfin, il a été observé que les hautes fréquences du champ électrique tendent à stabiliser l'écoulement à un débit donné.

Mots-clés: écoulement électroosmotique, microfluidique, analyse de stabilité linéaire, analyse en grande longueur d'onde, expériences en fluides miscibles/immiscibles.

Acknowledgments

My doctoral journey over the past three years at Bordeaux has been a very enriching journey for me both on professional and personal levels. This journey wouldn't have begun without my acceptance into the PhD project, which was a brainchild of Prof. Sakir Amiroudine and Prof. Suman Chakraborty. I express my sincerest gratitude to Prof. Amiroudine and Dr. Didier Lasseux for believing in my abilities to carry out such a detailed project which contained both theoretical and experimental investigations and was completely new and challenging to all of us.

I came to France with two big bags, the first one full of Indian spices, and the second one full of apprehensions regarding my survival in a completely different culture, lifestyle and language. Now, after a time span of three years, when I look back in time, I can not imagine how many amazing people I have met during my journey and how each one of them made my stay equally memorable. I was specially overwhelmed by the warmth and convivial nature of each and every individual that I met in the laboratoire I2M-TREFLE. It was because of the tireless efforts of Muriel, Sylviane, Fred, Marian, Audrey and Alain at ENSAM, and Valerie and Noemie at ENSCBP that I cruised through all the toilsome and non-trivial administrative procedures. As much as I wanted to learn about the French culture and language, the lesson started right from the very first day when I met Baptiste as my roommate. It was he who acted as my interpreter and translator during all the necessary administrative visits in the first few months. Then, I was proudly welcomed in the Francky family (Francky, Sandra, and Flavio) to whom I would like to dedicate all the weekends that I can not to remember anymore. I just have realized that during my entire stay at Bordeaux, I was really lucky to share moments and experiences with so many wonderful people that recounting each and every such moment would surpasse the size of my PhD thesis. Specially, I can not forget all the lunches and motivating discussions together with the Postdocs and PhD students of the TREFLE family, namely, Erik, Vlad, Mario, Nisrine, Essam, Carolina, Andrea, Christophe, Cecile, Elvire, Marie, Alex, Fouzia, Stephanie, Antonio, Mehrez, Tan, Xabi, and Jose. Moreover, it will be really difficult to forget the Friday evening drinks and dinners at FUFU with Alex, Clementine, Louiza, Antoine, Florent, and Nastaran.

I would also like to express my sincerest gratitude to Prof. Annie Colin, Julien, David, Virginie, Pierre, Hughes, Laetitia and the rest of the entire staff of the Laboratory of Future for helping me with the fabrication of my microchips and finding time out of their busy schedules to discuss my experimental issues and making sure that I always go home with a solution.

My thesis could not have achieved its current state of closure without the support of Julien Monteil from CBMN who accommodated my entire experimental setup in his laboratory and allowed me to use the phase contrast microscope of the lab.

At the very last but not the least, I like to thank all the members of Tir à l'arc de Bégles for welcoming me to their club and helping me learn archery. I would specially like to thank Cédric, Gilles, Yasmina, Laure and Chloé for giving me confidence and encouragement time to time, and for all the nice moments that we spent together.

Nomenclature

Roman Symbols

$\mathbf{I}$	Ionic charge density vector	
$\mathbf{U}$	Dimensionless velocity vector	
$\mathbf{u}$	velocity vector	
$\mathbf{D}$	Electric displacement field vector	
$\mathbf{E}$	Electric field vector	
$\mathbf{i}$	unit vector in x direction	
$\mathbf{J}$	Flux vector	
$\mathbf{j}$	unit vector in y direction	
$\mathbf{R}$	Dimensionless position vector	
$\mathbf{r}$	Position vector	
A	Dimensionless Hamaker constant	$\frac{a}{2\pi h_{ref}^2 \mu u_{ref}}$
a	Hamaker constant	
Ca	Capillary number	$\frac{\mu u_{ref}}{\gamma}$
De	Debye number	$\frac{\lambda_D}{h_{ref}}$
E_R	Electric field ratio	$\frac{\zeta_{ref}}{E_{app} h_{ref}}$
p	Hydrostatic pressure	
Q	Dimensionless flow rate	
Re	Reynolds number	$\frac{\rho u_{ref} h_{ref}}{\mu}$
u_{HS}	Helmholtz-Smoluchowski velocity	$-\frac{\varepsilon_r \varepsilon_0 \zeta_b E_{app}}{\mu}$

U	Dimensionless velocity in x-direction
u	Velocity in x-direction
v	Velocity in y-direction
Wo	Womersley number ..... $\sqrt{\frac{\omega h_{ref}^2}{\nu}}$
X	Dimensionless x direction
x	x direction
Y	Dimensionless y direction
Z_R	Zeta potential ratio ..... $\frac{\zeta_I}{\zeta_{ref}}$
Z	Dimensionless z direction
c_i	Concentration of the i-th ionic species
D	Coefficient of Diffusion
F	Faraday's constant
f	Frequency
h	Height
K	Bulk modulus
M	Molar Mobility
R	Universal Gas Constant
r	reactive term
T	Ambient temperature
y	y direction
z	z direction
z_i	Valence of i-th ionic species
$\underline{\underline{\mathbf{D}}}$	Strain rate tensor
$\underline{\underline{\mathbf{I}}}$	Identity tensor
k_B	Boltzmann constant

Abbreviations

AC	Alternating Current
DC	Direct Current
DLVO	Derjaguin, Landau, Verwey and Overbeek
EDL	Electric Double Layer
EOF	Electro-Osmotic Flow
GCS	Gouy-Chapman-Stern
PIV	Particle Image Velocimetry
PTV	Particle Tracking Velocimetry

Greek Symbols

α	Wave number
$\bar{\rho}_e$	Dimensionless charge density
β	Ionic energy parameter ..... $\frac{ez\zeta_{ref}}{k_B T}$
δ	Diffusion length
γ_R	Electro-viscous number ..... $\frac{\varepsilon_r \varepsilon_0 \zeta_{ref} E_{app}}{\mu u_{ref}}$
κ	Curvature
Λ	Surface conductivity
λ	Lamé's first parameter
λ_D	Debye length ..... $\sqrt{\frac{\varepsilon_r \varepsilon_0 k_B T}{2F^2 z^2 c_0}}$
μ	Coefficient of dynamic viscosity
μ_i	Chemical potential of the i-th ionic species
ν	Coefficient of kinematic viscosity
ω	Angular frequency
ω_{abs}	Magnitude of vorticity
Φ	Dimensionless scalar potential

ϕ	Scalar potential
Π	Dimensionless disjoining pressure
Ψ	Dimensionless stream function
ψ	Stream function
ρ	Density
σ	Growth rate
τ	Time period
Θ	Dimensionless time
θ	Time
$\underline{\underline{\mathbf{\Sigma^H}}}$	Hydrodynamic stress tensor
$\underline{\underline{\mathbf{\Sigma^M}}}$	Maxwell stress tensor
$\underline{\underline{\mathbf{\Sigma^T}}}$	Total stress tensor
$\underline{\underline{\tau}}$	Viscous shear stress tensor
ε	permittivity
ζ	Zeta potential

Subscripts

app	Applied
b	Base
C	Convective component
D	Diffusive component
E	Electromigration component
e	Charge
I	Interface
i	i-th species
m	Molar

ref	Reference
r	relative
sc	Space charge
s	Surface
+	Positive ions
-	Negative ions
0	Initial state

Mathematical Symbols

cosh	Hyperbolic cosine
sech	Hyperbolic secant
sinh	Hyperbolic sine
tanh	Hyperbolic tangent

Contents

Part I.

Introduction to Electrokinetics

1. General Introduction

1.1. Motivation and Overview

Multi-phase flows in micro-scale systems have recently found numerous applications in a wide range of fields like bio-chemical processing such as, lab-on-a-chip reactors [Deshmukh and Vlachos (2005)], mixers [Campbell and Grzybowski (2004)], DNA extraction [Ugaz et al. (2004)], and drug delivery [Squires et al. (2008)], to oil extraction from porous rock formations Zhang et al. (2006). One of the significant characteristics of micro-scale flows is high surface to volume ratio, which significantly highlights the role of multi-phase interfaces in such dynamics. Interfaces between phases can be broadly defined as continuous surfaces, normal to which there is a sharp transition of the intensive properties of one phase to another. Such interfaces can be largely categorized by the nature of the interacting phases such as gas-liquid, liquid-liquid and liquid-solid interfaces. Although within the scope of the present study, the solid interfaces are considered to be rigid and non-compliant. Within the scope of hydrodynamics, such confining solid surfaces provide boundary conditions on velocity slip and permeability (source or sink). Within the scope of electrodynamics, they either act as constant electric potential surfaces or polarizable dielectrics (see Chapter 2). Gas-liquid and liquid-liquid interfaces, within the purview of hydrodynamics are shear free and deformable interfaces. Electrodynamically, they are considered as charge storing interfaces, showing compliant dynamics under an applied electric field.

One of the major challenges in microscale transport phenomena is to have a reliable flow actuation. The most commonly used flow actuation mechanism in micro devices is by creating a pressure gradient using a pumping device. Such devices are bulky, use moving parts to create flow, and need frequent maintenance. During the past decade, use of electrokinetics as a flow actuating mechanism is microdevices is becoming more popular. Flow actuation in microchannels due to an externally applied electric field has found remarkable applications in lab-on-a-chip based microfluidics devices and systems [Stone et al. (2004); Sounart and Baygents (2007); Xu et al. (2011); Squires and Quake (2005); Bazant et al. (2004); Sheng and Wen (2012); Lee and Li (2006)]. Such flows are effectively realised by interactions between a wall-adhering charged layer (also known as the electrical double layer) and an externally applied electrical field, resulting in so-called Electro-Osmotic Flow (EOF) (see Chapter 2), which have an enduring advantage over classical fluidic pumps in a sense that these do not require any moving components. Electro-osmotic flows in microchan-

nels with axially-invariant interfacial potential typically have plug like (uniform) velocity profile which reduces the possibility of species dispersion and hence, may turn out to be effective for the transport of biological species in micro-devices. The most common form of EOF actuation is by a constant electrical field, but it has some inherent problems due to electrochemical reactions at the electrodes. Such problems include formation of Hydrogen and Oxygen bubbles due to the hydrolysis of water, which leads to fluctuations in the flow rate in microfluidic devices and sometimes eventually stops the flow altogether by insulating the electrode [Schaeper and Sepaniak (2000)].

Another problem associated with electrochemical reactions at the electrodes is the change of pH at electrode reservoirs [Persat et al. (2009b)]. Such a phenomenon creates a pH gradient in the channel affecting the electro-chemistry of the system and eventually affecting the mobility of ions in the liquid. Some previous studies have shown that the use of time periodic (AC) EOF is instrumental in diminishing the Faradaic reactions at the electrodes and to achieve effective spatio-temporal control over liquid flow and mixing [Shin et al. (2005); Chakraborty and Srivastava (2007); Chakraborty and Ray (2008); Dutta and Beskok (2001)]. Such a utility of AC EOF has led to recent increase in the studies exploring various novel applications of AC EOF including flow actuation [Ramos et al. (2005); Green et al. (2000); Gonzalez et al. (2000); Ramos et al. (1999); Bose et al. (2012); Chakraborty et al. (2012)], energy storage [Takami et al. (2002); Jang et al. (2005); Kötz (2000)] etc.

Although EOF has been proven to be the preferred mechanism for liquid transport in microchannels, one of the biggest shortcomings of its usage in mainstream applications comes from its basic requirement of the concerned liquid to be electrically conductive. There have been some attempts towards the transport of non-conductive liquid with the help of an immiscible conductive liquid through shear transfer at the fluid-fluid interface [Lee and Li (2006); Gao et al. (2005b); Haiwang et al. (2010); Lee et al. (2006); Pascall and Squires (2011)]. The study of two-phase electro-osmotic systems such as air-water systems has highlighted the role of interfacial charges on the velocity profile [Gao et al. (2005a)] such as different interfacial and bulk velocities, a feature that is unexpected in a classical EOF. Such a highly dispersive velocity profile can affect the species transport using EOF [Griffiths and Nilson (2006)]. The mentioned studies have been performed in two-layer EOF while considering classical interface matching conditions such as continuity of the velocity and hydrodynamic shear stress at the fluid-fluid interface. The presence of a fluid-fluid interface in an EOF necessitates the characterization of the parameters responsible for instability of such systems, for which one has to ascertain the basic or unperturbed state solution of the system. This is characterized by several intricacies, the modeling of which is not trivial. Those intricacies are attributed to the existence of an interface on which appropriate considerations on Maxwell stress need to be invoked [Choi et al. (2010); Mayur et al. (2012)]. This is in sharp contrast with flows in between rigid boundaries for which one imposes a velocity boundary condition (typically no slip at the walls) irrespective of any consideration on Maxwell stress. Moreover, in case

of a symmetric flow between two rigid boundaries, the hydrodynamic stress and the Maxwell stress individually become necessarily zero at the centerline (because of the centerline symmetry). However, for free surface flow, the total stress (hydrodynamic and Maxwell) at a flat interface needs to be zero.

In most of the micro-devices, the use of electrical field for fluid transport is limited by the non-conductive nature of a large group of fluids (for example, several biological liquids and polymeric liquids). Also, the behavior of such a system when it encounters a material discontinuity in the form of an interface is still under-explored. One of the major challenges in the film dynamics is to understand and model their interfacial evolution and stability thresholds under the influence of a wide range of inherent phenomena like surface tension, viscosity, van der Waals forces and imposed static and time-dependent phenomena like gravity, temperature gradients and electric fields. Although, reviews by Oron and Bankoff (1997) and Craster and Matar (2009) provide comprehensive details on the contribution of various physical phenomena towards film dynamics by providing a generalized evolution equation of the film thickness, owing to a complex interaction of the mentioned phenomena, a detailed and all-inclusive analysis is required, which is not easy and still awaited.

The objective of this thesis is to explore the EOF actuated interfacial dynamics in a two fluid system with the help of analytical models and experiemental investigations. A short overview of the included chapters is presented below,

Chapter 2 discusses the basic principle of an EOF in an aqueous electrolyte. It also discusses the origin of hydrodynamic and electrodynamic boundary conditions at solid-liquid and liquid-liquid interfaces.

Chapter 3 discusses the application of the basic concepts developed in Chapter 2 towards understanding the dynamics of a thin aqueous electrolytic film under the influence of DC and AC electric fields. Further, the role of interfacial Maxwell stress on flow control in a free surface flow of an electrolyte in a rectangular microchannel is discussed.

Chapter 4 discusses the stability of a thin electrolytic film under DC and AC electric fields using linear stability analysis for long wave disturbances while also focusing on the roles of capillary effects and disjoining pressure on film stability.

Chapter 5 discusses the experimental setup leading to one-fluid and two-fluid EOF in microchannels while also focusing on the microchannel fabrication using soft lithography techniques and a short discussion on the apparatus used.

Chapter 6 discusses the experimental observations and results for a EOF validation step and interfacial instabilities in miscible and immiscible fluids case. The EOF validation step involved estimation of the EOF parameters from a velocity field which was obtained by the help of Particle Tracking Velocimetry technique.

Chapter 7 discusses the conclusion and the perpectives of this thesis.

1.2. Publications from this project

1.2.1. Peer-reviewed Journals

[1] M. Mayur, S. Amiroudine, D. Lasseux, "Free-surface instability in electro-osmotic flows of ultrathin liquid films", Phys. Rev. E 2012, 85, pp. 046301.

[2] M. Mayur, S. Amiroudine, D. Lasseux, S. Chakraborty, "Maxwell stress-induced flow control of a free surface electro-osmotic flow in a rectangular microchannel", Microfluid. Nanofluid. 2013, DOI: 10.1007/s10404-013-1262-1.

[3] M. Mayur, S. Amiroudine, D. Lasseux, S. Chakraborty, "Effect of interfacial Maxwell stress on time periodic electro-osmotic flow in a thin liquid film with a flat interface", Electrophoresis, 2013, DOI: 10.1002/elps.201300236.

1.2.2. Conference Proceedings

[1] M. Mayur, S. Amiroudine, D. Lasseux, "Effect of interfacial potential and Maxwell stress on free surface electro-osmotic flow in a rectangular microchannel", ICREA 2012 Symposium "Nanofluidics, Colloids and Membranes", Barcelona, Spain (16-18th July, 2012).

[2] M. Mayur, S. Amiroudine, D. Lasseux, S. Chakraborty, "Effect of Maxwell stress on electro-osmotic flow of two immiscible fluids in a rectangular microchannel", 3rd European Conference on Microfluidics, Heidelberg, Germany (3-5th December, 2012).

2. Electro-Osmotic Flow and Interfacial Electro-hydrodynamics

2.1. Overview

Different states of matter like solid, liquid and gas respond differently under an externally applied electric field. Based on their responses, they can be broadly classified into conductors and insulators (dielectrics). The conductors have charges that are free to move under the applied electric field. In dielectrics, the charges that are bound to the constituting atoms or molecules, can only be displaced (translated or rotated) microscopically around the bounding atom or molecule under the influence of the external electric field. This spatial separation of bound charges is also called the "polarization" of charges. Some of the dielectrics show this polarization under the influence of an external electric field while others (for e.g. water), owing to their molecular structure have resident polarization and are called "polar molecules". It is because of this property that water can dissolve a large number of ionic compounds and polar non-ionic compounds. Such compounds dissociate into their constituent ions in the aqueous phase and are surrounded by the polar water molecules due to the Coulombic forces (see Fig. 2.1). This process is also called "hydration" when the solvent is water or "solvation" for any other polar solvent. Such ions under the influence of an external electric field are free to move within the solvent medium and can conduct electric current. Another very interesting aspect of such solvated mobile ions is that they can drag around the surrounding solvent molecules creating a bulk flow within the solvent. The catch, however, is that such solutions are electrically neutral, i.e. the concentrations of cations (positively charges ions) and anions (negatively charged ions) are the same. Hence, on assuming very small difference in the transport properties of involved cations and anions, the net solvent motion stands canceled. On the other hand, it is observed that when such an ionic solution is brought into contact with a chemically active solid substrate or encounters a material discontinuity in the terms of a fluid-fluid interface, a highly localized "charge separation" occurs near that interface which can extend over a scale of tens of nanometers. This structure has finite charge, which under the influence of an external electric field results into a near wall slip velocity, creating a highly non-dispersive plug flow in the bulk of the electrolyte. Such a flow of the bulk solution due to the charge

separation near the interfaces is called electro-osmotic flow (EOF). Such a system is being used extensively in microfluidic devices owing to its simple, low maintenance and non-dispersive flow actuation. This chapter details the exact mechanism of the mentioned phenomena with the help of thermodynamic and transport equations. This chapter revisits the interfacial boundary conditions with regards to the classical laws of hydrodynamics and the classical laws of electrodynamics. The boundary conditions developed in this chapter are developed with a general purview, which are used either in their entirety or within various approximations in the following chapters.

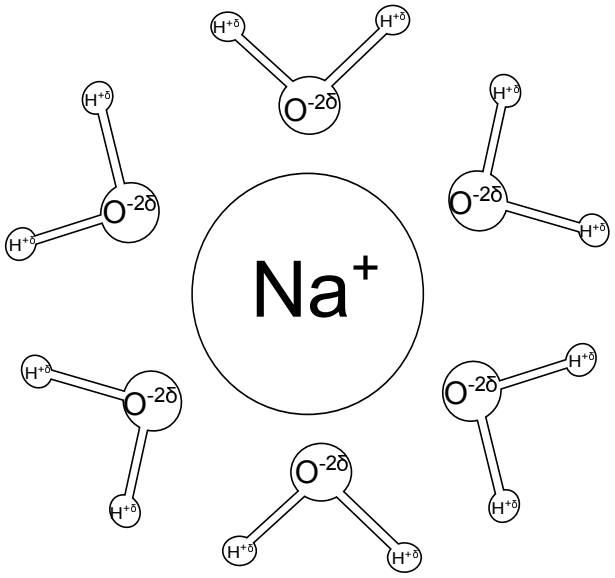

Figure 2.1.: Solvation of a Sodium ion (Na^+) by water ($H-O-H$) molecules.

2.2. Charge transport in bulk Electrolytes

The transport of individual dispersed charges in an electrolytic solution can be simplified by using a mean field approach, by expressing them as a volume averaged ion concentration. The transport equations for the charged species is called the Nernst-Planck equation [Zheng and Wei (2011)] and can be written as,

$$\frac{\partial c_i}{\partial t} = -\nabla \cdot \mathbf{J_i} + r_i \tag{2.2.1}$$

where, c_i is the molar concentration of the i^{th} ionic species, $\mathbf{J_i}$ is the ionic flux which can be written as a combination of three dominating fluxes, namely, the diffusive flux

($\mathbf{J_{D,i}}$), the electro-migration flux ($\mathbf{J_{E,i}}$), and the convective flux ($\mathbf{J_{C,i}}$). The term r_i accounts for the ion production due to chemical reactions of neutral species, which act as the source of ions. In this study, we will be focusing on unipolar injection of ions, which means that the ions are generated at the electrodes and there is no other chemical reaction going on in the bulk ($r_i = 0$). The diffusive flux is due to the concentration gradient present in the system and is expressed as, $\mathbf{J_{D,i}} = -D_i \nabla c_i$, where D_i is the coefficient of diffusion of the i^{th} ionic species. The electro-migration flux is due to the motion of the free charges dispersed in the solvent under the influence of an electric field. It can be expressed as, $\mathbf{J_{E,i}} = M_i F z_i c_i \mathbf{E}$, where M_i is the molar mobility of the i^{th} ionic species, F is the Faraday's constant which represents 1 mole of the electronic charge, z_i is the valence (charge number) of the i^{th} ionic species and $\mathbf{E}$ is the electric field vector. The values of ionic diffusivity (D_i) and mobility (M_i) for different ionic species is presented in Tab. 2.1. The convective flux is due to the flow field of the solvent and can be expressed as, $\mathbf{J_{C,i}} = \mathbf{u} c_i$. In a dilute solution, the background velocity ($\mathbf{u}$) is easy to define, which is the mass averaged velocity of the solvent. However, in concentrated solutions, such a velocity becomes more difficult to define, as the difference between the flux of an ion relative to the flow of the solvent is not clear. A generalized approach is to treat the motion of all the molecules (ions and solvent) in a coupled manner as in Stephan-Maxwell equations [Bird et al. (2007)]. But in this work, dilute electrolytes are considered, where such complexities can be neglected. Hence, the total ionic flux can be represented as,

$$\begin{aligned} \mathbf{J_i} &= \mathbf{J_{C,i}} + \mathbf{J_{D,i}} + \mathbf{J_{E,i}} \\ &= \mathbf{u} c_i - D_i \nabla c_i + M_i F z_i c_i \mathbf{E} \end{aligned} \tag{2.2.2}$$

ions at $T = 25°C$	H^+	K^+	Na^+	Br^-	Cl^-	F^-	I^-	OH^-
Molar Mobility, $M_i\,(10^{-8} m^2 mol/Js)$	36.2	7.62	5.19	8.09	7.91	5.70	7.96	20.6
Diffusivity, $D_i\,(10^{-9} m^2/s)$	9.31	1.96	1.33	2.08	2.03	1.46	2.05	5.30

Table 2.1.: Diffusivities and Mobilities of ions.

Using the Eq. 2.2.2 the Nernst-Plack equation (Eq. 2.2.1) can be rewritten as,

$$\frac{\partial c_i}{\partial t} = -\nabla \cdot (\mathbf{u} c_i - D_i \nabla c_i + M_i F z_i c_i \mathbf{E}) \tag{2.2.3}$$

The molar mobility of ions, M_i is related to the ionic diffusivity through the Einstein equation as, $M_i = D_i / RT$ where R is the universal gas constant and T is the ambient temperature. Assuming incompressible flow ($\nabla \cdot \mathbf{u} = 0$) for the ionic transport and representing the electric field as, $\mathbf{E} = -\nabla \phi$, where, ϕ is the electric potential, the

Nernst-Planck equation (see Eq. 2.2.3) can be written as,

$$\frac{\partial c_i}{\partial t} + (\mathbf{u} \cdot \nabla)\, c_i = D_i \nabla^2 c_i + \frac{D_i F z_i}{RT} \nabla \cdot (c_i \nabla \phi) \tag{2.2.4}$$

The Nernst-Planck equation contains two unknowns namely, the ionic concentration, c_i and the electrostatic potential field, ϕ. So in order to close the system of equations, one has to use the conservation of charges while considering the electroneutrality, $\rho_e = \sum_i F z_i c_i = 0$, where, ρ_e is the charge density of the system. The conservation of charge in the system can be obtained by having a divergence free flux of charges (or current density) as,

$$\nabla \cdot \mathbf{I} = 0 \tag{2.2.5}$$

where, $\mathbf{I}$ is the current density which is related to the ionic flux as,

$$\begin{aligned} \mathbf{I} &= \sum_i F z_i \mathbf{J_i} \\ &= \sum_i F z_i \mathbf{u} c_i - \sum_i F z_i D_i \nabla c_i - \sum_i \frac{F^2 z_i^2 D_i}{RT} c_i \nabla \phi \\ &= \mathbf{I_C} + \mathbf{I_D} + \mathbf{I_E} \end{aligned} \tag{2.2.6}$$

where, $\mathbf{I_C}$ is the convective current density, $\mathbf{I_D}$ is the diffusive current density and $\mathbf{I_E}$ is the electronic (Ohmic) current density. Using the above expression, the conservation of charge expression (see 2.2.5) for incompressible flows ($\nabla \cdot \mathbf{u} = 0$) leads to,

$$\begin{aligned} \nabla \cdot \mathbf{I} &= \sum_i F z_i \,(\mathbf{u} \cdot \nabla)\, c_i - \sum_i F z_i D_i \nabla^2 c_i - \sum_i \frac{D_i F^2 z_i^2}{RT} \nabla \cdot (c_i \nabla \phi) \\ &= (\mathbf{u} \cdot \nabla) \sum_i F z_i c_i - \sum_i F z_i D_i \nabla^2 c_i - \sum_i \frac{D_i F^2 z_i^2}{RT} \nabla \cdot (c_i \nabla \phi) = 0 \end{aligned} \tag{2.2.7}$$

From the electroneutrality condition ($\sum_i F z_i c_i = 0$), the conservation of charge expression reduces to,

$$\sum_i F z_i D_i \nabla^2 c_i + \sum_i \frac{D_i F^2 z_i^2}{RT} \nabla \cdot (c_i \nabla \phi) = 0 \tag{2.2.8}$$

For a binary ($i = 2$) and symmetric electrolyte ($z_+ = -z_- = z$), the electroneutrality condition gives,

$$\begin{aligned} F z_+ c_+ + F z_- c_- &= 0 \\ \Rightarrow c_+ &= c_- \end{aligned} \tag{2.2.9}$$

Taking $c_+ = c_- = c$, the conservation of charge reduces to,

$$F z \,(D_+ - D_-)\, \nabla^2 c + \frac{F^2 z^2}{RT} \,(D_+ + D_-)\, \nabla \cdot (c \nabla \phi) = 0 \tag{2.2.10}$$

2.3. Charge distribution near solid substrates

A solid surface (substrate) which is in contact with an electrolyte develops a surface charge density (which can be associated with a surface potential, ϕ_s). Some of the most plausible mechanisms causing such a phenomenon can be enlisted as, ionization or dissociation of surface groups and adsorption of ions from the solution [Israelachvili (2011)]. In order to maintain the electro-neutrality in the bulk region of the electrolyte, the surface charge of the solid substrate is balanced by a net opposite charge (through a combination of oppositely charged ions (counter-ions) and like charged ions (co-ions)) in the vicinity of the charged substrate. This ionic distribution physically manifests as a diffused cloud of ions screening the substrate potential and is structurally identified to have two distinct regions (see Fig. 2.2). The first region consists of counter-ions that are strongly attached to the charged substrate owing to strong Coulombic attractions. This region exists as a monolayer of immobile counter-ions and is commonly known as the Stern layer. Beyond the Stern layer, the ions are mobile and the plane separating the immobile and mobile layers of ions is also known as the slipping plane. The electric potential associated with this plane is called the zeta potential (ζ_b), which can be measured experimentally [Kirby and Hasselbrink (2004a)] and hence is commonly used in modeling electro-kinetics. The second region consists of ions suspended in a structural equilibrium under an attractive Coulombic force due to the charged wall, a repulsive Coulombic force due to the neighboring like charged ions, and the intrinsic thermal motion of the ions. This two-layered structure is also known as the electric double layer (EDL) and is modeled using the Gouy-Chapman-Stern (GCS) model [Lyklema (2001)]. The GCS model however has certain assumptions as,

1) Ions are modeled as point charges.

2) The dominant interaction between the charges in the diffuse double layer is the Coulombic interaction.

3) The solvent is assumed to be a structureless continuous media with constant dielectric permittivity throughout the double layer.

Although recent advances have been made in proposing more accurate models while considering the steric effects of the ions, ionic solvation etc, the GCS model has been quite effective in modeling the equilibrium distribution of charges near a charged surface. To obtain the equilibrium ionic charge distribution and the related potential field within the EDL one can assume a steady state with no background flow or external electric field. The net flux, $\mathbf{J_i}$ in such a case ($\mathbf{u} = \mathbf{0}$) can be written as,

$$\mathbf{J_i} = -M_i c_i \nabla \mu_i \tag{2.3.1}$$

where, μ_i is the molar chemical potential, which is defined as the change in the free energy of the system upon adding or removing one ion. The expression for the molar

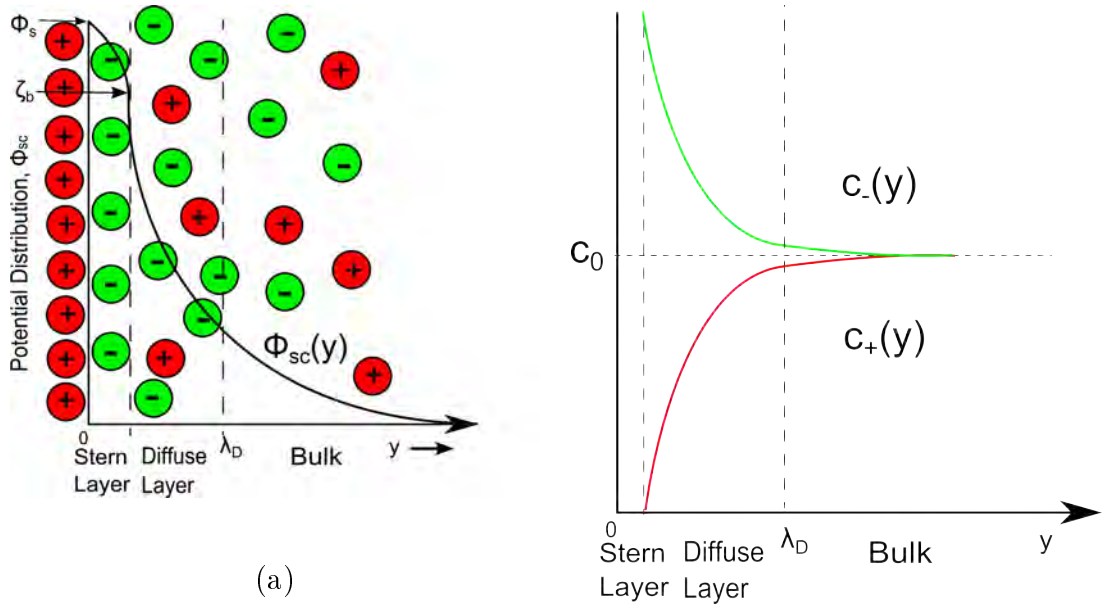

Figure 2.2.: Structure of an EDL near a positively charged surface with a surface potential (ϕ_s) showing (a) Electrostatic potential distribution (ϕ_{sc}), and (b) distribution of counter-ions ($c_-(y)$) and co-ions ($c_+(y)$).

chemical potential is,

$$\mu_i = \mu_{0,i} + RTln\left(\frac{c_i}{c_{0,i}}\right) + Fz_i\phi_{sc} \tag{2.3.2}$$

where, $\mu_{0,i}$ is the chemical potential of the initial state, $c_{0,i}$ is the initial (bulk) ionic concentration and ϕ_{sc} is the electrostatic potential field in the fluid due to the space-charge distribution. In electro-chemical equilibrium, the ions rearrange rapidly to counter any change in the concentration of the ions keeping the chemical potential constant. Therefore, the electro-chemical equilibrium requires the change in the chemical potential to be zero ($\triangle\mu_i = \mu_i - \mu_{0,i} = 0$) which gives,

$$RTln\left(\frac{c_i}{c_{0,i}}\right) + Fz_i\phi_{sc} = 0 \tag{2.3.3}$$

which results into a Boltzmann distribution of the charged species as,

$$c_i = c_{0,i}e^{-\frac{Fz_i\phi_{sc}}{RT}} \tag{2.3.4}$$

As from the first principle of differentiation, $\nabla\mu_i = \lim_{\triangle L\to 0} \triangle\mu_i/\triangle L$. So, from the Eq. 2.3.1, we can see that an electro-chemical equilibrium condition ($\triangle\mu_i = 0$) within

the EDL leads to a zero ionic flux condition too ($\mathbf{J_i} = 0$). To complete the set of equations and unknowns (namely c_i and ϕ_{sc}), we need a closure on the potential distribution, ϕ_{sc}. From Gauss's law,

$$\rho_e = \nabla \cdot \mathbf{D_{sc}} \tag{2.3.5}$$

where, ρ_e is the free charge density and $\mathbf{D_{sc}}$ is the electric displacement field due to the space charge distribution, which for a linear dielectric material can be written as a function of the electric field in the system,

$$\mathbf{D_{sc}} = \varepsilon_r \varepsilon_0 \mathbf{E_{sc}} \tag{2.3.6}$$

where ε_r is the dielectric constant of the medium, ε_0 is the permittivity of the vacuum and $\mathbf{E_{sc}}$ is the electric field distribution in the medium. From electrostatics,

$$\begin{aligned} \nabla \times \mathbf{E_{sc}} &= \mathbf{0} \\ \mathbf{E_{sc}} &= -\nabla \phi_{sc} \end{aligned} \tag{2.3.7}$$

Hence, the resulting equation can be written as,

$$\rho_e = -\nabla \cdot (\varepsilon_r \varepsilon_0 \nabla \phi_{sc}) \tag{2.3.8}$$

Upon combining the two equations we can obtain the equation for electric potential as a function of concentration distribution as,

$$-\nabla \cdot (\varepsilon_r \varepsilon_0 \nabla \phi_{sc}) = \sum_i F z_i c_i \tag{2.3.9}$$

Using the concentration expression from Eq. 2.3.4, for a symmetric binary electrolyte ($z_+ = -z_- = z$) and a solvent with constant permittivity, $\varepsilon_r \varepsilon_0$, Eq. 2.3.9 reduces to,

$$\begin{aligned} \varepsilon_r \varepsilon_0 \nabla^2 \phi_{sc} &= -\sum_i F z_i c_i \\ &= 2Fzc_0 sinh\left(\frac{Fz\phi_{sc}}{k_B T}\right) \end{aligned} \tag{2.3.10}$$

where, c_0 is the neutral bulk ionic concentration of the solution. The above equation is also known as the Poisson-Boltzmann Equation (PBE). Upon non-dimensionalizing the PBE using, $\Phi_{sc} = \phi_{sc}/\zeta_{ref}$, $\bar{\nabla} = h_0 \nabla$, where h_0 is the characteristic length scale of the system, Eq. 2.3.10 leads to,

$$\bar{\nabla}^2 \Phi_{sc} = \frac{sinh\left(\beta \Phi_{sc}\right)}{\beta De^2} \tag{2.3.11}$$

where, $\beta = \frac{ez\zeta_{ref}}{k_B T}$ is the ionic energy parameter which measures the relative strength of the electrostatic energy of ions with respect to the thermal energy of ions, $De =$

λ_D/h_0 is the Debye number with $\lambda_D = \sqrt{\frac{\varepsilon_r \varepsilon_0 k_B T}{2F^2 z^2 c_0}}$ as the Debye length, which represents the extent of the EDL. Hence, the Debye number represents the relative extent of the EDL as compared to the characteristic length scale of the system. For a symmetric $(1:1)$ electrolyte at $25°C$, the Debye length can be calculated as $\frac{0.305}{\sqrt{c_0}} nm$. Such a non-linear boundary value problem is not very easy to solve analytically and requires a numerical solution. However, analytical solutions exist for some simplified and practical cases.

One of the examples to demonstrate potential distribution in an EDL is by considering a charged solid substrate-electrolye system, with a surface zeta potential as ζ_b (which can be henceforth taken as the reference potential, $\zeta_{ref} = \zeta_b$), lying in the XZ plane at $Y = 0$ and the electrolyte in the $Y > 0$ half plane (see Fig. 2.2a). The potential distribution in the electrolyte can be obtained analytically by solving Eq. 2.3.11, while considering electro-neutrality in the bulk. With the assumption that at an infinite distance away from the charged surface, the ionic concentration reaches its bulk value ($c_i(Y \to \infty) \to c_{0,i}$) and the electrostatic potential becomes zero ($\Phi_{sc}(Y \to \infty) \to 0$) which complies with the electro-neutrality condition in the bulk, the electric potential distribution in the electrolyte can be written as [Israelachvili (2011)],

$$\Phi_{sc}(Y) = \frac{4}{\beta} tanh^{-1}\left[tanh\left(\frac{\beta}{4}\right) e^{\left(-\frac{Y}{De}\right)}\right] \tag{2.3.12}$$

Scaling the net charge density (ρ_e) by $\varepsilon_r \varepsilon_0 \zeta_b / h_0^2$ (see Eq. 2.3.8), the dimensionless net charge density ($\bar{\rho}_e$) can be written as,

$$\bar{\rho}_e = -\frac{sinh\left(4tanh^{-1}\left[tanh\left(\frac{\beta}{4}\right) e^{\left(-\frac{Y}{De}\right)}\right]\right)}{\beta De^2} \tag{2.3.13}$$

Commonly such electrolytic systems have low substrate zeta potential ($\zeta_b \leq 25mV$), which corresponds to $\beta < 1$ for a monovalent symmetric electrolyte at $25°C$. In that case, Eq. 2.3.11 can be linearized as (also known as the Debye-Hückel linearization [Debye and Huckel (1923)]),

$$\bar{\nabla}^2 \Phi_{sc} = \frac{\Phi_{sc}}{De^2} \tag{2.3.14}$$

which can be solved with the electro-neutrality condition in the bulk ($\Phi_{sc}(Y \to \infty) \to 0$) as,

$$\Phi_{sc}(Y) = e^{-\frac{Y}{De}} \tag{2.3.15}$$

and the corresponding dimensionless net charge density can be obtained as,

$$\bar{\rho}_e = -\frac{e^{-\frac{Y}{De}}}{De^2} \tag{2.3.16}$$

2.4. Electro-Hydrodynamics

2.4.1. Maxwell Stress in Electrolytes

Upon application of an external electric field on any media with a definite electrical permittivity, a Coulombic force is experienced by the free or bound charges present in the media, which react by creating an ionic flux and molecular scale polarization, respectively. Such a force is a function of the charge distribution within the media which can be represented in a volume averaged stress formalism (Maxwell stress) to facilitate the hydrodynamic coupling of the electrostatically imposed fluid flux. The Maxwell stress tensor ($\underline{\underline{\mathbf{\Sigma}^{\mathbf{M}}}}$) in a linear dielectric media in the absence of magnetic field can be written as [Melcher (1981)],

$$\underline{\underline{\mathbf{\Sigma}^{\mathbf{M}}}} = -\frac{\varepsilon_r \varepsilon_0}{2}\mathbf{E}\cdot\mathbf{E} + \varepsilon_r\varepsilon_0\mathbf{E}\otimes\mathbf{E} \tag{2.4.1}$$

where, $\mathbf{E}$ is the total electric field in the medium. The diffuse space charge potential near a charged surface in contact with an electrolyte leads to an electric field in the electrolyte as, $\mathbf{E_{sc}} = -\nabla\phi_{sc}$. The applied electric field creates a potential gradient too which can be written as, $\mathbf{E_{app}} = -\nabla\phi_{app}$. So, the net electric field, $\mathbf{E}$ (or potential, ϕ) in the system is a combination of the two effects as,$\mathbf{E} = \mathbf{E_{app}} + \mathbf{E_{sc}}$ (or $\phi = \phi_{app} + \phi_{sc}$).

2.4.2. Total Stress in Electrolytes

Fluids by definition are a phase of matter that flow (deform) indefinitely under the influence of a shearing action. Although, real fluids inherently show some resistance to such a flow by virtue of a property called viscosity, the nature of the rate of deformation of fluids for a given value of applied shear stress varies for different fluids and can be used for classification of fluids as such. If the rate of the deformation of a fluid varies linearly with the shear, it is categorized as a Newtonian fluid, if the variation is non-linear, it is categorized as a Non-Newtonian fluid. For common fluids like water, air and some oils, a linear relationship between the shear and the

deformation exists. From Hooke's law for isotropic fluids the viscous shear stress tensor ($\underline{\underline{\tau}}$) can be written as,

$$\underline{\underline{\tau}} = 2\mu\underline{\underline{\mathbf{D}}} + \lambda\left(\nabla\cdot\mathbf{u}\right)\underline{\underline{\mathbf{I}}} \tag{2.4.2}$$

where, λ is the Lamé's first parameter, μ is the Lamé's second parameter or shear modulus, and $\underline{\underline{\mathbf{I}}}$ is the identity tensor. The Lamé's parameters are related to the bulk modulus as, $K = \lambda + \frac{2}{3}\mu$. $\underline{\underline{\mathbf{D}}}$ is the strain rate tensor which is defined as,

$$\underline{\underline{\mathbf{D}}} = \frac{1}{2}\left(\nabla\mathbf{u} + \nabla\mathbf{u}^{\mathbf{T}}\right) \tag{2.4.3}$$

The total state of hydrodynamic stress in the fluid can be written as a combination of the hydrostatic component (pressure) and the deviatoric component (shear) as,

$$\underline{\underline{\mathbf{\Sigma}^{\mathbf{H}}}} = -p\underline{\underline{\mathbf{I}}} + \underline{\underline{\tau}} \tag{2.4.4}$$

where, p is the hydrostatic pressure. Hence, the net stress tensor ($\underline{\underline{\mathbf{\Sigma}^{\mathbf{T}}}}$) acting on a fluid under the influence of an external electric field is a combination of the Maxwell stress and the hydrodynamic stress tensor ($\underline{\underline{\mathbf{\Sigma}^{\mathbf{H}}}} = -p\underline{\underline{\mathbf{I}}} + \mu\left(\nabla\mathbf{u} + \nabla\mathbf{u}^{T}\right)$) and can be written as, $\underline{\underline{\mathbf{\Sigma}^{\mathbf{T}}}} = \underline{\underline{\mathbf{\Sigma}^{\mathbf{H}}}} + \underline{\underline{\mathbf{\Sigma}^{\mathbf{M}}}}$. Now with this net stress tensor, the momentum transport equation to describe the flow of a Newtonian fluid can be written as,

$$\begin{aligned}\rho\frac{D\mathbf{u}}{Dt} &= \nabla\cdot\underline{\underline{\mathbf{\Sigma}^{\mathbf{T}}}}\\ &= \nabla\cdot\underline{\underline{\mathbf{\Sigma}^{\mathbf{H}}}} + \nabla\cdot\underline{\underline{\mathbf{\Sigma}^{\mathbf{M}}}}\\ &= -\nabla p + \mu\nabla^2\mathbf{u} + \nabla\cdot\underline{\underline{\mathbf{\Sigma}^{\mathbf{M}}}}\end{aligned} \tag{2.4.5}$$

The divergence of the Maxwell stress tensor appears as a body force term in the momentum equations and can be expanded as [Melcher (1981)],

$$\nabla\cdot\underline{\underline{\mathbf{\Sigma}^{\mathbf{M}}}} = \nabla\cdot\left(-\frac{\varepsilon_r\varepsilon_0}{2}\mathbf{E}\cdot\mathbf{E} + \varepsilon_r\varepsilon_0\mathbf{E}\otimes\mathbf{E}\right) = -\frac{\varepsilon_0}{2}\mathbf{E}\cdot\mathbf{E}\nabla\varepsilon_r + \rho_e\mathbf{E} \tag{2.4.6}$$

For an isotropic dielectric material ($\nabla\varepsilon_r = 0$), the divergence of the Maxwell stress tensor reduces to the product of the charge distribution in the medium (ρ_e) and the net electric field. From Eq. 2.3.8, we can re-write the momentum equations as,

$$\begin{aligned}\rho\frac{D\mathbf{u}}{Dt} &= -\nabla p + \mu\nabla^2\mathbf{u} + \rho_e\mathbf{E}\\ &= -\nabla p + \mu\nabla^2\mathbf{u} + \varepsilon_r\varepsilon_0\nabla^2\phi_{sc}\nabla\phi\end{aligned} \tag{2.4.7}$$

Upon scaling the velocity as, $\mathbf{U} = \mathbf{u}/u_{ref}$, time as, $\theta = \omega t$, where, ω is the frequency of the periodic actuation, pressure, $P = p_{ref}h_0/\mu u_{ref}$, electrostatic potential, $\Phi = \phi/\zeta_{ref}$, gradient as, $\bar{\nabla} = h_0\nabla$, the momentum transport equation can be written as,

$$\begin{aligned}&\rho\omega u_{ref}\frac{d\mathbf{U}}{d\theta} + \frac{\rho u_{ref}^2}{h}\left(\mathbf{U}\cdot\bar{\nabla}\right)\mathbf{U} = -\frac{p}{h_0}\bar{\nabla}P + \frac{\mu u_{ref}}{h_0^2}\bar{\nabla}^2\mathbf{U} + \frac{\varepsilon_r\varepsilon_0\zeta_{ref}^2}{h_0^3}\bar{\nabla}^2\Phi_{sc}\bar{\nabla}\Phi\\ &\Rightarrow Wo^2\frac{d\mathbf{U}}{d\theta} + Re\left(\mathbf{U}\cdot\bar{\nabla}\right)\mathbf{U} = -\bar{\nabla}P + \bar{\nabla}^2\mathbf{U} + \gamma_R E_R\bar{\nabla}^2\Phi_{sc}\bar{\nabla}\Phi\end{aligned} \tag{2.4.8}$$

where, $Wo = \sqrt{\frac{\omega h_0^2}{\nu}}$ is the Womersley number, $Re = \frac{u_{ref} h_0}{\nu}$ is the Reynolds number, $\gamma_R = \frac{\varepsilon_r \varepsilon_0 \zeta_b E_0}{\mu u_{ref}}$ is the electro-viscous ratio, which quantifies the relative strength of electrical body forces to viscous forces, E_0 is the strength of the applied electric field ($|\mathbf{E_{app}}| = E_0$), and $E_R = \frac{\zeta_b}{E_0 h_0}$ is the ratio of the strengths of the electric field in the EDL to the applied electric field, which can be written as, $\Phi_{app} = -\int \mathbf{E_{app}} d\mathbf{r} = -\frac{1}{E_R} \int d\mathbf{R}$ (where $\mathbf{R}$and $\mathbf{r}$ are the dimensionless and dimensional position vectors, respectively). Also, at microscales the viscous effects dominate over inertial effects. So, upon assuming a steady system and neglecting the convective terms, the momentum transport equation can be written as,

$$-\bar{\nabla} P + \bar{\nabla}^2 \mathbf{U} + \gamma_R E_R \bar{\nabla}^2 \Phi_{sc} \bar{\nabla} \Phi = 0 \tag{2.4.9}$$

2.4.3. Electro-Osmotic Flow in a Parallel Plate System

In order to get an idea of the EOF velocity field in a parallel plate configuration of charged plates, let us consider two charged plates with a zeta potential as ζ_b and separated by a distance $2h_0$ in the xz plane. The first plate is at $y = -h_0$ and the second one is at $y = h_0$ (see Fig. 2.3). The dimensional scales used are, $Y = y/h_0$, $U = u/u_{ref}$, and $\Phi = \phi/\zeta_b$. The potential distribution in such a system can be obtained by using the PBE with the Debye-Hückel linearization for low zeta potential system (see Eq. 2.3.14). Upon using the boundary conditions as, $\Phi_{sc} = 1$ at the walls and the symmetry condition, $d\Phi_{sc}/dY = 0$ at the channel center ($Y = 0$), the space-charge potential distribution can be obtained as,

$$\Phi_{sc}(Y) = \frac{cosh\left(\frac{Y}{De}\right)}{cosh\left(\frac{1}{De}\right)} \tag{2.4.10}$$

And, the resulting net charge distribution is,

$$\bar{\rho}_e = -\frac{cosh\left(\frac{Y}{De}\right)}{De^2 cosh\left(\frac{1}{De}\right)} \tag{2.4.11}$$

Under the influence of an external electric field as, $\mathbf{E} = (E_{app}, 0, 0)$, no external pressure gradient ($\bar{\nabla} P = 0$), and a laminar and fully developed velocity field ($\mathbf{U} = (U(Y), 0, 0)$), the momentum transport equation (see Eq. 2.4.9) can be written as,

$$\frac{d^2 U}{dY^2} - \frac{\gamma_R cosh\left(\frac{Y}{De}\right)}{De^2 cosh\left(\frac{1}{De}\right)} = 0 \tag{2.4.12}$$

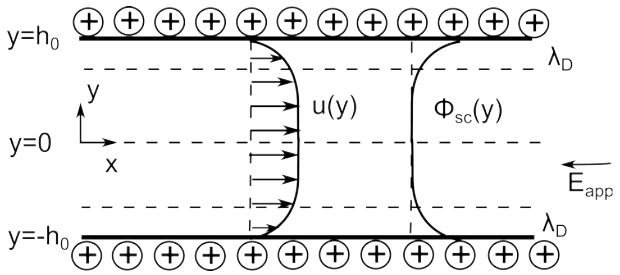

Figure 2.3.: Schematics of a parallel-plate EOF with the representation of velocity and potential distribution

Considering no-slip at the walls ($U(\pm 1) = 0$) and symmetry condition at the channel center ($\frac{dU}{dY}(0) = 0$), the EOF velocity field can be obtained as,

$$U(Y) = -\gamma_R \left[1 - \frac{cosh\left(\frac{Y}{De}\right)}{cosh\left(\frac{1}{De}\right)}\right] \tag{2.4.13}$$

In the limit of thin Debye layers as compared to the characteristic length scales ($De \ll 1$), the electro-osmotic velocity can be obtained as,

$$U(Y) = -\gamma_R \tag{2.4.14}$$

This dispersion-free plug type velocity profile is observed in many practical micro-systems where $h_0 \gg \lambda_D \sim O(0.1 - 10nm)$. In such a limit, the EOF velocity is taken as a slip velocity condition and is called the Helmholtz-Smoluchowski velocity as, $u_{HS} = -\varepsilon_r \varepsilon_0 \zeta_b E_{app}/\mu$.

2.5. Van der Waals Forces

Understanding the role of van der Waals forces in the micro-nanoscale systems is very important as they play a significant role in a wide range of important phenomena. Some of which are adhesion, surface tension, adsorption, wetting, multiphasic interactions of gases, liquids, and solids, and towards determining the structures of condensed macromolecules such as proteins and polymers. The van der Waals force between atoms and molecules is always present unlike the double-layer interaction. It is mostly insensitive to variations in electrolyte concentration and pH, and can be considered to be a constant characteristic force for a given set of interacting phases. Their main features may be summarized as follows [Israelachvili (2011)],

1. They are long-range forces and, depending on the situation, can be effective from large distances ($> 1nm$) down to inter-atomic spacings (about 1).

2. These forces may be repulsive or attractive.

3. Such forces not only bring molecules together but also tend to mutually align or orient them, though this orienting effect is usually weaker than with dipolar interactions.

4. They are not additive; that is the force between two bodies is affected by the presence of other bodies nearby. This is called the nonadditivity of an interaction.

Further, in the presence of electrical double layer interactions, the van der Waals attraction must always exceed the double-layer repulsion at small enough distances since it is a power law interaction. The free energies of interactions per unit area have mostly long-range apolar component only. However, short range repulsion forces are also present and act over distances $\leq 10nm$. The short range forces are electrostatic in nature occurring due to the overlap of diffuse electric double layers, which form near interfaces involving polar fluids [Craster and Matar (2009)]. The exact nature of such electric double layer based interactions has been detailed in the previous sections. The sequence of phenomena described above forms the basis of the celebrated DLVO theory of colloidal stability, after Derjaguin, Landau, Verwey and Overbeek [Russel et al. (1989)]. The free energy per unit volume for the long range interactions can be written as [Sharma and Jameel (1993)],

$$\phi_{vdW} = \frac{a}{6\pi h^3} \tag{2.5.1}$$

where, a is the Hamaker constant, and h is the distance between the interacting surfaces. The disjoining pressure is defined as, $p_d = -\phi_{vdW}$.

2.6. Interfacial Boundary Conditions

2.6.1. Continuity of Stress

The fluid-fluid interfaces are stress free interfaces as they instantly flow under the application of a shearing force. In other words, the net surface traction, which is defined as the surface force per unit area applied by one fluid should be completely balanced by the net surface traction by the second fluid across the interface. The surface traction ($\mathbf{T}$) is related to the total state of stress ($\underline{\underline{\mathbf{\Sigma^T}}} = \underline{\underline{\mathbf{\Sigma^H}}} + \underline{\underline{\mathbf{\Sigma^M}}}$) at a point by Cauchy's stress theorem as, $\mathbf{T} = \underline{\underline{\mathbf{\Sigma^T}}} \cdot \mathbf{n}$, where, $\mathbf{n}$ is the normal vector to the surface. However, when there is interfacial deformation and variation of the interfacial tension, a finite difference (jump) in the surface traction across the fluid-fluid interfaces is observed which balances out interfacial forces due to any such deformation or variation. The continuity of stress in such cases require,

$$\left[\underline{\underline{\mathbf{\Sigma^T}}} \cdot \mathbf{n}\right] = \gamma \mathbf{n} \left(\nabla \cdot \mathbf{n}\right) - \nabla_{\mathbf{s}} \gamma \tag{2.6.1}$$

where, $\left[\underline{\underline{\mathbf{\Sigma^T}}} \cdot \mathbf{n}\right] = \underline{\underline{\mathbf{\Sigma_1^T}}} \cdot \mathbf{n} - \underline{\underline{\mathbf{\Sigma_2^T}}} \cdot \mathbf{n}$, is the difference in the total stress at the interface between the bounding phases 1 and 2, and $\nabla_s = \nabla - \mathbf{n}\left(\mathbf{n} \cdot \nabla\right)$ is the surface gradient

operator and models the variations in interfacial tension such as due to temperature (thermocapillarity), species concentration (solutocapillarity), and electric field (electrocapillarity). By definition, the surface gradient operator is the gradient operator minus the normal component of the gradient operator. Hence, it is always tangential to the interface and is zero for the systems with constant temperature, surfactant concentration, and the electric field. The Eq. 2.6.1 can be hence separated into normal and tangential components of the stress. The jump in the normal component of the stress can be attributed to the curvature induced due to the interfacial deformation and can be represented by,

$$\left[\mathbf{n}\cdot\underline{\underline{\boldsymbol{\Sigma}^{\mathbf{T}}}}\cdot\mathbf{n}\right]=\gamma\nabla\cdot\mathbf{n} \tag{2.6.2}$$

Similarly, the jump in the tangential component of the stress can be written as,

$$\left[\mathbf{t}\cdot\underline{\underline{\boldsymbol{\Sigma}^{\mathbf{T}}}}\cdot\mathbf{n}\right]=-\mathbf{t}\cdot\nabla_{\mathbf{s}}\gamma \tag{2.6.3}$$

2.6.2. Kinematic Condition

In the absence of a net mass flux through the fluid-fluid interface, i.e. an impermeable interface, the relative velocity component of the fluid normal to the interface must be zero. This means that if the interface is stationary, the normal component of the velocity is zero. This idea can be represented by,

$$(\mathbf{U}-\mathbf{V})\cdot\mathbf{n}=0 \tag{2.6.4}$$

where, $\mathbf{U}$ is the fluid velocity at the interface and $\mathbf{V}$ is the interfacial velocity. If the interface is to be represented by, $f(\mathbf{r},t)=0$, the unit normal vector pointing in the region $f(\mathbf{r},t)>0$ is given by, $\mathbf{n}=\frac{\nabla f}{|\nabla f|}$. Now, within the reference frame of the interface the material derivative of the interface vanishes ($\frac{Df}{Dt}=0$), which gives the interfacial velocity as, $\mathbf{V}\cdot\nabla f=-\frac{\partial f}{\partial t}$ or in a simplified manner, $\mathbf{V}\cdot\mathbf{n}\,|\nabla f|=-\frac{\partial f}{\partial t}$. Hence Eq. 2.6.4 can be rewritten as,

$$\mathbf{U}\cdot\frac{\nabla f}{|\nabla f|}=-\frac{1}{|\nabla f|}\frac{\partial f}{\partial t} \tag{2.6.5}$$

which reduces to,

$$\mathbf{U}\cdot\nabla f=-\frac{\partial f}{\partial t} \tag{2.6.6}$$

2.6.3. Gauss's law

The Gauss's law relates the electric field distribution to the electrical charge distribution. It says that the net electrical flux through a closed surface is proportional to the total charge enclosed by the surface. While considering the free charge distribution (i.e. ignoring the polarized charges in a dielectric), one can express it as,

$$\oint_C \mathbf{D} \cdot \mathbf{dS} = \iiint_V \rho_f dV \tag{2.6.7}$$

where, $\mathbf{D}$ is the electric displacement field and ρ_f is the free charge density. From the control volume V (see Fig. 2.4) one can write the above equation as,

$$\int \mathbf{D_1}\cdot\mathbf{n_1}dx + \int (\mathbf{D_1}+\mathbf{D_2})\cdot\mathbf{n_2}dy + \int \mathbf{D_2}\cdot\mathbf{n_3}dx + \int (\mathbf{D_1}+\mathbf{D_2})\cdot\mathbf{n_4}dy = \rho_f \triangle x \tag{2.6.8}$$

Using, $\mathbf{D_1} = D_{1,t}\mathbf{i} + D_{1,n}\mathbf{j}$, $\mathbf{D_2} = D_{2,t}\mathbf{i} + D_{2,n}\mathbf{j}$, $\mathbf{n_1} = -\mathbf{j}$, $\mathbf{n_2} = -\mathbf{i}$, $\mathbf{n_3} = \mathbf{j}$, and $\mathbf{n_4} = \mathbf{i}$, Eq. 2.6.8 can be finally expressed as,

$$D_{2,n} - D_{1,n} = \rho_f \tag{2.6.9}$$

where, n is the direction normal to the interface. From the Eq. 2.3.6 and using, $E_n = -\frac{\partial \phi}{\partial n}$, the jump of electrical potential gradient across the interface can be written as,

$$\left[\varepsilon_r \varepsilon_0 \frac{\partial \phi}{\partial n}\right]_1^2 = \rho_f \tag{2.6.10}$$

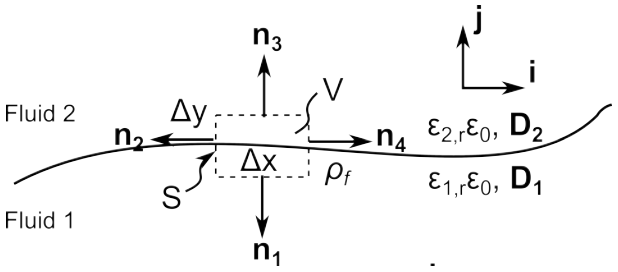

Figure 2.4.: Schematics of a control volume (V) and control surface (S) at a charged interface with a surface charge density (ρ_f).

2.6.4. Faraday's law of induction

Faraday's law of induction suggests how a time-varying magnetic field ($\mathbf{B}$) creates a spatially varying, non-conservative electric field. In differential form, it can be

written as,

$$\nabla \times \mathbf{E} = -\frac{\partial \mathbf{B}}{\partial t} \tag{2.6.11}$$

In integral form, it can be written as,

$$\oint \mathbf{E} \cdot \mathbf{dl} = -\iint \frac{\partial \mathbf{B}}{\partial t} \cdot \mathbf{dS} \tag{2.6.12}$$

In the absence of the magnetic field, it shows the conservative nature of the electric field, that the total work done by an electric field in a closed loop is zero (see Fig. 2.5).

$$\int \mathbf{E_1} \cdot \mathbf{t_1} dx + \int (\mathbf{E_1} + \mathbf{E_2}) \cdot \mathbf{t_2} dy + \int \mathbf{E_2} \cdot \mathbf{t_3} dx + \int (\mathbf{E_1} + \mathbf{E_2}) \cdot \mathbf{t_4} dx = 0 \tag{2.6.13}$$

Using, $\mathbf{E_1} = E_{1,t}\mathbf{i} + E_{1,n}\mathbf{j}$, $\mathbf{E_2} = E_{2,t}\mathbf{i} + E_{2,n}\mathbf{j}$, $\mathbf{t_1} = -\mathbf{i}$, $\mathbf{t_2} = \mathbf{j}$, $\mathbf{t_3} = \mathbf{i}$, and $\mathbf{t_4} = -\mathbf{j}$ in the Eq. 2.6.13, the jump in the tangential component of electric field across the interface is obtained as,

$$E_{2,t} - E_{1,t} = 0 \tag{2.6.14}$$

which, in terms of jump of electric potential can be written as,

$$\left[\frac{\partial \phi}{\partial x}\right]_1^2 = 0 \tag{2.6.15}$$

which, upon integrating leads to,

$$[\phi]_1^2 = \zeta_I \tag{2.6.16}$$

where, ζ_I is the interfacial zeta potential.

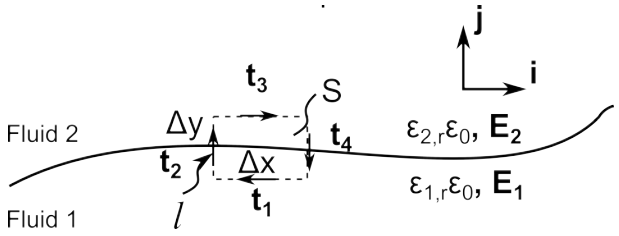

Figure 2.5.: Schematics of a control surface (S) and the enclosing loop (l) at a fluid-fluid interface.

2.6.5. Conservation of charge

The conservation equation of charged species across an interface can be obtained by integrating the charge transport equation (see Eq. 2.2.3) across the interface while assuming that there are no chemical reactions taking place.

$$\frac{\partial c_i}{\partial t} = -\nabla \cdot (\mathbf{u}c_i - D_i \nabla c_i + M_i F z_i c_i \mathbf{E}) \tag{2.6.17}$$

where, for i^{th}ionic species, c_i is the molar concentration, $\mathbf{u}$ is the convective velocity field, D_i is the ionic diffusivity, M_i is the ionic mobility, F is the Faraday's constant, z_i is the ionic valence and $\mathbf{E}$ is the applied electric field. Upon integrating the above equation across the interface, one can obtain,

$$\begin{aligned}
\frac{\partial c_{i,s}}{\partial t} &= -\nabla \cdot \int (\mathbf{u}c_i)\, \mathbf{dS} + \int \nabla \cdot (D_i \nabla c_i)\, \mathbf{dS} - \int \nabla \cdot (M_i F z_i c_i \mathbf{E})\, \mathbf{dS} \\
&= -\mathbf{u} \cdot \nabla c_{i,s} + \int (D_i \nabla c_i) \cdot \mathbf{n} dl - \int (M_i F z_i c_i \mathbf{E}) \cdot \mathbf{n} dl \\
&= -\mathbf{u} \cdot (\nabla_s + \mathbf{n} \cdot (\mathbf{n} \cdot \nabla))\, c_{i,s} + [D_i \nabla c_{i,s} - M_i F z_i c_{i,s} \mathbf{E}]_1^2 \cdot \mathbf{n}
\end{aligned} \tag{2.6.18}$$

where, $c_{i,s}$ is the surface concentration of the i^{th} species and ∇_s is the surface gradient. In order to obtain the conservation equation of the net surface charge density, $q_{f,s} = \sum_i F z_i c_{i,s}$ one can multiply the Eq.2.6.18 by $F z_i$ and perform a summation over all of the ionic species as,

$$\begin{aligned}
\frac{\partial q_{f,s}}{\partial t} &= -\mathbf{u} \cdot \nabla_s q_{f,s} - \mathbf{n} \cdot \mathbf{u}\, (\nabla \cdot \mathbf{n})\, q_{f,s} + \left[\sum_i D_i F z_i \nabla c_{i,s} - \mathbf{E} \sum_i F^2 z_i^2 M_i c_{i,s} \right]_1^2 \cdot \mathbf{n} \\
&= \underbrace{-\mathbf{u} \cdot \nabla_s q_{f,s} - u_n\, (\nabla \cdot \mathbf{n})\, q_{f,s}}_{\textit{Interfacial Deformation}} + \left[\underbrace{\sum_i D_i F z_i \nabla c_{i,s}}_{\textit{Diffusive Current}} - \underbrace{\Lambda_{m,s} \mathbf{E}}_{\textit{Ohmic Current}} \right]_1^2 \cdot \mathbf{n}
\end{aligned} \tag{2.6.19}$$

where, $\Lambda_{m,s}$ is the molar surface conductivity. Hence, from the above expression, one can see that the contributions to the net change in the surface charge density is by the deformation (extension/shrinkage) of the interface, the diffusive surface current

and the Ohmic surface current. In the case of a binary ($i = 2$) and symmetric ($z_+ = z_- = z$) electrolyte with same diffusivity ($D_+ = D_- = D$), one can re-write the Eq. 2.6.19 as,

$$\frac{\partial q_{f,s}}{\partial t} = -\mathbf{u} \cdot \nabla_s q_{f,s} - \mathbf{n} \cdot \mathbf{u} \left(\nabla \cdot \mathbf{n}\right) q_{f,s} + \left[D \nabla q_{f,s} - \Lambda_{m,s} \mathbf{E}\right]_1^2 \cdot \mathbf{n} \tag{2.6.20}$$

Part II.

Theoretical Studies

3. Thin Films in Electrokinetics

3.1. Overview

This chapter explores the dynamics of a viscous electrolytic thin film bounded by a solid surface from below and a low viscosity and low permittivity gas phase from the top. The EOF dynamics of such a film is studied under steady and time-periodic potential bias, V_{app} (or electric field, $E_{app} = V_{app}/L$), where the electrodes are kept L distance apart. The gas-liquid interface is considered to have a constant interfacial potential, ζ_I, and the substrate-liquid potential is taken to be ζ_b. The height of the thin film is taken to be h_0. Firstly, the flow characteristics of the conductive thin film under a steady (DC) electric field is explored, where a detailed parametric dependence of the velocity profile is presented.

Further, a contrasting analysis of time periodic (AC) EOF in a thin liquid layer with a flat free surface and that of a thin layer of liquid between two rigid boundaries has been carried out. In order to establish a common comparative basis between the two cases, an unperturbed interface for the former case is considered here, which technically represents the basic state of a general thin film stability problem. In an effort to bring out the interesting interplay between the characteristic length scale of the liquid layer and the characteristic electric double layer (EDL) length scale (Debye length), various orders of the liquid layer thickness to Debye length ratios are addressed. For further generalizations, the possibilities of addressing the effect of high zeta potentials on thin film dynamics by invoking the non-linear Poisson-Boltzmann equation are considered. The analytical expressions for the electric potential and velocity field are derived, bringing out important implications of Maxwell stresses at the free surface.

Finally, the thin film dynamics under DC EOF is explored in a rectangular geometry with various aspect ratios, where the effect of EDL parameters on the fluid flow rate is presented. Such a study is important for realistic cases where a gaseous film lies between the fluid and the bounding walls, thus creating a free-surface situation. The presence of such gaseous layers is commonly observed near hydrophobic substrates, or sometimes due to the generation of gaseous products as a part of certain electrochemical reactions. Also, it provides a base state flow condition for further studies on instabilities associated with a two-layer EOF in the presence of steady or time periodic electric fields.

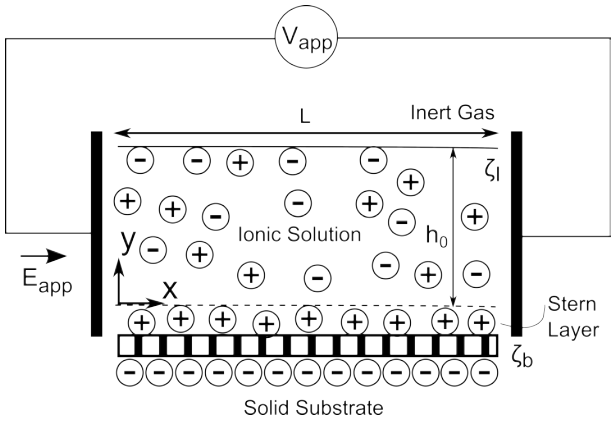

Figure 3.1.: Schematics of a 2D thin film system under EOF

3.2. Thin Films in DC Electro-osmosis

3.2.1. Mathematical Model

Electric potential field

In this study, the thin film system is considered to have large lateral extents which results into negligible x-gradients as compared to the y-gradients (hence, $\nabla \sim d/dy$). The space charge distribution within the conductive film leads to a potential field, ϕ_{sc}, where, the solid substrate ($y = 0$) and the gas-liquid interface ($y = h_0$) are considered to be at constant potential with the associated boundary conditions as,

$$\begin{aligned} \phi_{sc}(0) &= \zeta_b \\ \phi_{sc}(h_0) &= \zeta_I \end{aligned} \tag{3.2.1}$$

The potential distribution can be obtained as a solution of the Poisson-Boltzmann equation (PBE) (see Eq. 2.3.10). Upon using the reference scales as, $\Phi_{sc} = \phi_{sc}/\zeta_b$ and $Y = y/h_0$, the dimensionless PBE (see Eq. 2.3.11) can be written as,

$$\frac{d^2\Phi_{sc}}{dY^2} = \frac{sinh(\beta\Phi_{sc})}{\beta De^2} \tag{3.2.2}$$

where, $De = \lambda_D/h_0$ is the ratio of the Debye length (λ_D) and the film thickness (h_0), and $\beta = \frac{ez\zeta_b}{k_B T}$ is the ionic energy parameter (see Chapter 2). The boundary conditions in the dimensionless form can be written as,

$$\begin{aligned} \Phi_{sc}(0) &= 1 \\ \Phi_{sc}(0) &= Z_R \end{aligned} \tag{3.2.3}$$

where, $Z_R = \zeta_I/\zeta_b$ is the ratio of the interfacial zeta potential to the substrate zeta potential. The value of the interfacial potential depends upon electrochemistry of the problem and hence, Z_R is taken as a variable parameter. Generally, the substrate zeta potential is less than the thermal potential, i.e. $\beta < 1$. In that limit, the Eq. 3.2.2 can be linearized (see Eq. 2.3.14) and the boundary value problem (Eq. 3.2.2-3.2.3) can be solved analytically to obtain the following closed form solution,

$$\Phi_{sc}(Y) = \frac{1}{sinh\left(\frac{1}{De}\right)}\left\{Z_R sinh\left(\frac{Y}{De}\right) + sinh\left(\frac{1-Y}{De}\right)\right\} \tag{3.2.4}$$

However, for larger wall zeta-potential systems ($\beta \geq 1$), Eqs. 3.2.2 and 3.2.3 have to be solved in their non-linear form. This system of equations is a boundary value problem (BVP) having two Dirichlet boundary conditions along with a non-linear second order ordinary differential equation, for which no tractable analytical solution is available. Hence, to obtain the resulting potential distribution one has to resort to numerical tools. It is also observed that for thin EDLs ($De \leq 0.1$), $1/\beta De^2$ is much larger than 1, making the differential equation very stiff with large variations over short distances (for example, within the EDL). A stiff differential equation is a class of differential equations where one is forced to use small step size while integrating even when the solution is expected to show smooth characteristics (very little variation) in a region [Lambert (1992)]. To solve such a highly stiff BVP, the Automated Continuation with Deferred Correction (ACDC) method by Cash et al. (2001) is used here. This method is based on implicit Runge-Kutta scheme on a Lobatto grid. A Lobatto grid includes boundary points in the integration interval, facilitating the use of an adaptive mesh. Such an adaptive mesh is extremely useful for systems having large spatial gradients like a boundary layer or an EDL. The electric potential due to the externally applied electric field (Φ_{app}) can be written in the dimensionless form as,

$$\Phi_{app}(X) = -\int \frac{E_0 h_0}{\zeta_b} dX = -\frac{X}{E_R} \tag{3.2.5}$$

where, $\Phi_{app} = \phi_{app}/\zeta_b$, $X = x/h_0$, and $E_R = \zeta_b/E_0 h_0$. The net electric potential in the system can be written as a sum of the potential fields due to the space charge distribution (Φ_{sc}) and the externally applied electric field (Φ_{app}). The dimensionless total electric potential of the system can be written as,

$$\begin{aligned}\Phi(X,Y) &= \Phi_{app}(X) + \Phi_{sc}(Y) \\ &= -\frac{X}{E_R} + \frac{1}{sinh\left(\frac{1}{De}\right)}\left\{Z_R sinh\left(\frac{Y}{De}\right) + sinh\left(\frac{1-Y}{De}\right)\right\}\end{aligned} \tag{3.2.6}$$

Velocity Field

The hydrodynamics of the flat thin electrolytic film is explored under the influence of an externally applied electric field by considering a steady and a laminar velocity

field ($\mathbf{U} = (U(Y), 0, 0)$) with no externally applied pressure gradient ($dP/dX = 0$) and a flat interface ($Y = 1$). The base state x-momentum transport equations (see Eq. 2.4.9) in dimensionless form can be written as,

$$\frac{d^2U_b}{dY^2} - \gamma_R \frac{\partial^2 \Phi_{sc}}{\partial Y^2} = 0 \tag{3.2.7}$$

and, the base state y-momentum transport equation (see Eq. 2.4.9) can be written as,

$$-\frac{dP_b}{dY} + \gamma_R E_R \frac{\partial \Phi_{sc}}{\partial Y} \frac{\partial^2 \Phi_{sc}}{\partial Y^2} = 0 \tag{3.2.8}$$

At the solid substrate ($Y = 0$), a no slip boundary condition gives,

$$U_b(0) = 0 \tag{3.2.9}$$

At the gas-liquid interface ($Y = 1$), the continuity of shear and normal stresses respectively give,

$$\frac{dU_b}{dY} + \gamma_R E_R \frac{\partial \Phi}{\partial X} \frac{\partial \Phi}{\partial Y} = 0 \tag{3.2.10}$$

$$P_b - \frac{\gamma_R E_R}{2} \left\{ \left(\frac{\partial \Phi}{\partial X} \right)^2 - \left(\frac{\partial \Phi}{\partial Y} \right)^2 \right\} = 0 \tag{3.2.11}$$

From Eqs. 3.2.7-3.2.11, the solutions for $U_b(Y)$ and $P_b(Y)$ can be obtained as follows,

$$U_b(Y) = -\gamma_R \left(1 - \frac{Z_R sinh\left(\frac{Y}{De}\right) + sinh\left(\frac{1-Y}{De}\right)}{sinh\left(\frac{1}{De}\right)} \right) \tag{3.2.12}$$

$$P_b(Y) = \frac{\gamma_R E_R}{2De^2 sinh^2\left(\frac{1}{De}\right)} \left\{ Z_R cosh\left(\frac{Y}{De}\right) - cosh\left(\frac{1-Y}{De}\right) \right\}^2 \tag{3.2.13}$$

The fluid velocity at the free surface is then,

$$U_b(1) = \gamma_R (Z_R - 1) \tag{3.2.14}$$

which has a linear dependence upon the zeta-potential at the interface. This dependence, which is by virtue of the polarity of the interfacial potential, is observed to facilitate or delay the free surface stability by either increasing or decreasing the shear stress [Choi et al. (2010)].

3.3. Thin Films in AC Electro-osmosis

3.3.1. Mathematical Model

Electric potential field

The dimensionless electric potential due to the externally oscillating applied electric field ($\mathbf{E}_{app} = E_0 sin(\omega t)$) can be written in the dimensionless form as,

$$\Phi_{app}(X,\Theta) = -\int_0^X \frac{E_0 h_0}{\zeta_b} sin\Theta dX = -\frac{X}{E_R} sin\Theta \tag{3.3.1}$$

where, $\Theta = \omega t$. The net electric potential in the system can be written as a sum of the potential field due to the space charge distribution (Φ_{sc}) (see Eq. 3.2.4) and the externally applied electric field (Φ_{app}). The dimensionless total electric potential of the system under a time-periodic electric field can be written as,

$$\Phi(X,Y,\Theta) = \Phi_{app}(X,\Theta) + \Phi_{sc}(Y) \tag{3.3.2}$$

Velocity field

Upon non-dimensionalizing the flow variables as, $U = u/u_{ref}$ and without an external pressure gradient the dimensionless momentum conservation Eq. 2.4.8 reduces to,

$$\begin{aligned} Wo^2 \frac{\partial U}{\partial \Theta} &= \frac{\partial^2 U}{\partial Y^2} + \gamma_R E_R \frac{\partial \Phi}{\partial X}\frac{\partial^2 \Phi}{\partial Y^2} \\ &= \frac{\partial^2 U}{\partial Y^2} - \gamma_R sin\Theta \frac{d^2\Phi_{sc}}{dY^2} \end{aligned} \tag{3.3.3}$$

where, $Wo = \sqrt{\omega h_0^2/\nu}$ is the Womersley number expressing the relative strength of temporal inertial force over the viscous dissipation force. The dimensionless y-momentum equation gives,

$$\begin{aligned} 0 &= -\frac{dP}{dY} + \gamma_R E_R \frac{\partial \Phi}{\partial Y}\frac{\partial^2 \Phi}{\partial Y^2} \\ &= -\frac{dP}{dY} + \gamma_R E_R \frac{d\Phi_{sc}}{dY}\frac{d^2\Phi_{sc}}{dY^2} \end{aligned} \tag{3.3.4}$$

The interfacial boundary conditions in dimensionless form (see Eqs. 3.2.10 and 3.2.11) are,

$$\frac{\partial U}{\partial Y} = \gamma_R sin\Theta \frac{d\Phi_{sc}}{dY} \tag{3.3.5}$$

$$P(1,\Theta) = \gamma_R E_R \left(\left(\frac{\partial \Phi}{\partial X}\right)^2 - \left(\frac{\partial \Phi}{\partial Y}\right)^2 \right) \tag{3.3.6}$$

with no-slip condition at the wall ($Y = 0$),

$$U(0, \Theta) = 0 \tag{3.3.7}$$

The solution of the system of equations 3.3.3-3.3.7 can be obtained by decomposing the velocity into time-dependent and space-dependent functions as,

$$U(Y, \Theta) = F(Y)G(\Theta) = Im\left(F(Y)\, e^{i\Theta}\right) \tag{3.3.8}$$

Upon substituting Eq. 3.3.8 in Eq. 3.3.3, an ordinary differential equation in $F(Y)$ is obtained as,

$$i\, Wo^2 F = \frac{d^2F}{dY^2} - \gamma_R \frac{d^2\Phi_{sc}}{dY^2} \tag{3.3.9}$$

the corresponding boundary conditions are,

$$F(0) = 0 \tag{3.3.10}$$

$$\frac{dF}{dY} - \gamma_R \frac{d\Phi_{sc}}{dY} = 0 \tag{3.3.11}$$

For a generalized potential distribution, the resulting velocity profile can be obtained as,

$$U(Y, \Theta) = \gamma_R Im \begin{bmatrix} \Phi_{sc}(Y)\, e^{i\Theta} - \frac{cosh\left(\sqrt{i}(1-Y)\, Wo\right)}{cosh\left(\sqrt{i}\, Wo\right)} \Phi_{sc}(0)\, e^{i\Theta} \\ -\frac{cosh\left(\sqrt{i}(1-Y)\, Wo\right)}{cosh\left(\sqrt{i}\, Wo\right)} e^{i\Theta} \sqrt{i}\, Wo \int_0^1 cosh\left(\sqrt{i}\, Wo\,(1-\eta)\right) \Phi_{sc}(\eta)\, d\eta \\ \frac{\sqrt{i}\, Wo}{2} e^{i\Theta + \sqrt{i}\, WoY} \int_0^Y e^{-\sqrt{i}\, Wo\eta} \Phi_{sc}(\eta)\, d\eta \\ -\frac{\sqrt{i}\, Wo}{2} e^{i\Theta - \sqrt{i}\, WoY} \int_0^Y e^{\sqrt{i}\, Wo\eta} \Phi_{sc}(\eta)\, d\eta \end{bmatrix} \tag{3.3.12}$$

To obtain the velocity field for a generalized potential, one needs to perform the involved integrations in Eq. 3.3.12 numerically. In this study, the QUADPACK numerical integration package [Favati et al. (1991)] was used which effectively handles the integration of complex functions with the help of an adaptive automatic integration algorithm using Gauss-Kronrod rule. For general cases where the substrate zeta potential lies within the Debye-Hückel limit, upon using a space-charge potential obtained by Debye-Hückel linearization, the velocity expression can be simplified analytically and written as,

$$U(Y, \Theta) = U_a(Y)\, sin\left(\Theta + \Delta(Y)\right) \tag{3.3.13}$$

where, $U_a(Y)$ is the amplitude and $\Delta(Y)$ is the phase of the velocity. Detailed expressions of the amplitude and the phase are given in the Appendix $A1$. Similarly

with the Debye-Hückel linearization, the pressure distribution in the system can be obtained by solving Eqs. 3.3.4 and 3.3.6 as,

$$P(Y,\Theta) = \frac{\gamma_R}{4E_R} cos\,(2\Theta) - \frac{\gamma_R}{4E_R} + \frac{\gamma_R E_R}{2De^2 sinh^2\left(\frac{1}{De}\right)} \left\{ Z_R cosh\left(\frac{Y}{De}\right) - cosh\left(\frac{1-Y}{De}\right) \right\}^2 \tag{3.3.14}$$

It is also observed from Eqs. 3.3.3 and 3.3.4 that in the absence of an external pressure gradient, the velocity and pressure distributions are decoupled and are parametrically dependent on the applied electric field and space-charge potential distribution.

3.3.2. Results and Discussion

It can be seen from Eq. 3.3.6 that the interfacial boundary condition is no longer a classical hydrodynamic stress free boundary condition. The Maxwell stress, by the virtue of the Coulombic force on the space charge distribution and the free surface potential, contributes to the interfacial dynamics as well. To demonstrate the effects of Maxwell stress on electro-osmotic flows, a comparison of flow characteristics between EOF under a Hele-Shaw configuration (parallel plate flow) [Chakraborty and Srivastava (2007); Dutta and Beskok (2001)] and the free surface EOF has been carried out. Although being two completely different physical systems the mentioned problems share a similar physical modeling in terms of governing equation and boundary conditions. The most general modeling of a parallel plate EOF system involves Stokes equations with a Helmholtz-Smoluchowski slip velocity at the walls and a symmetry condition applied on the velocity at the channel centerline. Such a system has been very successful in modeling microscale EOF owing to the thin EDL length scales as compared to the channel length scales. However, for systems where the EDL thickness becomes comparable to the channel length scales, one can add an electrical body force term in the Stokes equations, the involved electric charge distribution being obtained from the electrical potential distribution which results as a solution of the PBE [Chakraborty and Srivastava (2007); Dutta and Beskok (2001)]. In the second case, the wall boundary condition is a no slip condition along with the previously used symmetry condition at the channel centerline. Similarly, the modeling of a thin free surface flow involves a Stokes equation with no slip condition at the wall and a stress free condition at the free surface. In the absence of various surface phenomena such as surface tension variation, phase change and mass transfer, the stress free condition at the free surface ($\partial u/\partial y = 0$) is mathematically the same as a symmetry condition at the channel center ($\partial u/\partial y = 0$) in a parallel plate EOF [Chakraborty and Srivastava (2007); Dutta and Beskok (2001)]. Hence, the commonly studied parallel plate EOF can be put forth as a case without the Maxwell stress, which in the simplified form adds a term involving transverse gradient of electric potential at the free surface (see Eq. 3.3.6). As a consequence, it is

seen that, in the presence of very thin EDLs ($De = 0.01$) and no interfacial potential ($Z_R = 0$), the free surface system behaves as a classical half channel EOF system where the electrical effects are localized close to the wall and the far field electric potential is zero. A validation of the present free surface model developed in the previous sections is presented through a comparison with a Hele-Shaw EOF, where the half channel velocity profile was taken from the seminal work of Dutta and Beskok (2001) (see Fig. 3.2). Their usage of Debye length as the characteristic length scale as compared to the film thickness used in this study leads to different dimensionless groups which can be mathematically adjusted without losing any physical details for comparing the results. Their various parameters can be recovered from the present parameters as,

$$\kappa = Wo \times De; \quad \eta = De; \quad u_{HS} = -u_{ref} \tag{3.3.15}$$

where κ is the dimensionless frequency, η is the dimensionless Debye length and u_{HS} is the Helmholtz-Smoluchowski slip velocity used as the reference velocity by Dutta and Beskok (2001). The excellent agreement between the velocity profiles obtained from the present model and the one extracted from Dutta and Beskok (2001) as reported in Fig. 3.2, justifies the success of non-Maxwell stress model in thin EDL systems.

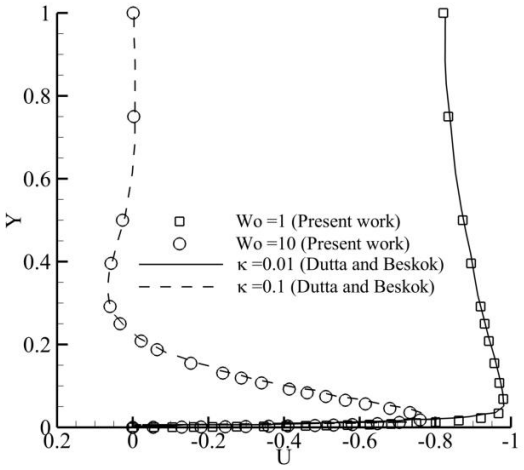

Figure 3.2.: Velocity profiles comparison with Dutta and Beskok (2001), where, $\kappa = Wo \times De$ is the dimensionless frequency used by them. Other fixed parameters are $De = 0.01$, $Z_R = 0$, $\gamma_R = 1$, $\Theta = \pi/2$.

For cases where the EDL extent is comparable to the characteristic dimensions of the flow, which in the present case is the film thickness h_0, the effect of Maxwell

stress modifying the shear stress balance criterion at the surface boundary is more pronounced. This leads to changes on the transverse velocity gradients as a function of the surface potential and potential field present in the bulk. In the absence of transverse velocity component, the distribution of such a gradient also corresponds to the absolute value of vorticity (ω_{abs}) field defined as $\omega_{abs} = |\nabla \times \mathbf{U}| = \partial U/\partial Y$, which can account for vorticity induced flow instabilities in the system. To study the effect of Maxwell stress model on vorticity distribution, a comparison between free-surface EOF models with and without Maxwell stress was performed (see Fig. 3.3). The vorticity profile of non-Maxwell stress model was taken from Chakraborty and Srivastava (2007), whose dimensionless parameters relate to the present parameters as mentioned in Eq. 3.3.15. It is seen from the figure that neglecting Maxwell stress can lead to significant underestimation of the vorticity strengths in the bulk. Also, for thick EDLs the strong presence of velocity gradients renders Helmholtz-Smoluchowski velocity a non-ideal slip condition at the liquid solid interface. In order to strengthen this argument, a further discussion on velocity scales is provided with different values of γ_R. The resulting velocity gradients lead to dispersion in thick EDL flows over the time and with the help of this study one can identify the regimes of applied frequency and electrolyte characteristics to avoid the dispersion effects in a time periodic EOF.

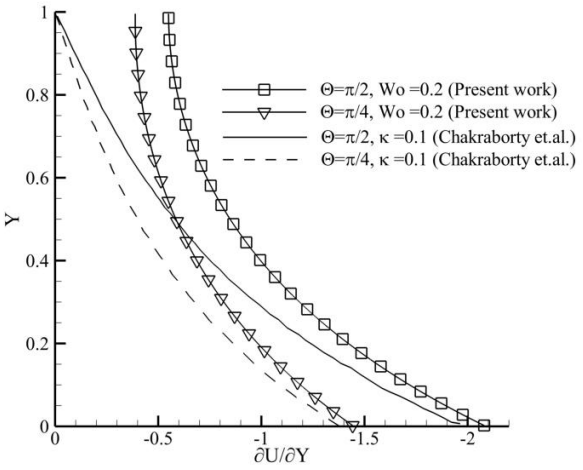

Figure 3.3.: Vorticity profile comparison of Maxwell stress and non-Maxwell stress models [Chakraborty and Srivastava (2007)]. The values of other fixed parameters are $De = 0.5$, $\alpha = 0.4278$, $Z_R = 0$, $\gamma_R = 1$.

As the ionic energy parameter, β, defines the relative strength of electrostatic energy of ions over their thermal energy, the changes in the velocity distribution due

to the relative interplay between the mentioned competing energies is significant. To demonstrate the effect of β, four cases have been considered with different values of the EDL thickness (De) and β (see Fig. 3.4). It is seen that for lower values of β the difference in the velocity distribution is significant for higher EDL thickness ($De = 0.1$). However, in the case of thin EDL, the difference is not noticeable. This also explains the reason why the Debye-Hückel linearization of Poisson-Boltzmann equation, which is valid for low values of β, successfully models the thin EDL potential distribution even over a large range of β. The above observation can also be explained by the fact that, when the thermal motion of ions dominates ($\beta < 1$), the electric actuation is diffused strongly in the EDL and hence the local velocity magnitude is reduced. This diffusion of the electrical actuation is enhanced if the EDL is thicker as the presence of a greater amount of space-charge distribution aides in more effective distribution of velocity in the liquid bulk.

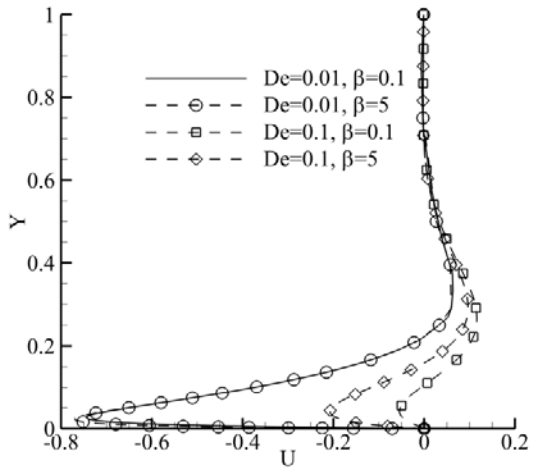

Figure 3.4.: Velocity profile with different values of the Debye number (De) and ionic energy parameter (β) for fixed values of Womersley number (Wo), electro-viscous ratio (γ_R), Z_R at time $\Theta = \pi/2$.

The electro-viscous ratio, γ_R, (see Eq. 3.3.3) is directly proportional to the amplitude of the applied oscillating electric field and hence, increment of which amplifies the flow velocity profile for a given fluid. This is clearly highlighted in Fig. 3.5 for the values $De = 0.01$ and $De = 0.1$. It can also be seen that the maximum value of the velocity obtained for a thin EDL case ($De = 0.01$) is greater than in the case with a thicker EDL ($De = 0.1$), which can be attributed to the fact that in the case of thick EDLs, the electrical energy mobilizes a greater space charge distribution than in the case of a thin EDL. This leads to a lower maximum kinetic energy of the

liquid within the EDL. Moreover, γ_R also represents a ratio of the classically used Helmholtz-Smoluchowski velocity (u_{HS}) as a reference velocity scale to the current velocity scale. It is interesting to note that u_{HS} can be used as a reference velocity scale ($\gamma_R = 1$) when (a) EDL is thin (see Fig. 3.5), (b) forcing frequency is smaller than the viscous relaxation frequency ($Wo < 1$) (see Fig. 3.6). In remaining cases, u_{HS} overestimates the characteristic velocity sometimes by an order of magnitude. Also, one can observe from Fig. 3.5 that the velocity oscillations propagate as a damped wave into the bulk. The extent of this bulk penetration of the damped velocity oscillations seem to be unaffected by the value of γ_R.

Taking a cue from the classical Stokes second problem, the typical penetration depth of momentum diffusion of oscillatory flows in a liquid can be estimated by the Stokes penetration depth δ_s. Typically, δ_s is a function of the forcing frequency as $\frac{\delta_s}{h_0} = \sqrt{\frac{\nu}{\omega h_0^2}} = \frac{1}{Wo}$, where Wo is the Womersley number representing the relative strength of temporal inertia over viscous force (see Eq. 3.3.3). This inverse relationship between the δ_s and Wo, is also observed in Fig. 3.6 which shows the velocity profiles as a function of Wo.

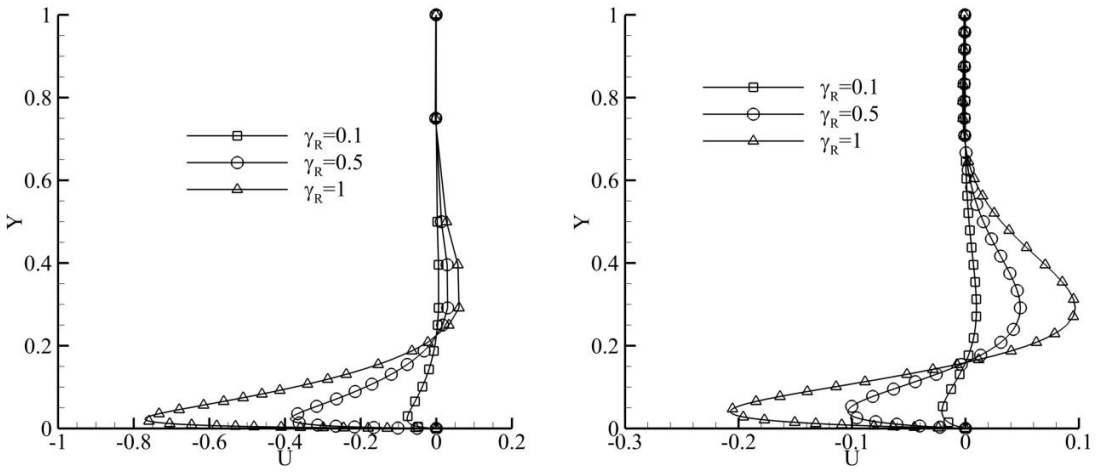

Figure 3.5.: Velocity distribution over the film thickness with different values of Electro-osmotic number, γ_R for $\beta = 5$, $Z_R = 0$, $Wo = 10$ at $\Theta = \pi/2$ with (a) $De = 0.01$ and (b) $De = 0.1$.

It is observed that decreasing Wo increases the Stokes penetration depth and in turn enhances the sharp changes in the velocity gradients near the wall. This also

results in a stronger diffusion of the near wall vorticity in the liquid bulk. However, upon increasing Wo, the viscous time lag of momentum propagation in the liquid also increases which leads to inflection points in the velocity profiles. Presence of such inflection points leads to extrema in the vorticity distribution yielding possible fluid mixing and instability [Davis (1976)]. It is also observed that the magnitude and extent of vorticity propagation is a strong function of the EDL thickness. This can be explained in terms of electrokinetic energy transfer over the extent of space charge distribution in the liquid. The thinner will be the space charge distribution, the stronger will be the velocity gradients.

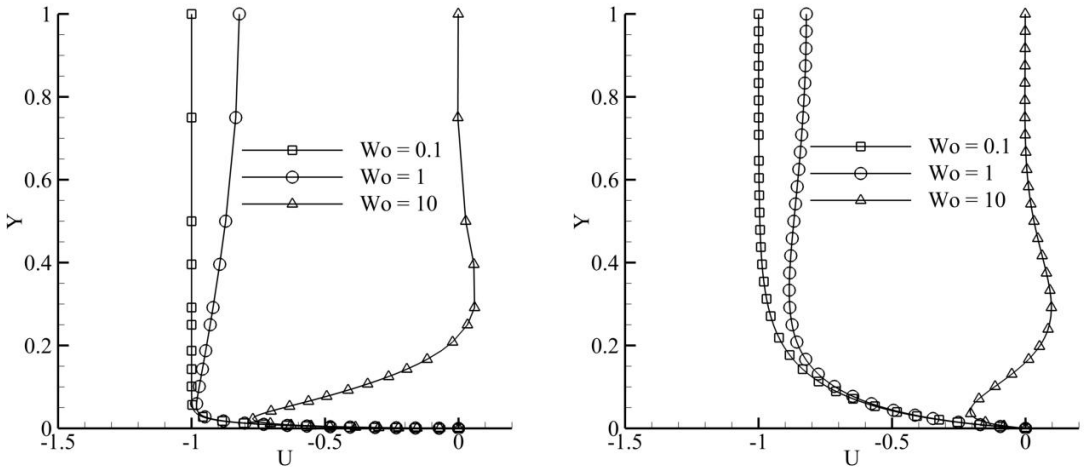

Figure 3.6.: Velocity distribution over the film thickness with different values of Wo and for fixed values of $\beta = 5$, $Z_R = 0$ and $\gamma_R = 1$ at $\Theta = \pi/2$ with (a) $De = 0.01$ and (b) $De = 0.1$

Interfacial polarity, Z_R, in the context of free surface flows has been demonstrated to be an important parameter determining the base state velocity profile presented in Fig. 3.7. One can see that the nature of velocity profile is a strong function of the interfacial polarity. The presence of strong velocity gradients is a marker of high dispersive fields present near the interface and at the wall. It is seen that the interfacial dispersion can be reduced by reducing the interfacial potential or charge distribution. Such an effect can be achieved by controlling the solvent pH and electrolytic concentrations or using non-electrolytic surfactants. The strong velocity gradients near the wall can be relaxed by using non-wettable surfaces which enhance velocity slip.

Another aspect of interfacial potential is the phase lag (see Eq. 3.3.13) between velocities at different transverse locations in the flow (see Fig. 3.7b). It is observed that upon reversing the polarity of the interface induces a phase lag of π in the interfacial velocity. However, the near-wall ($Y = 0.1$) and mid-film ($Y = 0.5$) velocities seem to be insensitive to the changes in the interfacial polarity. This reinforces the idea that the viscous diffusion, as represented by the Stokes penetration depth, has significant effect on the thin film dynamics under a time periodic actuation.

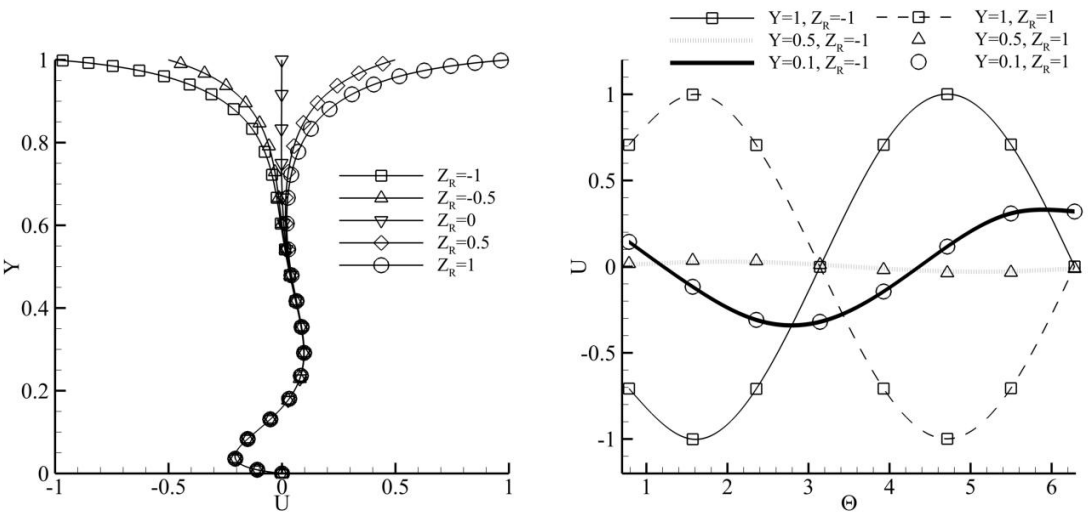

(a) (b)

Figure 3.7.: Velocity profile with fixed values of $De = 0.1$, $\beta = 5$, $\gamma_R = 1$ and $Wo = 10$ with (a) different values of interfacial polarity, Z_R at $\Theta = \pi/2$ and (b) at different times (Θ) and transverse locations (Y).

Upon observing the vorticity distribution in the fluid over a complete time cycle, one can get an idea of vorticity fluctuation and diffusion in the fluid bulk as a function of time (See Fig. 3.8). It is observed that the vorticity transport in the bulk is controlled by Wo and De. As high Wo reduces the rate of viscous diffusion, the fluid bulk is not affected by the time dependent fluctuations in the vorticity profile even when the EDL is thick. However, for lower Wo, the vorticity fluctuation is spread over the entire extent of the space charge distribution.

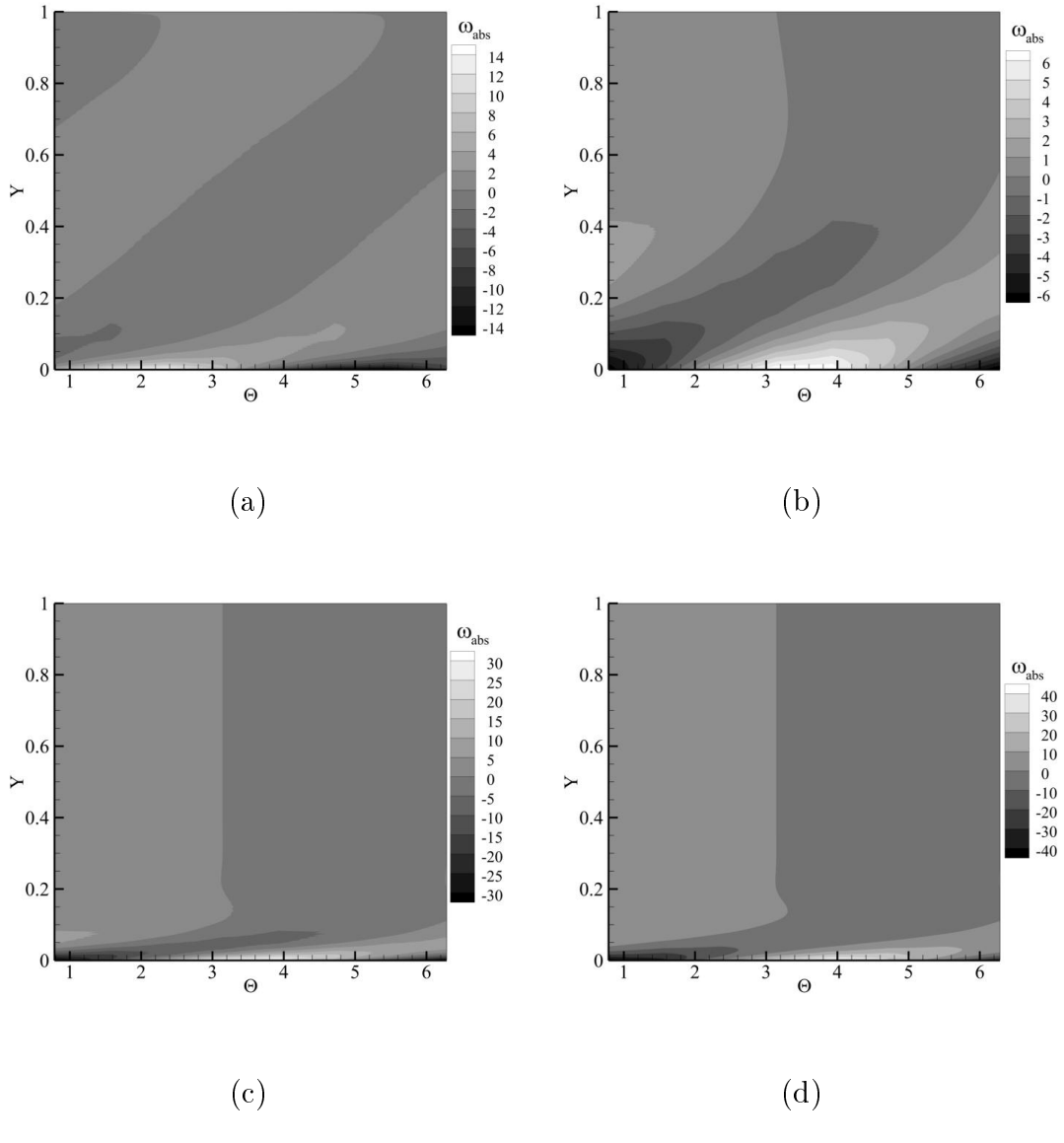

Figure 3.8.: Vorticity (ω_{abs}) distribution in the fluid over one complete time cycle ($\Theta \in (0, 2\pi)$). The values of fixed parameters are: $\gamma_R = 1$, $\beta = 5$, $Z_R = 1$ with (a) $De = 0.1$ and $Wo = 10$, (b) $De = 0.5$ and $Wo = 10$, (c) $De = 0.1$ and $Wo = 50$, (d) $De = 0.5$ and $Wo = 50$.

3.4. Free Surface Flows in Rectangular Geometry under a DC Electric Field

The common approach of 2D EOF models predicts the velocity profiles by ignoring the channel 3D confinement effects, and are useful when channel aspect ratios

are significantly larger than the EDL thickness. However, due to various microfabrication limitations and practical aspects of microfluidic devices, large aspect ratio microchannels are not very common. This requires a 3D analysis of the flow to understand the flow profiles especially when the channel dimensions are comparable to the EDL thickness. In this section, electro-osmotic flow of an aqueous electrolyte bounded by an inert gas on the top is studied in a rectangular microchannel and the role of interfacial potential and Maxwell stress generated dynamics are explored.

3.4.1. Mathematical Modeling

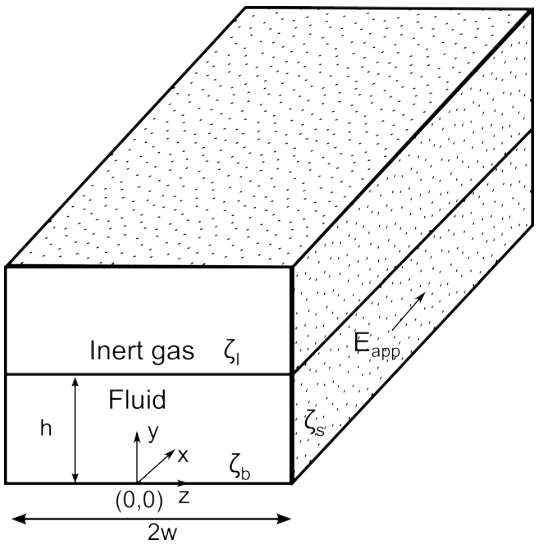

Figure 3.9.: Schematics of a rectangular channel under free-surface electro-osmotic flow.

The system under study consists of a conductive fluid having a planar interface with an inert gas in a microchannel with a rectangular cross-section. A Cartesian co-ordinate system is chosen to describe the channel geometry where the origin is set at the intersection of the bottom wall and the transverse line of symmetry (see Fig. 3.9). The width of the channel is taken as $2w$. The height of the conductive fluid is taken as h. The conductive fluid is considered to be a low concentration symmetric electrolytic solution with constant permittivity ($\varepsilon_{f,r}\varepsilon_0$). The inert gas is considered to be at constant pressure with a low permittivity ($\varepsilon_{g,r} \sim 1$) and low viscosity ($\mu_g \sim 0$) . The electrical double layer forms at the interface between the electrolyte and the bounding walls as well as at the liquid-gas interface. All the interfaces to the electrolytic solution develop zeta potentials, the magnitude of which depends upon the electrochemistry of liquid-gas and solid-liquid interactions.

The bottom wall zeta potential is taken as ζ_b, the side wall zeta potential is taken as ζ_s, and the liquid-gas interfacial zeta potential is taken as ζ_I. It is assumed that the external electric field has no effect on the zeta potentials. The bounding walls are considered to be rigid and a constant electric field is applied along the channel length (x-direction). Due to the symmetry of the system along $z = 0$, the governing equations will be solved for $0 \leq z \leq w$ and $0 \leq y \leq h$.

Electrostatic Potential Distribution

The space charge potential distribution in the electrolyte can be obtained from the classical Poisson-Boltzmann equation (PBE) (see Chapter 2) as,

$$\varepsilon_{f,r}\varepsilon_0 \nabla^2 \phi_{sc} = 2ez_0 C_0 sinh\left(\frac{ez_0\phi_{sc}}{k_B\theta}\right) \tag{3.4.1}$$

Upon using the scaling parameters as, $Y = y/D_h$, $Z = z/D_h$, $\Phi_{sc} = \phi_{sc}/\zeta_{ref}$ where $D_h = 4lh/(l+h)$ is the hydraulic diameter of an open rectangular duct and using Debye-Huckel linearization for small wall potentials ($\zeta_b \sim 25mV$), the governing equation for the electrostatic potential distribution in the EDL can be obtained as,

$$\frac{\partial^2 \Phi_{sc}}{\partial Y^2} + \frac{\partial^2 \Phi_{sc}}{\partial Z^2} = \frac{\Phi_{sc}}{De^2} \tag{3.4.2}$$

where, $De = \lambda_D/D_h$ is Debye number, which represents the relative extent of the EDL as compared to the geometric length scale with $\lambda_D = \sqrt{\varepsilon_{f,r}\varepsilon_0 k_B T/(2\rho_0 z^2 e^2)}$. The electrostatic potential distribution satisfies the following boundary conditions,

$$\begin{aligned}
&\frac{\partial \Phi_{sc}}{\partial Z}(Y,0) = 0 \\
&\Phi_{sc}(Y,W) = \bar{\zeta}_s \\
&\Phi_{sc}(0,Z) = \bar{\zeta}_b \\
&\Phi_{sc}(H,Z) = \bar{\zeta}_I
\end{aligned} \tag{3.4.3}$$

where, $W = w/D_h$, $H = h/D_h$, $\bar{\zeta}_s = \zeta_s/\zeta_{ref}$, $\bar{\zeta}_b = \zeta_b/\zeta_{ref}$ and $\bar{\zeta}_I = \zeta_I/\zeta_{ref}$. The solution of Eqs. 3.4.2 and 3.4.3 can be obtained by separation of variables as,

$$\begin{aligned}
\Phi_{sc}(Y,Z) = &\sum_{m=1}^{\infty} \frac{2(-1)^{m-1}\left[\bar{\zeta}_i sinh\left(\sqrt{\frac{1}{De^2}+\lambda_m^2}Y\right)+\bar{\zeta}_b sinh\left(\sqrt{\frac{1}{De^2}+\lambda_m^2}(H-Y)\right)\right]cos(\lambda_m Z)}{W\lambda_m sinh\left(H_1\sqrt{\frac{1}{De^2}+\lambda_m^2}\right)} \\
&+\sum_{n=1}^{\infty} \frac{2\left(1+(-1)^{n-1}\right)\bar{\zeta}_s cosh\left(\sqrt{\frac{1}{De^2}+\lambda_n^2}Z\right)sin(\lambda_n Y)}{H\lambda_n sinh\left(\sqrt{\frac{1}{De^2}+\lambda_n^2}W\right)}
\end{aligned} \tag{3.4.4}$$

where, $\lambda_m = (2m-1)\,\pi/(2W)$ and $\lambda_n = n\pi/H$. The electric potential due to the external field can be calculated as,

$$\Phi_{app}(X) = -\int \frac{E_{app} D_h}{\zeta_{ref}} dX = -\frac{X}{E_R} \tag{3.4.5}$$

where, $X = x/D_h$, and $E_R = \frac{\zeta_{ref}}{E_{app} D_h}$ is the ratio of the electric potential due to charge polarization in the electrolyte over the electric potential due to the externally applied electric field. Hence, the net electric potential field in the fluid is,

$$\Phi(X, Y, Z) = \Phi_{app}(X) + \Phi_{sc}(Y, Z) \tag{3.4.6}$$

Velocity Distribution

Since the top fluid is considered to be a low permittivity, low viscosity inert gas at a constant pressure, it can be considered at rest. An external electric field acting on a space charge distribution in the conductive fluid generates a Maxwell stress. This Maxwell stress along with the hydrodynamic stress results into a net stress distribution in the fluid (see Chapter 2). Under such an actuation, for a Newtonian fluid with incompressible, steady and laminar flow assumption, and in the absence of an external pressure gradient the momentum equation can be written as,

$$\frac{\partial^2 u}{\partial y^2} + \frac{\partial^2 u}{\partial z^2} = \varepsilon_{f,r}\varepsilon_0 \frac{\partial \phi}{\partial x}\left(\frac{\partial^2 \phi}{\partial y^2} + \frac{\partial^2 \phi}{\partial z^2}\right) \tag{3.4.7}$$

The boundary condition at the walls ($y = 0$ and $z = \pm w$) is taken to be a no-slip condition as,

$$\begin{aligned} u(0, z) &= 0 \\ u(y, w) &= 0 \end{aligned} \tag{3.4.8}$$

The continuity of shear stress at the gas-fluid interface ($y = h$),

$$\frac{\partial u}{\partial y}(h, z) - \varepsilon_{f,r}\varepsilon_0 \frac{\partial \phi_{sc}}{\partial y}(h, z) = 0 \tag{3.4.9}$$

At the symmetry plane ($z = 0$), the symmetry condition leads to,

$$\frac{\partial u}{\partial z}(y, 0) = 0 \tag{3.4.10}$$

Further, the dimensionless governing equation can be written as,

$$\frac{\partial^2 U}{\partial Y^2} + \frac{\partial^2 U}{\partial Z^2} = \gamma_R \left(\frac{\partial^2 \Phi_{sc}}{\partial Y^2} + \frac{\partial^2 \Phi_{sc}}{\partial Z^2}\right) \tag{3.4.11}$$

where, $U = \frac{u}{u_{ref}}$. The corresponding dimensionless boundary conditions are,

$$\begin{aligned} U(0,Z) &= 0 \\ U(Y,W) &= 0 \\ \frac{\partial U}{\partial Y}(H,Z) - \gamma_R \frac{\partial \Phi_{sc}}{\partial Y}(H,Z) &= 0 \\ \frac{\partial U}{\partial Z}(Y,0) &= 0 \end{aligned} \tag{3.4.12}$$

The solution to the system of Eqs. 3.4.11 and 3.4.12 can be obtained by using the method of separation of variables and the resulting velocity can be written as,

$$\begin{aligned} U(Y,Z) = & \sum_{m=1}^{\infty} \frac{2(-1)^{m-1}\gamma_R\left[\bar{\zeta}_I sinh\left(\sqrt{\frac{1}{De^2}+\lambda_m^2}Y\right)+\bar{\zeta}_b sinh\left(\sqrt{\frac{1}{De^2}+\lambda_m^2}(H-Y)\right)\right]cos(\lambda_m Z)}{W\lambda_m sinh\left(H_1\sqrt{\frac{1}{De^2}+\lambda_m^2}\right)} \\ & + \sum_{n=1}^{\infty} \frac{2\left(1+(-1)^{n-1}\right)\gamma_R\bar{\zeta}_s cosh\left(\sqrt{\frac{1}{De^2}+\lambda_n^2}Z\right)sin(\lambda_n Y)}{H\lambda_n cosh\left(\sqrt{\frac{1}{De^2}+\lambda_n^2}W\right)} \\ & + \sum_{m=1}^{\infty} \frac{2(-1)^m\gamma_R\bar{\zeta}_b cosh(\lambda_m(H-Y))cos(\lambda_m Z)}{H\lambda_n cosh\left(\sqrt{\frac{1}{De^2}+\lambda_n^2}W\right)} \\ & - \sum_{n=1}^{\infty} \frac{2\left(1+(-1)^{n-1}\right)\gamma_R\bar{\zeta}_s cosh(\lambda_n Z)sin(\lambda_n Y)}{H\lambda_n cosh(\lambda_n W)} \end{aligned} \tag{3.4.13}$$

The corresponding flow rate in the rectangular cavity can be obtained by,

$$Q = 2\int_0^W \int_0^H U(Y,Z)\, dY\, dZ \tag{3.4.14}$$

3.4.2. Results and Discussions

Owing to the plug like velocity distribution of EOF in the commonly observed thin EDL limit, the most simplified approach towards modeling an EOF is by solving Stokes equation in the presence of Helmholtz-Smoluchowski slip velocity ($u_{HS} = -\varepsilon_{f,r}\varepsilon_0\zeta_b E_{app}/\mu$) at the wall boundaries. So, it it natural to consider the reference velocity as u_{HS} and reference potential as ζ_b which also helps in performing a comparative analysis with the previous works. Such an assumption leads to $\gamma_R = -\frac{u_{HS}}{u_{ref}} = 1$.

Using a modified stress term, which includes the effects of both hydrodynamic and electric field generated stresses, one obtains a body force term in the momentum equations and a modified free surface shear stress jump condition. To observe the effect of Maxwell stress in a free surface electro-osmotic flow, a comparison of velocity profiles with and without modified stress term is presented where the case without interfacial Maxwell stress is taken from Gao et al. (2005b) (see Fig. 3.10). The

classical hydrodynamic stress free condition at the free surface enforces shear stress free condition at the interface, which can also be expressed by a zero velocity gradient in the direction normal to the free surface. It can be seen that the interfacial Maxwell stress significantly affects the velocity distribution in the fluid by introducing a non-zero velocity gradient at the free surface ($Y = H$). The non-zero velocity gradient observed at the free surface, can be associated with a hydrodynamic shear, which is balanced out by an equal and opposite interfacial Maxwell stress. Such finite velocity gradients can result into a dispersive flow, which is not observed in a classical EOF. It can also be observed that the effect of Maxwell stress on velocity distribution is greatly enhanced when the channel aspect ratio ($H/2W$) is low and the EDL thickness is comparable to the characteristic length scale.

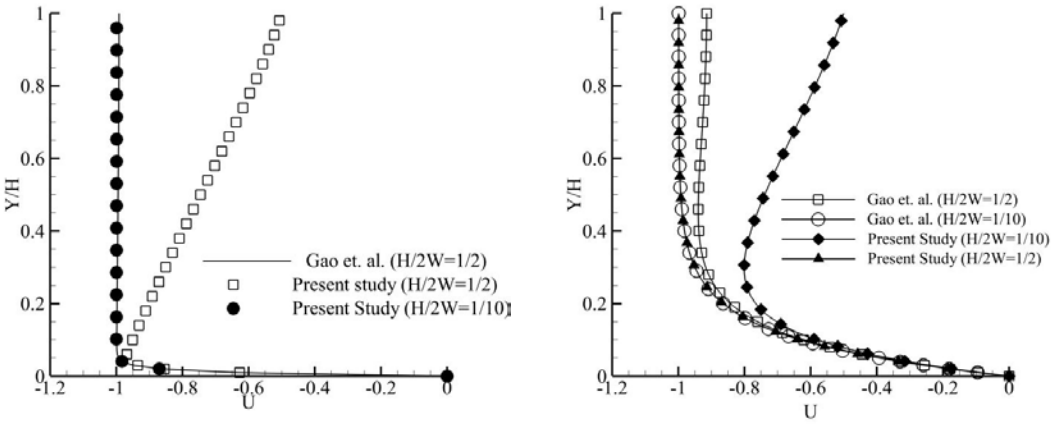

(a) (b)

Figure 3.10.: Velocity profiles for cases with and without interfacial Maxwell stress at the symmetry axis of the channel ($Z = 0$). The case without Maxwell stress was taken from a study by Gao et al. (2005b). The values of fixed parameters are $\gamma_R = 1$, $\overline{\zeta}_s = 1$, $\overline{\zeta}_I = 0$ and (a) $De = 0.01$ (b) $De = 0.1$. The free surface is at $Y = H$.

From the velocity solution as obtained in Eq. 3.4.13, it can be seen that the fluid velocity distribution is proportional to the Electro-viscous number, γ_R, showing the direct dependence of EOF velocity on the applied electric field and substrate zeta petential. However, the dependence of fluid velocity on other flow parameters such as, EDL thickness, wall and interfacial zeta potential, and channel geometry is not obvious. The role of each individual parameter on the velocity distribution in the rectangular channel is discussed below.

Effect of the EDL thickness

The thickness of the EDL which is usually expressed as the Debye length (λ_D) as compared to the flow length scale which in this study is the hydraulic diameter (D_h) is represented by the Debye number (De). The extent of the EDL defines the geometrical extent of the electrical field generated body force on the fluid. When the EDL is thin the charge polarization occurs over a short distance and hence results into very high velocity gradients. This results into high magnitudes of velocity, as compared to the thicker EDL case where the velocity gradients are lesser. The above observation is evident from Fig. 3.11 where velocity contours are presented for two different values of the Debye number, namely, 0.1 and 0.01 where values of channel aspect ratio, electric field strength, wall and interfacial zeta potential are fixed.

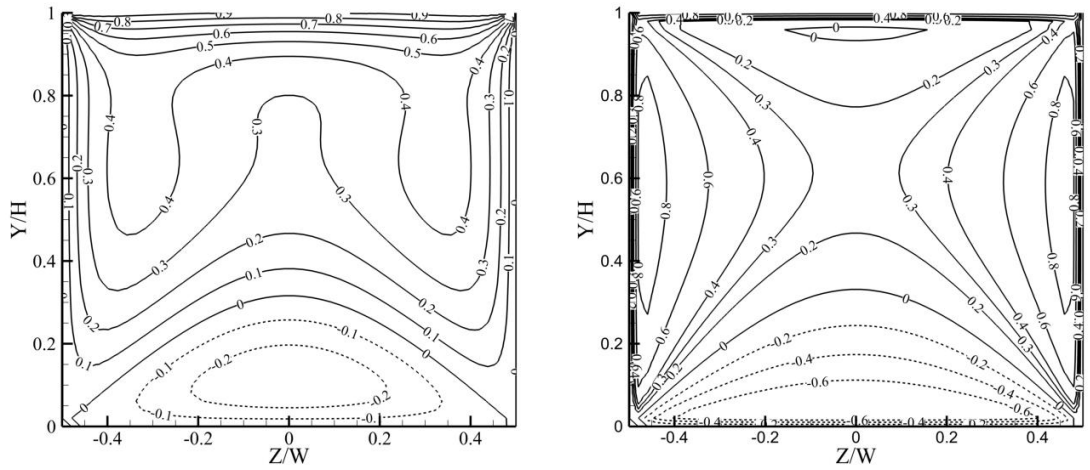

(a) (b)

Figure 3.11.: Velocity contours in the Y-Z plane for different Debye numbers where $\gamma_R = 1$, $\overline{\zeta}_s = -1$, $\overline{\zeta}_I = 1$, $H/2W = 1$ and (a) $De = 0.1$, (b) $De = 0.01$. Solid lines show positive velocity and dashed lines show negative velocity values. The free surface is at $Y = H$.

Effect of the channel aspect ratio

The channel aspect ratio ($H/2W$) determines the effect of channel confinement on the flow characteristics. In the contrast with the EDL thickness which is determined by the electrochemistry of the system, the channel geometry is controlled by the limitations of the manufacturing process involved and the physical properties of the

material used. From Fig. 3.12, it is seen that the channel aspect ratio controls the effect of side wall generated flow on the overall velocity distribution and in some cases on the centerline velocity profile. If the channel aspect ratio is small, the side wall generated dynamics have a strong effect on the overall velocity profile whereas if the channel has a larger aspect ratio, the dynamics at the top and bottom boundaries dominate the flow profile. In the Fig. 3.12, the Debye number is taken as 0.1 so that the side wall generated EOF is more apparent.

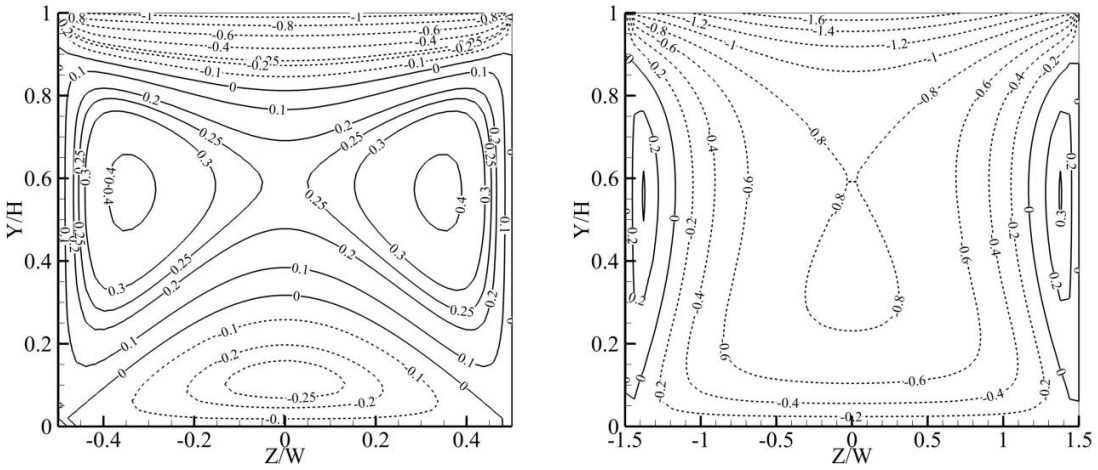

(a) (b)

Figure 3.12.: Velocity contours on the Y-Z plane for different aspect ratios where $De = 0.1$, $\gamma_R = 1$, $\overline{\zeta}_s = -1$, $\overline{\zeta}_I = -1$ and (a) $H/2W = 1$, (b) $H/2W = 1/3$. Solid lines show positive velocity and dashed lines show negative velocity values. The free surface is at $Y = H$.

Effect of wall and interfacial zeta potential

The magnitude and polarity of wall and interfacial zeta potential dictate the dominating polarity of charge distribution near the wall or the interface over which the fluid actuating electric field operates. From the Helmholtz-Smoluchowski relation, one can see that for a positive value of the electric field, the direction of the near wall velocity is opposite to that of the wall zeta potential (see Fig. 3.12a and Fig. 3.13a). However, the direction of the interfacial velocity follows that of the polarity of the interfacial zeta potential. This interesting observation can be attributed to the basic structure of the EDL where the ions contributing to the zeta potential of the substrate are strongly bonded to the surface. For a rigid and stationary substrate, this

layer of immobile ions is followed by a layer of mobile oppositely charged ions. For example, if the surface has a negative zeta potential, the mobile ionic layer will be positively charged and under a positive electric field will produce a positive velocity. If the surface is positively charged, the mobile ionic layer will be negatively charged and will produce a negative velocity field under a positive electric field. However, at the interface, there is no rigid and immobile layer of ions and hence the velocity direction is the same as the polarity of the interfacial potential under a positive electric field. This observation is evident in all the velocity plots. From Fig. 3.13b, one can see that the polarity of the interfacial potential has a strong influence on the centerline velocity profile and can be controlled to produce desired flow-rates in microdevices.

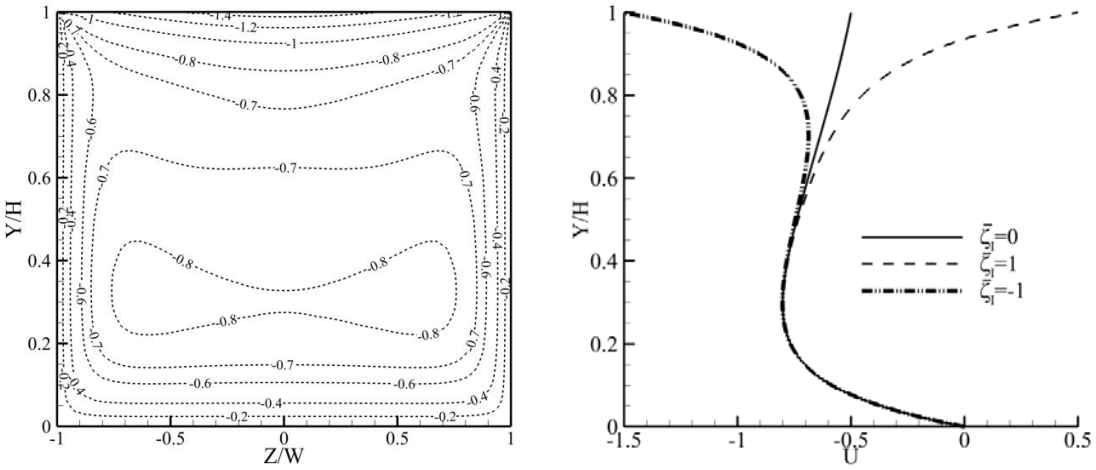

(a) (b)

Figure 3.13.: (a) Velocity contours on the Y-Z plane where $De = 0.1$, $\gamma_R = 1$, $\overline{\zeta}_s = 1$, $\overline{\zeta}_I = -1$ and (b) Centerline velocity profile (at $Z = 0$) where $De = 0.1$, $\gamma_R = 1$,$\overline{\zeta}_s = 1$, $H/2W = 1/2$ for different values of $\overline{\zeta}_I$.

Flow rate

The net flow rate variation over a range of De manifests various regimes observed in such systems (see Fig. 3.14). It is remarkable to observe that upon changing the Debye length, which is a function of the salt concentration of the system, one can enhance, diminish, or in some cases, reverse the flow rate in microdevices. The flow reversal observed can be attributed to the combined effects of interfacial zeta potential ($\overline{\zeta}_I$) and Debye length. It can be seen from Fig. 3.11 that a positive $\overline{\zeta}_I$

induces a positive interfacial velocity. However, the strength of the extent of this positive velocity in the bulk is delimited by the Debye length, which represents the extent of the polarized cloud of mobile ions. Moreover, for large Debye lengths ($De \geq 0.1$) the positive velocity induced by a positively charged free surface has greater influence over bulk dynamics as compared to the electro-osmotic velocities induced near the walls. This is also evident from Fig. 3.14a where for a positive and sufficiently large Debye length ($De \geq 0.4$), the flow rate is positive irrespective of the polarity of the side walls. It is also observed that the asymptotic nature of the flow rate dependence helps to identify the regions of maximum and minimum variation of the magnitude of flow rate. This asymptotic variation of flow rate can be attributed to the two prominent opposing mechanisms viz. electro-osmotic actuation and viscous dissipation due to the wall confinements. Such a study helps to control the fluctuations in the electro-osmotically generated flow rates which occur due to the changes in ionic concentrations and pH variations which further culminates into Debye length or zeta potential variations.

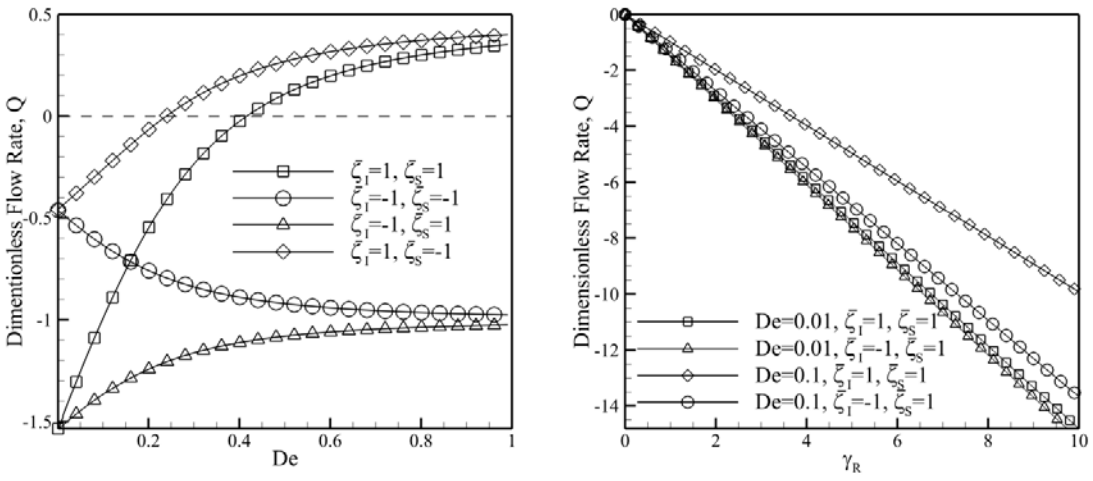

(a) (b)

Figure 3.14.: Dimensionless flow rate variation with (a) Debye number, De for a fixed aspect ratio, $H/2W = 1$ and γ_R (b) Electro-viscous number (γ_R), for a fixed aspect ratio, $H/2W = 1$.

From Fig. 3.14b, it is observed that a reversed polarity of interfacial zeta potential has little effect on the flow rate variation when the Debye layer is thin ($De = 0.01$). However, the reversed polarity of side wall zeta potential changes the flow rate significantly for thin Debye layers (see Fig. 3.14a). The thin Debye layer case is

special as it is the most commonly observed phenomena in experimental microfluidics. Moreover, recent advances allow specific treatment of channel walls to alter their electrochemical properties, so that one can modulate the substrate zeta potential to overcome the limitations posed on flow rate by channel geometry through micro-fabrication constraints or the magnitude of the actuating field.

3.5. Conclusion

The present work focuses on the role of steady and time-dependent Maxwell stress in free surface electro-osmotic flows. It was highlighted that the Maxwell stress generated dynamics introduces significant velocity gradients at the free surface as compared to the studies where interfacial Maxwell stress was not taken into account. Moreover, it was observed that for thick EDLs (or very thin films) the non-Maxwell stress model significantly underestimates the velocity and vorticity distributions in the fluid film. Such gradients are instrumental in the interfacial instability under a time-periodic actuation. The bulk penetration of near wall oscillations is inversely proportional to the forcing frequency. At lower frequencies, we observe a significant suppression of velocity dispersion which asymptotes to the classical dispersion free velocity in a DC electro-osmotic flow. By the variation of interfacial polarity one can not only control the interfacial velocity and the rate of shear transfer but also establish a significant phase difference in fluid velocity at different transverse locations in the fluid which enhances the dispersion effects and can be effectively used in controlled species transport in microfluidic devices. Further, in order to study the effect of interfacial Maxwell stresses in realistic rectangular channels, the solution of a free surface EOF in a microchannel of rectangular cross-section was achieved analytically. By taking into account a complete expression of the boundary condition at the free surface that includes the Maxwell stress at this interface, a parametric analysis of the flow in terms of the EDL thickness, channel aspect ratio and different fluid-fluid and solid-fluid interfacial zeta potential was carried out. With the help of two-dimensional velocity contours, it has been shown that the bounding walls have a significant effect on the velocity distribution in a rectangular microchannel. The flow controlling parameters in an EOF are not only the electro-chemical properties of the involved fluid and electrolytes which control the EDL thickness and wall and interfacial zeta potentials but also the geometry of the channel through the channel aspect ratio. Such a study helps identifying proper control parameters for achieving a desired flow rate and velocity distribution in a microfluidic device.

4. Long Wave Analysis of Thin Films Stability in Electrokinetics

4.1. Overview

The ever growing attention towards understanding the dynamics of thin liquid films can be attributed to their ubiquitous presence all around us. Starting from biological entities like tear film in the eyes or mucous linings in the organs, they are also found in man-made objects like bearings, paints, adhesives etc. As widespread is the availability of thin films in the nature, equally extensive are the properties of the constituent fluids and their physico-chemical interactions with their environments. One of the major challenges in the film dynamics is to understand and model their interfacial evolution and stability thresholds under the influence of a wide range of inherent parameters like surface tension, viscosity, van der Waals forces and imposed static and time-dependent phenomena like gravity, temperature gradients and electric fields. Owing to the complex interaction of the mentioned phenomena, a detailed and all-inclusive analysis is required, which is not easy and still awaited. Creating and maintaining thin aqueous films is a challenging task as one has to understand the roles of various mentioned dynamic phenomena at work that contribute to its rupture.

The role of hydrodynamics in film stability has been investigated in a great detail in the literature but most of the related studies focus on a homogeneous fluid without any other dispersed phase. Sometimes the role of the dispersed phase is limited to modify the surface tension, which is used in the classical dispersion relationships (characteristic stability equations). When the fluid in question contains ionic species (either due to self-dissociation of the solvent or dissolved ions), their contribution to film stability is relatively underexplored in the existing literature. To a large extent, the role of ions is again limited to surface tension modification, which for low concentrations can be safely ignored. However, near the bounding interfaces of thin films the ionic distribution is not uniform and electro-neutrality is not valid (see Chapter 2). When an electric field is applied to such a film, the Coulombic forces acting on this net ionic charge distribution actuates a flow, also called as Electro-Osmotic Flow (EOF). Stability of fluid interfaces under EOF has been a wide field of research in the past decade [Lin (2009); Zaltzman and Rubinstein

(2007); Rubinstein and Leshansky (2011); Sounart and Baygents (2007); Santos and Storey (2008)], a variety of stability models have been presented, discussing the effects of flow-actuating parameters, along with substantial experimental evidence to validate the theoretical predictions [Oddy et al. (2001); Posner and Santiago (2006); Oddy and Santiago (2005); CHEN et al. (2005)]. Most of the mentioned studies have been concentrated in the domain where the Electrical Double Layer (EDL) is negligible as compared to the characteristic length-scale. In such domains, the effect of the EDL on the flow is modeled using a slip velocity, which is obtained by the classical Helmholtz-Smoluchowski formulation and the bulk of the fluid remains electro-neutral. This approximation has been substantially helpful to design the flow and mixing process in modern microfluidic devices. However, with the technology of miniaturization foraying in the nanometric length scale with some applications like controlled delivery of non-conducting liquids in microfluidics devices, patterned conformal coatings, and control of thin films on electrostatic film radiators in space applications [Kim et al. (1992)], the fluid dynamics within the limits of the EDL can not be ignored. It has been established that new modes of instability can be observed when the Debye length is comparable to the film thickness [Qian et al. (2009)]. In some of the earlier works [Qian et al. (2009); Sadiq and Joo (2009); Joo (2008); Choi et al. (2010)], the effects of electric field strength, surface tension and intermolecular van der Waals force on free surface instability, where the length scale is of the order of the Debye length have been discussed. However, the effect of electric field generated stress (Maxwell stress) at the free surface has been overlooked. This Maxwell stress at the free surface is engendered due to the presence of free charges, the magnitude of which depends upon the fluid properties and substrate fluid interactions. It has been recently shown that due to the Maxwell stress, the free surface has an active role in electro-osmotic flows and should not be treated as a passive entity [Choi et al. (2010)].

In this chapter, the stability of free surface under DC and AC electro-osmotic flow in thin liquid films is investigated, where the film thickness can be varied over a range of electrical double layer thickness while considering the relative contribution from the van der Waals forces. The role of interfacial Maxwell stress on thin film stability is highlighted. This configuration gives some interesting insights into the physics of free surface stability at a scale where various competing forces such as Coulombic force, van der Waals force and surface tension come into play. The effects of the mentioned forces is incorporated in the Navier-Stokes equations and linear stability analysis of the resulting governing equations is performed to obtain the Orr-Sommerfeld equations. Parametric dependence of interfacial stability on surface tension, disjoining pressure, applied electric field, substrate zeta potential, free surface potential, film thickness and Debye length is explored. The characteristic stability curve of the system is obtained through an asymptotic analysis of the Orr-Sommerfeld equations in the long wave limit. These equations are solved by the asymptotic long wave expansion method of Yih (1963), as for thin viscous films, the instability is found to occur at long wavelengths [Oron and Bankoff (1997)].

This chapter is divided in three sections. In the first section, the characteristics of the physical system under investigation is presented. The contributions of various parameters to the governing equations are also worked out, and a generalized set of governing equations is presented. In the second section, linear stability analysis of DC EOF system is performed and the characteristic stability curve is obtained as a solution of the Orr-Sommerfeld equations while the role of various parameters is discussed. Finally, linear stability analysis of AC EOF system is performed followed by an extensive discussion on the parametric dependence of the stability of the system.

4.2. Thin film stability under DC EOF

The system under study consists of a thin electrolyte film spread over a rigid solid substrate exposed to an inert gaseous atmosphere (see Fig. 3.1). The film thickness is denoted by h. The dynamics of such a film is studied under the effect of a longitudinal oscillating electric field, $\mathbf{E_{app}} = E_0\mathbf{i}$, where E_0 is the magnitude of the applied electric field. The electrolyte concentration in this study is considered to be small enough in magnitude ($\sim 0.1 - 10mM$) in order to neglect the liquid property changes due to Joules heating [Cetin and Li (2008)], even in the case of an applied electric field of large amplitude. The low electrolyte concentration also avoids complexities in flow modeling by reducing the nonlinear dependence of electrophoretic mobility of ions on the sparse space-charge distribution [Wei and Patey (1991); Lorenz and Travesset (2007); Borukhov et al. (1995); Yossifon et al. (2009); Fedorov and Kornyshev (2008); Dufreche et al. (2005); Song and Kim (2011)]. The solid substrate zeta potential is represented as ζ_b, which is a function of the substrate-fluid interaction, ionic concentration and pH of the solution [Kirby and Hasselbrink (2004a)]. The liquid surface exposed to a gaseous environment develops a charge which is a function of various parameters like ionic concentration, pH of the solution and valence of the ions involved [Manciu and Ruckenstein (2012); Li and Somasundaran (1991); Gray-Weale and Beattie (2009)]. The associated zeta potential (ζ_I) has been found to vary over a wide range in the reported literature [Graciaa et al. (1995); Yang et al. (2001); Choi et al. (2011)].

4.2.1. Electric Potential Field

The total electric potential in dimensionless form in the conductive thin film system can be written as (see Eq. 3.3.2),

$$\begin{aligned}\Phi(X,Y) &= \Phi_{app}(X) + \Phi_{sc}(Y) \\ &= -\frac{X}{E_R} + \frac{1}{sinh\left(\frac{H}{De}\right)}\left\{Z_R sinh\left(\frac{Y}{De}\right) + sinh\left(\frac{H-Y}{De}\right)\right\} \end{aligned} \tag{4.2.1}$$

The corresponding electric field can be calculated as $\mathbf{E} = -\nabla\phi$.

4.2.2. Hydrodynamic Equations

Considering a Newtonian fluid under incompressible flow in the absence of an externally applied pressure gradient, the conservation of mass and momentum equations can be written as,

$$\nabla \cdot \mathbf{u} = 0 \tag{4.2.2}$$

$$\rho\left[\frac{\partial \mathbf{u}}{\partial t} + (\mathbf{u}\cdot\nabla)\,\mathbf{u}\right] = -\nabla p_d + \nabla\cdot\underline{\underline{\boldsymbol{\Sigma}}}^{\mathbf{T}} \tag{4.2.3}$$

where, p_d is the disjoining pressure. In situations involving thin films where the Debye length is of the order of the film thickness, the effect of intermolecular interactions cannot be ignored. This intermolecular interaction manifests itself in the form of a disjoining pressure term in momentum equations. It is represented as a pressure term in the momentum equations (see Chapter 2) and its dominant molecular component is defined as,

$$p_d = -\frac{a}{6\pi h^3} \tag{4.2.4}$$

where, a is the Hamaker's constant and h is the film thickness.
At the solid substrate ($y = 0$), no-slip and no-penetration conditions are assumed. At the free surface, which is located at $y = h(x,t)$, with an equilibrium height of h_0, the jump of shear and normal stresses can be respectively written as,

$$\left[\mathbf{t}\cdot\underline{\underline{\boldsymbol{\Sigma}}}^{\mathbf{T}}\cdot\mathbf{n}\right] = 0 \tag{4.2.5}$$

$$\left[\mathbf{n}\cdot\underline{\underline{\boldsymbol{\Sigma}}}^{\mathbf{T}}\cdot\mathbf{n}\right] = \gamma\kappa \tag{4.2.6}$$

where, $\gamma\kappa$ is the capillary force with γ being the surface tension and κ the local double mean curvature of the interface. The corresponding dimensionless conservation equations are written using the scaling parameters as, $\Theta = \omega_{ref}t$ with, $\omega_{ref} = \frac{1}{\tau_{ref}}$, where, τ_{ref} is the reference time scale, $U = \frac{u}{u_{ref}}$, $V = \frac{v}{u_{ref}}$, and $P = \frac{ph_0}{\mu u_{ref}}$ as,

Continuity:

$$\frac{\partial U}{\partial X} + \frac{\partial V}{\partial Y} = 0 \tag{4.2.7}$$

Momentum:

$$Wo^2\frac{\partial U}{\partial \Theta} + ReU\frac{\partial U}{\partial X} + ReV\frac{\partial U}{\partial Y} = -\frac{\partial P}{\partial X} + \frac{A}{H^4}\frac{\partial H}{\partial X} + \frac{\partial^2 U}{\partial X^2} + \frac{\partial^2 U}{\partial Y^2} + \gamma_R E_R\frac{\partial \Phi}{\partial X}\frac{\partial^2 \Phi}{\partial Y^2} \tag{4.2.8}$$

$$Wo^2\frac{\partial V}{\partial \Theta}+ReU\frac{\partial V}{\partial X}+ReV\frac{\partial V}{\partial Y}=-\frac{\partial P}{\partial Y}+\frac{\partial^2 V}{\partial X^2}+\frac{\partial^2 V}{\partial Y^2}+\gamma_R E_R\frac{\partial \Phi}{\partial Y}\frac{\partial^2 \Phi}{\partial Y^2} \quad (4.2.9)$$

where, $Wo=\sqrt{\frac{\omega_{ref}h_0^2}{\nu}}$ is the Womersley number expressing the relative strength of temporal inertial force over the viscous dissipation force, $Re=\frac{\rho u_{ref}h_0}{\mu}$ is the characteristic Reynolds number, $A=\frac{a}{2\pi h_0^2\mu u_{ref}}$ is the dimensionless Hamaker constant. The dimensionless boundary conditions at the wall ($Y=0$) are no-slip and no-penetration conditions,

$$U(0,\Theta)=V(0,\Theta)=0 \quad (4.2.10)$$

At the free surface, $Y=H(X,\Theta)$, the dimensionless continuity of tangential and normal stress are, respectively,

$$\begin{aligned}&\left[\left(\frac{\partial U}{\partial Y}+\frac{\partial V}{\partial X}\right)\left\{1-\left(\frac{\partial H}{\partial X}\right)^2\right\}-4\frac{\partial H}{\partial X}\frac{\partial U}{\partial X}\right]\\ &+\gamma_R E_R\left[\frac{\partial \Phi}{\partial X}\frac{\partial \Phi}{\partial Y}\left\{1-\left(\frac{\partial H}{\partial X}\right)^2\right\}-\frac{\partial H}{\partial X}\left\{\left(\frac{\partial \Phi}{\partial X}\right)^2-\left(\frac{\partial \Phi}{\partial Y}\right)^2\right\}\right] \;=\; 0\end{aligned} \quad (4.2.11)$$

$$\begin{aligned}&-\left[P+\frac{\gamma_R E_R}{2}\left\{\left(\frac{\partial \Phi}{\partial X}\right)^2+\left(\frac{\partial \Phi}{\partial Y}\right)^2\right\}\right]\\ &+\frac{2}{\left\{1+\left(\frac{\partial H}{\partial X}\right)^2\right\}}\left[\frac{\partial U}{\partial X}\left\{\left(\frac{\partial H}{\partial X}\right)^2-1\right\}-\frac{\partial H}{\partial X}\left(\frac{\partial U}{\partial Y}+\frac{\partial V}{\partial X}\right)\right]\\ &+\frac{\gamma_R E_R}{\left\{1+\left(\frac{\partial H}{\partial X}\right)^2\right\}}\left\{\left(\frac{\partial \Phi}{\partial X}\right)^2\left(\frac{\partial H}{\partial X}\right)^2+\left(\frac{\partial \Phi}{\partial Y}\right)^2\right\}\\ &-\frac{2\gamma_R E_R}{\left\{1+\left(\frac{\partial H}{\partial X}\right)^2\right\}}\frac{\partial H}{\partial X}\frac{\partial \Phi}{\partial X}\frac{\partial \Phi}{\partial Y} \;=\; \frac{\frac{\partial^2 H}{\partial X^2}}{\left\{1+\left(\frac{\partial H}{\partial X}\right)^2\right\}^{\frac{3}{2}}Ca}\end{aligned} \quad (4.2.12)$$

where, $Ca=\frac{\mu u_{ref}}{\gamma}$ is the capillary number. The dimensionless kinematic constraint at the free surface is,

$$\frac{Wo^2}{Re}\frac{\partial H}{\partial \Theta}+U\frac{\partial H}{\partial X}=V \quad (4.2.13)$$

In the absence of any time periodic actuation, the viscous relaxation time can be chosen as the dominant time scale as, $\tau_{ref} = h_0^2/\nu$. In such a case, the Womersley number, $Wo = 1$. Accordingly, the velocity reference scale can also be set as the viscous velocity scale as, $u_{ref} = \nu/h_0$. This leads to a Reynolds number, $Re = 1$. One can obtain the equilibrium (base state) velocity profile for the system by assuming a steady, laminar and fully developed flow as (see Chapter 3),

$$U_b(Y) = -\gamma_R \left(1 - \frac{Z_R sinh\left(\frac{Y}{De}\right) + sinh\left(\frac{1-Y}{De}\right)}{sinh\left(\frac{1}{De}\right)} \right) \tag{4.2.14}$$

4.2.3. Linear Stability Analysis

In order to study the stability behavior of the system under an external disturbance, the flow variables are perturbed by infinitesimal disturbances as ,

$$\begin{aligned} U(X,Y,\Theta) &= U_b(Y) + \tilde{U}(X,Y,\Theta) && (4.2.15)\\ V(X,Y,\Theta) &= \tilde{V}(X,Y,\Theta) && (4.2.16)\\ P(X,Y,\Theta) &= P_b(Y) + \tilde{P}(X,Y,\Theta) && (4.2.17)\\ H(X,\Theta) &= 1 + \tilde{H}(X,\Theta) && (4.2.18) \end{aligned}$$

where variables with tilde correspond to perturbation variables. To reduce the number of dependent variables, the stream function is introduced as, $\tilde{U} = \frac{\partial \tilde{\Psi}}{\partial Y}$ and $\tilde{V} = -\frac{\partial \tilde{\Psi}}{\partial X}$. Considering the normal mode solutions of the perturbation variables as,

$$\begin{aligned} \tilde{\Psi}(X,Y,\Theta) &= \bar{\Psi}(Y) e^{i\alpha X + \sigma\Theta} && (4.2.19)\\ \tilde{P}(X,Y,\Theta) &= \bar{P}(Y) e^{i\alpha X + \sigma\Theta} && (4.2.20)\\ \tilde{H}(X,\Theta) &= \bar{H} e^{i\alpha X + \sigma\Theta} && (4.2.21) \end{aligned}$$

where, $\alpha = 2\pi h_0/\lambda_L$ is the dimensionless wave number, λ_L is the wavelength of the perturbation, and σ is the growth rate. Upon substituting the flow variables with the perturbations mentioned above in the Eqs. 4.2.7-4.2.13, linearizing and eliminating pressure the following Orr-Sommerfeld equation is obtained as,

$$\left(\frac{\partial^2}{\partial Y^2} - \alpha^2\right)^2 \bar{\Psi}(Y) - i\alpha U_b \left(\frac{\partial^2}{\partial Y^2} - \alpha^2\right) \bar{\Psi}(Y) + i\alpha \frac{d^2 U_b}{dY^2} \bar{\Psi}(Y) = \sigma \left(\frac{\partial^2}{\partial Y^2} - \alpha^2\right) \bar{\Psi}(Y) \tag{4.2.22}$$

The boundary conditions using the normal mode representation of the perturbation parameters can be written as,

$$\bar{\Psi}(0) = \partial_Y^2 \bar{\Psi}(0) = 0 \tag{4.2.23}$$

$$\left(\frac{\partial^2}{\partial Y^2} + \alpha^2\right)\bar{\Psi}(1) + \bar{H}\frac{d^2 U_b(1)}{dY^2} - i\alpha\gamma_R E_R \bar{H}\left(\left(\frac{\partial \Phi}{\partial X}\right)^2 - \left(\frac{\partial \Phi}{\partial Y}\right)^2\right) = 0 \tag{4.2.24}$$

$$\left(\frac{\partial^2}{\partial Y^2} - 3\alpha^2\right)\bar{\Psi}(1) - \sigma\frac{\partial \bar{\Psi}(1)}{\partial Y} - i\alpha\left[U_b(1)\frac{\partial \bar{\Psi}(1)}{\partial Y} - \bar{\Psi}(1)\frac{dU(1)}{dY}\right] = i\alpha\bar{H}\left(\frac{\alpha^2}{Ca} - A\right) \tag{4.2.25}$$

In thin film stability problems, the long wave analysis of the resulting Orr-Sommerfeld equations yields results that capture the essential features of the full numerical solution of the complex set of equations. Hence the stability information of thin film systems can be recovered without solving the complete set of equations. Here, Yih's method [Yih (1963)] is used to expand the dependent variables like $\bar{\Psi}$ and σ in powers of α and solve equations at zeroth and first orders in α. As a consequence we use the developments,

$$\bar{\Psi} = \bar{\Psi}_0 + \alpha\bar{\Psi}_1 + \alpha^2\bar{\Psi}_2 \ldots \tag{4.2.26}$$

$$\sigma = \sigma_0 + \alpha\sigma_1 + \alpha^2\sigma_2 \ldots \tag{4.2.27}$$

$$\bar{H} = \bar{H}_0 + \alpha\bar{H}_1 + \alpha^2\bar{H}_2 \tag{4.2.28}$$

The characteristic stability curves can be graphically presented by plotting the variation of real part of the growth rate, σ_R vs α in the range of $\alpha \leq O(1)$ i.e. in the long wave limit.

The flow actuating mechanism in this study is the externally applied electric field, which acts as a body force in the fluid bulk and manifests itself as the Maxwell stress on the free surface. Its contribution is reflected in the two dimensionless numbers namely, γ_R and E_R. It has to be noted that, by definition, the mentioned dimensionless numbers also depend upon another imposed field variable - the substrate zeta potential. To study the effect of the imposed electric field and the substrate zeta potential separately, the following combination of γ_R and E_R is presented. By varying the ratio (γ_R/E_R) one can study the effect of the variation of the electric field on the stability of the system. While selectively varying the product ($\gamma_R E_R$) one can study the effect of the variation of the substrate zeta potential on the stability of the system. The other important parameters which have a significant effect on free surface stability are, the dimensionless Hamaker constant (A), the Debye number (De), the capillary number (Ca) and the ratio of the interfacial to substrate zeta

potential (Z_R). The real part of the growth rate, σ_R as obtained from the solution of the Orr-Sommerfeld equations from asymptotic analysis, can be written as,

$$\sigma_R = f(Ca)\alpha^4 + g\left(A, \gamma_R, E_R, Z_R, De\right)\alpha^2 \tag{4.2.29}$$

where,

$$f(Ca) = -\frac{1}{3Ca} \tag{4.2.30}$$

$$\begin{aligned} g\left(A, \gamma_R, E_R, Z_R, De\right) &= A + \frac{\gamma_R}{2E_R} - \left\{cosech\left(\frac{1}{De}\right) - Z_R coth\left(\frac{1}{De}\right)\right\}^2 \gamma_R E_R \\ &- \left\{\left(\frac{1}{De} - 4De\right) cosech\left(\frac{1}{De}\right) - 5coth\left(\frac{1}{De}\right) De\right\} \gamma_R^2 Z_R \\ &+ \left\{\frac{5}{48De^4} - \frac{11}{24De^2} - \frac{1}{2} + \left(\frac{1}{De} - 4De\right) coth\left(\frac{1}{De}\right)\right\} \gamma_R^2 Z_R^2 \\ &- 5cosech\left(\frac{1}{De}\right) De\gamma_R^2 Z_R^2 + 9De^2\gamma_R^2 Z_R^2 - 9De^2\gamma_R^2 Z_R \end{aligned} \tag{4.2.31}$$

4.2.4. Results and Discussion

For fixed values of the parameters for a typical water-air system: $\rho \sim 10^3 kg/m^3$, $\gamma \sim 0.072N/m$, $a \sim 10^{-19} - 10^{-20}J$, $\nu \sim 10^{-6}m^2/s$, $\varepsilon_r \sim 80$, $\varepsilon_0 \sim 8.85 \times 10^{-12}F/m$ is the permittivity of vacuum. The typical values of controllable parameters are taken as, $\zeta_b = 1 - 100mV$, $E_0 = 1 - 100kV/cm$, $c_0 = 0.01mM$ with a film thickness d ranging over $0.1 - 10\mu m$. The flow control parameters are varied to illustrate the parametric dependence of the free surface stability of the system. To highlight the role of the interfacial Maxwell stress on the thin film stability, two characteristic stability curves were worked out. The first one was obtained by removing the Maxwell stress term, $\underline{\underline{\mathbf{\Sigma}}}^{\mathbf{M}}$ from the total stress term, $\underline{\underline{\mathbf{\Sigma}}}^{\mathbf{T}}$ in the free surface boundary conditions. This confines the contribution of the electric field on the hydrodynamics as a body force in the momentum equations. The second characteristic stability curve was obtained by keeping the Maxwell stress term in the total stress at the free surface boundary condition. Upon plotting the real part of the growth rate against the wave number for both cases, it was found that ignoring the Maxwell stress on the free surface over-estimates the instability (see Fig. 4.1). This over prediction can significantly affect the sensitive dependence of the stability of the system which is a function of a large number of the mentioned parameters. The parametric dependence of the stability of the system will be discussed henceforth within the purview of the model that includes the contribution of the Maxwell stress at the free surface. The order of magnitude analysis on Eq. 4.2.8, highlights the relative contribution of the two

important phenomena, namely, disjoining pressure and Maxwell stress to the thin film dynamics. Using Eq. 4.2.8, one can show that the Maxwell stress contribution to the momentum equation represented by $\gamma_R E_R \frac{\partial \Phi}{\partial X} \nabla^2 \Phi$ term reduces to the order $\sim O(\frac{\gamma_R}{De^2})$.

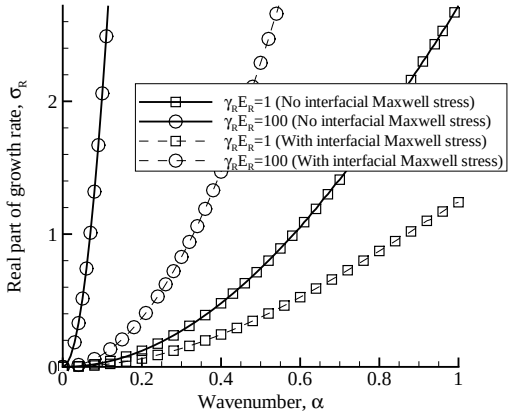

Figure 4.1.: Comparison of the variation of the real part of growth rate (σ_R) as a function of the wave number(α) for $Ca = 1$, $Z_R = 1$, $De = 0.5$, $A = 1$.

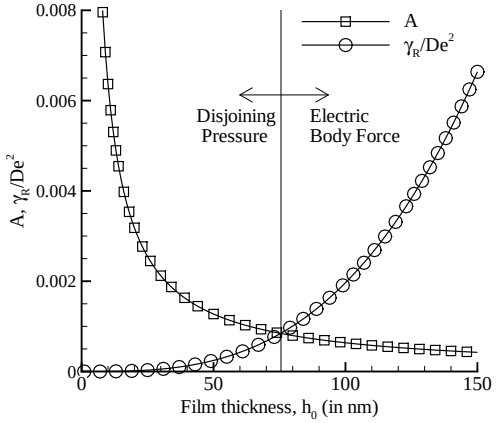

Figure 4.2.: Comparison of the dimensionless contributions of disjoining pressure, A and Maxwell stress as a function of the film thickness h_0 keeping the values of other parameters fixed.

The variation of γ_R/De^2 and A (representing the disjoining pressure) can be plotted as a function of h_0 (see Fig. 4.2). In Fig. 4.2, the two curves A and γ_R/De^2 versus h_0 are giving an intersection point which demarcates two zones showing the relative dominance of the two novel effects, disjoining pressure and Maxwell stress. In the above case the value of the corresponding film thickness is approximately $76nm$. So this means that for the given values of parameters, if film thickness is greater than $76nm$, the effect of disjoining pressure will be less compared to the Maxwell stress.

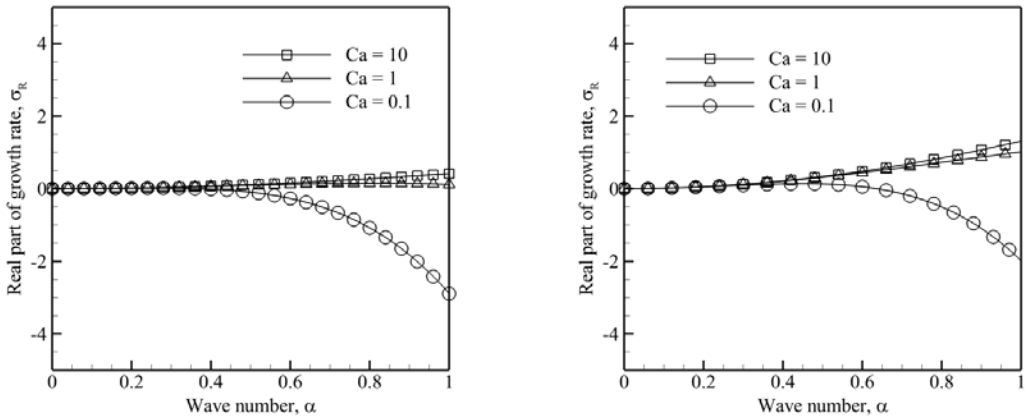

(a) (b)

Figure 4.3.: Growth rate variation with the wave number for different values of the Capillary number, Ca with $\gamma_R E_R = 1$, $De = 0.5$, $Z_R = 0$ and (a) $A = 0.1$, (b) $A = 1$.

Fig. 4.3 shows the growth rate σ_R as a function of the wave number for different values of the capillary number, Ca and two values of the Hamaker's constant A. All the other parameters are taken as fixed. For both values of A, the system becomes more stable at large values of the wave number as the capillary number, Ca increases. This can also be observed from Eqs. 4.2.29 and 4.2.30. While at the small wave numbers, that is in the domain of long wave disturbances, the effect of surface tension diminishes.

It can also be seen that the disjoining pressure represented through the dimensionless constant A, has a significant effect on the stability of the system in the long wave range. Fig. 4.4 shows the effect of A on the growth rate, σ_R for fixed values of electrical field E_{app} (Fig. 4.4a) and substrate zeta potential ζ_b (Fig. 4.4b). From these figures it is observed that upon increasing the disjoining pressure, the system becomes unstable. This phenomenon can be explained by the fact that increasing

the disjoining pressure pushes the system away from the mechanical equilibrium of the thin film hence making the system unstable.

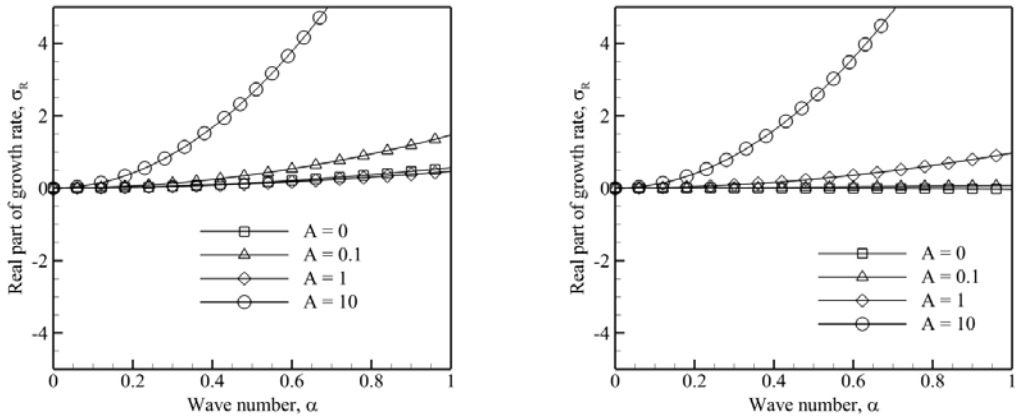

(a) (b)

Figure 4.4.: Growth rate variation with the wave number for different values of dimensionless disjoining pressure, A with $De = 0.1$, $Ca = 10$, $Z_R = 0$ and (a) $\gamma_R/E_R = 2500$, (b) $\gamma_R E_R = 0.01$.

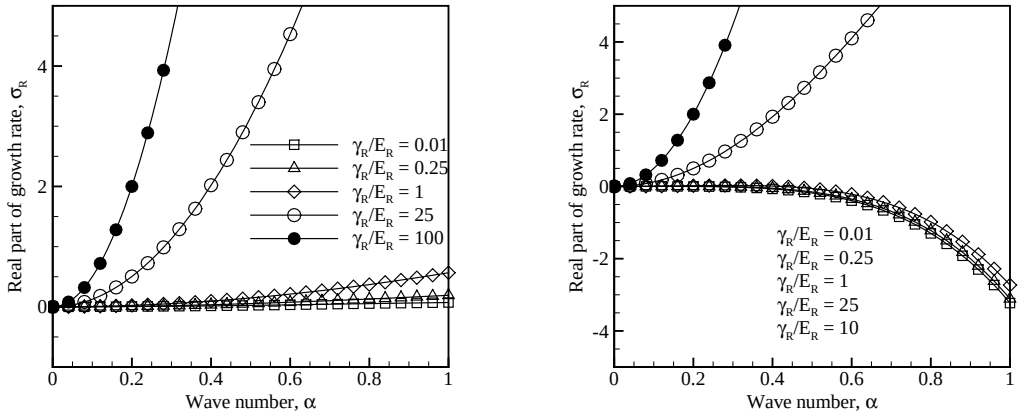

Figure 4.5.: Growth rate variation with the wave number for different values of the applied electric field with $A = 0.1$, $De = 0.1$, $Z_R = 0$ and (a) $Ca = 10$, (b) $Ca = 0.1$.

The effect of the externally applied electric field, which can be reflected through the ratio, γ_R/E_R, on the stability of the system is clearly observed from Eq. 4.2.31 which shows that the increase of the applied electric field makes the system more unstable. This is an expected phenomenon, as upon increasing the magnitude of the electric field, E_0, the unbalanced interfacial stress components due to the resulting Maxwell stress increase, pushing the system away from equilibrium. This effect is shown in Fig. 4.5 for two values of Ca.

It is also known that, influenced by the nature of substrate-fluid interactions and fluid properties, the interfacial zeta potential is determined and can be measured experimentally. Under electro-osmotic flows, the effect of the substrate zeta potential ζ_b has a significant effect on interfacial stability of thin films. This is shown in Fig. 4.6 for two characteristic values of $\gamma_R E_R$, De, Ca and fixed value of A. As can be seen from the expression of the growth factor (Eqs. 4.2.29-4.2.31), the product $\gamma_R E_R$, which is proportional to ζ_b^2 has a negative coefficient, and leads to a decrease in the growth factor when the substrate zeta potential is increased. Hence, when the substrate zeta potential is increased, the system becomes more stable which is clearly shown in Fig. 4.6a for $Z_R = -1$. However, when the interfacial polarity is same as the substrate, an opposite behaviour is seen (Fig. 4.6b), which is explained below.

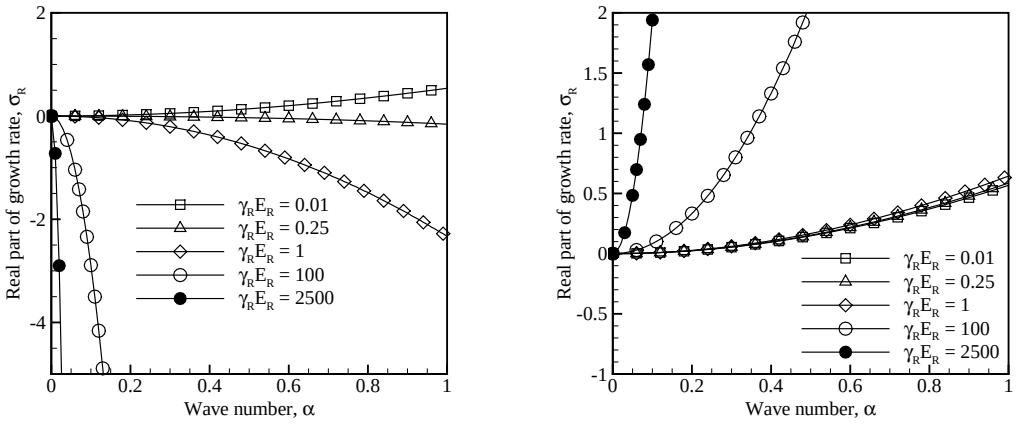

Figure 4.6.: Growth rate variation with the wave number for different values of substrate zeta potential with $De = 0.5$, $Ca = 10$, $A = 0.1$ and (a)$Z_R = -1$, (b)$Z_R = 1$.

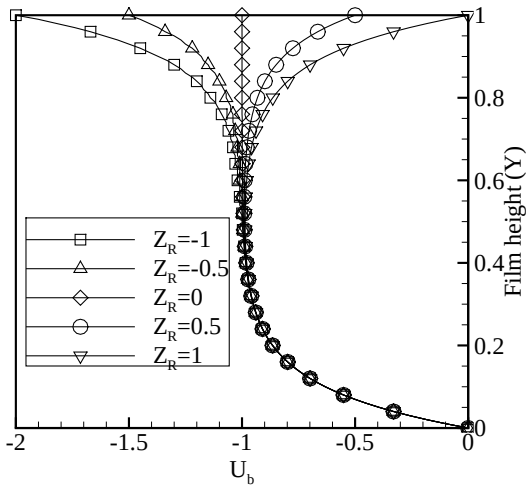

Figure 4.7.: The base state velocity profile with different values of the surface to substrate potential ratio (Z_R). The values of other fixed parameters are: $\gamma_R = 1$, $De = 0.1$.

From the basic state velocity distribution (see Eq. 4.2.14), one can see that depend-

ing upon the interfacial zeta potential the interface can either reduce the interfacial stress or enhance it. This is also shown in Fig. 4.7 where one can also see that when the interface has an opposite polarity as compared to the substrate, it reduces the interfacial stress and when the free surface polarity is the same as the substrate, it supports the interfacial stress. This relation between interfacial polarity and interfacial stress also manifests itself in the system stability equations (Eqs. 4.2.29-4.2.31) as expected. It is observed that the interfacial polarity with respect to the substrate zeta potential, which is represented by the ratio Z_R, tends to increase the system stability as it reduces the interfacial stress when Z_R is negative i.e. of the opposite polarity as the substrate. The system becomes more unstable when Z_R is positive, i.e. of the same polarity as of the substrate as it enhances the interfacial stress. This effect is shown in Fig. 4.8. This can also be attributed to the impact of substrate zeta potential on the distribution of charged species in the bulk of the fluid. As the zeta potential of the interface increases, the concentration of counter ion species increases near the substrate, decreasing the ionic concentration in the bulk which screens the magnitude of the net electric potential as felt at the interface. This decreases the contributions of the charged substrate to the interfacial Maxwell stress hence making the system more stable. This mechanism is also clearly highlighted in Fig. 4.6 which shows the growth rate variation for two opposite values of Z_R with $\gamma_R E_R$ as the varying parameter and all the other parameters being fixed.

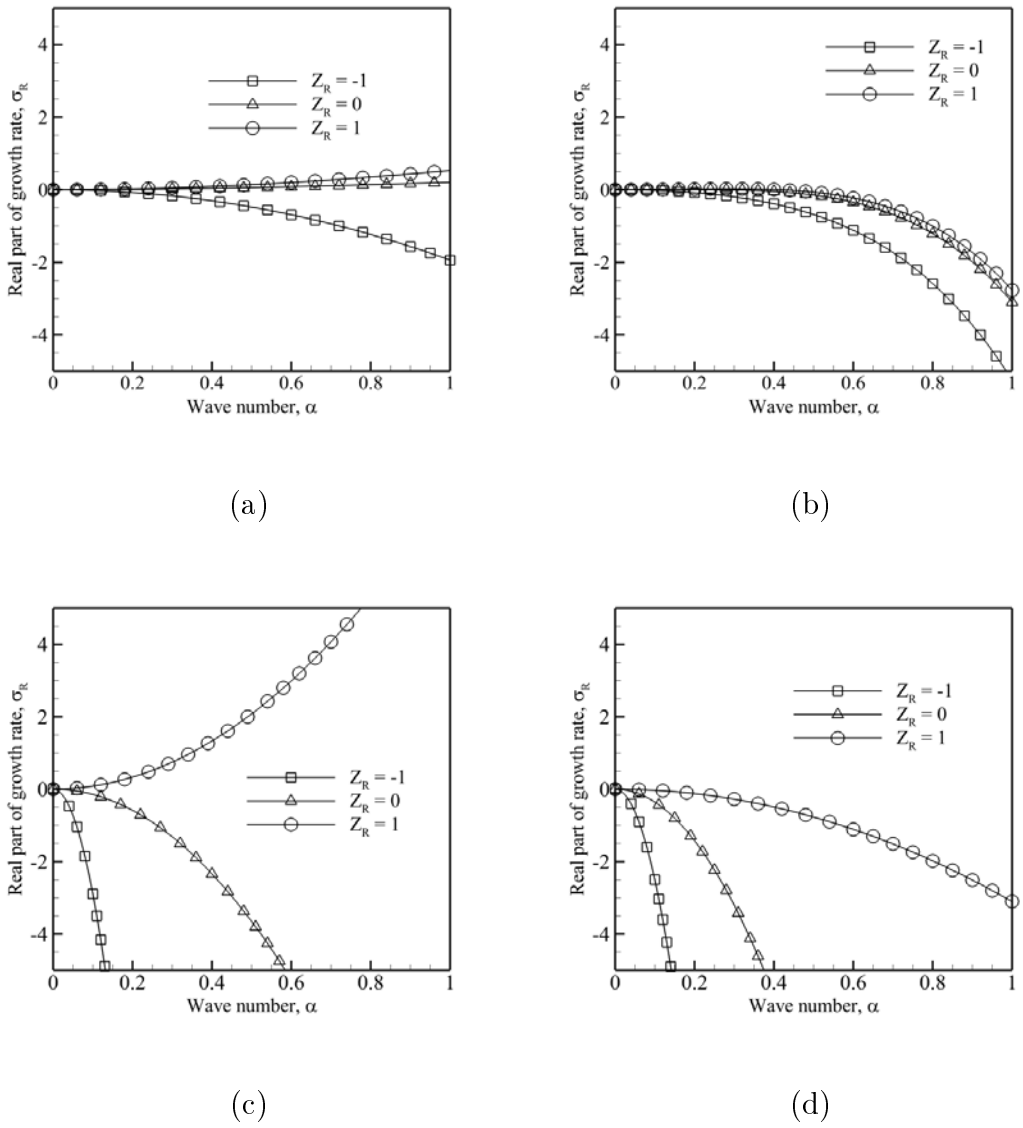

Figure 4.8.: Growth rate variation with the wave number for different values of interfacial zeta potential. With fixed parameters as, $\gamma_R E_R = 1$, $De = 1$, $A = 0.1$, for different values of Capillary number as, (a) $Ca = 10$, (b) $Ca = 0.1$, and also with $\gamma_R / E_R = 100$, $Ca = 10$, $A = 0.1$, for different values of Debye number as, (c) $De = 0.5$, (d) $De = 1$.

The effect of initial film thickness as compared to the Debye length, represented by the Debye number, De, on the interfacial stability is not obvious by observing the growth factor characteristic equation (Eqs. 4.2.29-4.2.31). Fig. 4.9 shows the effect of De on the stability of the system for different values of all the other parameters.

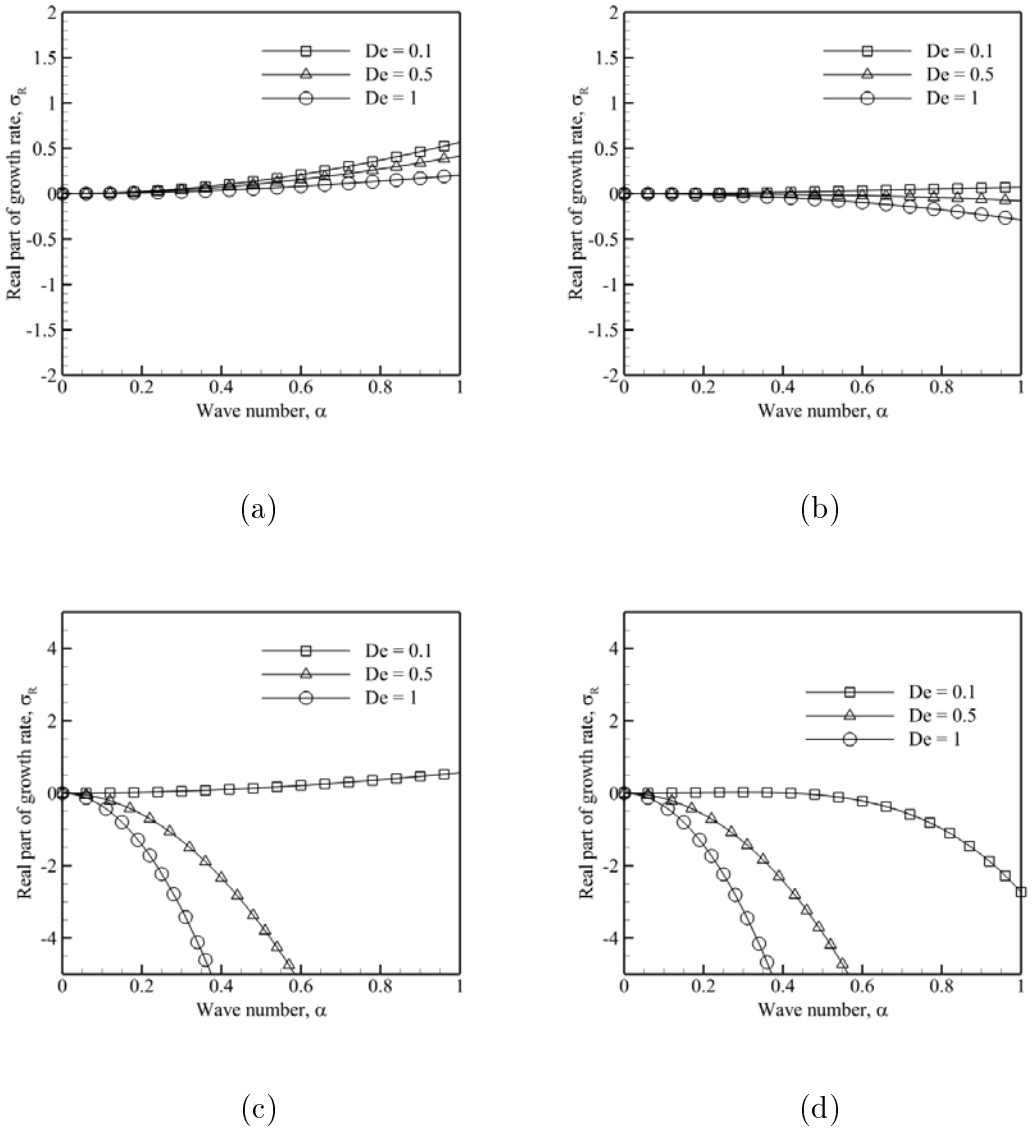

Figure 4.9.: Growth rate variation with the wave number for different values of the Debye number, which corresponds to a varying Debye length for a given film thickness. With fixed parameters as, $Z_R = 0$, $Ca = 10$, $A = 0.1$ for different values of wall zeta potential as, (a) $\gamma_R E_R = 1$, (b) $\gamma_R E_R = 0.01$, and also with $\gamma_R / E_R = 100$, $Z_R = 0$, $A = 0.1$ for different values of Capillary number as, (c) $Ca = 10$, (d) $Ca = 0.1$.

It is observed from this figure that the stability of the system increases upon increasing De. This can be explained by the fact that for a given film thickness h_0, an increase in Debye number corresponds to an increasing Debye length, which in turn corresponds to a decrease in ionic concentration as, $\lambda_D \propto \frac{1}{\sqrt{c_0}}$, where c_0 is the

ionic concentration. Hence, a decrease in the ionic concentration drives the system naturally towards stability. The flow actuating mechanism in this problem is the Coulombic force by the external electric field on to the distribution of ions in the fluid. If the ionic concentration c_0 is low, so will be the net forces by the external electric field on the ionic solution. Hence, in this limit of large De, the flow will be reduced and consequently the interface will stay undisturbed.

Conditions leading to the onset of instability can be complemented by a study of a mode that corresponds to the maximum growth rate of a disturbance. This mode, which is characterized as the most dangerous mode ($\alpha_{critical}$), is studied as a function of the set of parameters mentioned above. The most dangerous mode is the wave number for which the characteristic stability curve (Eq. 4.2.29) of a system reaches a maximum. The resulting wave number is obtained as a function of dimensionless parameters through the following equation:

$$\alpha_{critical} = \sqrt{\frac{-g\left(A, \gamma_R, E_R, Z_R, De\right)}{2f(Ca)}} \tag{4.2.32}$$

with a condition that $g\left(A, \gamma_R, E_R, Z_R, De\right)$ is positive.

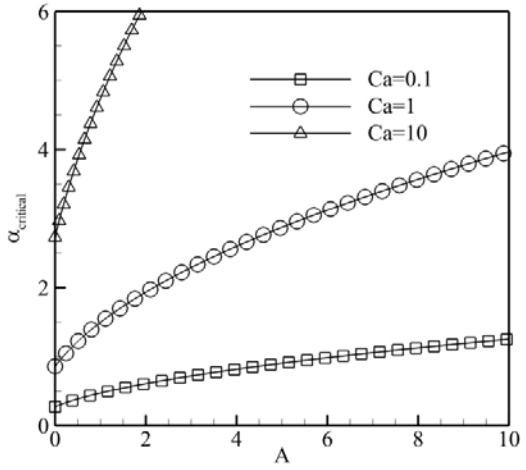

Figure 4.10.: Most dangerous wave number ($\alpha_{critical}$) variation with the van der Waals parameter (A), for different values of the capillary number (Ca). Values of other fixed parameters are, $\gamma_R E_R = 1$, $De = 1$, $Z_R = 0$.

The values of $\alpha_{critical}$ as obtained from the above equation, was studied for the various dimensionless parameters and representative results are presented in Fig. 4.10-Fig. 4.12. The increase in van der Waals parameter (A) increases the value of $\alpha_{critical}$ (see Fig. 4.10).

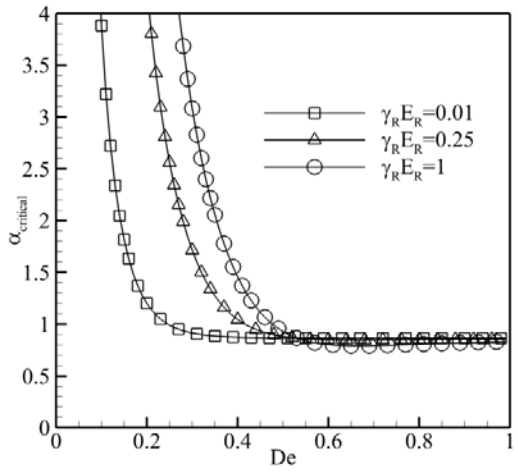

Figure 4.11.: Most dangerous wave number ($\alpha_{critical}$) variation with the Debye number (De) for different values of the wall zeta potential ($\gamma_R E_R$). Values of other fixed parameters are, $Ca = 1$, $Z_R = 1$, $A = 0$.

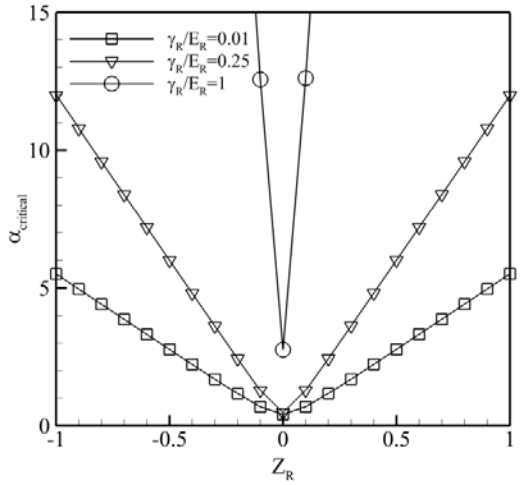

Figure 4.12.: Most dangerous wave number ($\alpha_{critical}$) variation with the zeta potential ratio (Z_R) for different values of the electric field parameter (γ_R/E_R). Values of other fixed parameters are, $Ca = 1/10$, $De = 0.1$, $A = 1$.

It is also observed that the increase in the value of surface tension decreases the value of $\alpha_{critical}$, which is consistent with the observation that the increase in surface tension increases the stability of the system by decreasing the most dangerous mode. It is observed that the most dangerous mode is independent of the Debye number for $\lambda_D > h_0/2$ (see Fig. 4.11) and suggests that the most dangerous wavelength is of the order of the film thickness in this range of De, independently of the other parameters. For a given value of the Debye number, $\alpha_{critical}$ increases with the wall zeta potential ($\gamma_R E_R$) (see Fig. 4.11). Finally, the most dangerous mode is independent of the polarity of the interface zeta potential (Z_R) and increases with its magnitude (see Fig. 4.12). Also, the increase in the magnitude of the external electric field (γ_R/E_R) increases the value of the most dangerous mode.

4.3. Thin film stability under AC EOF

The system under study consists of a thin electrolyte film spread over a rigid solid substrate exposed to an inert gaseous atmosphere (see Fig. 3.1). The film thickness is denoted by h_0. The dynamics of such a film is studied under the effect of a longitudinal oscillating electric field, $\mathbf{E_{app}} = E_0 sin(\omega t)\,\mathbf{i}$, where E_0 is the magnitude and ω is the frequency of the applied electric field. The total electric potential in the conductive thin film system can be written as (see Eq. 3.3.2),

$$\begin{aligned}\Phi(X,Y,\Theta) &= \Phi_{app}(X,\Theta) + \Phi_{sc}(Y) \\ &= -\frac{X}{E_R} sin\Theta + \frac{1}{sinh\left(\frac{H}{De}\right)}\left\{Z_R sinh\left(\frac{Y}{De}\right) + sinh\left(\frac{H-Y}{De}\right)\right\}\end{aligned} \tag{4.3.1}$$

where, $\Theta = \omega t$ is the dimensionless time.

4.3.1. Hydrodynamic Equations

For the dimensionless conservation equations one can refer to the Eqs. 4.2.7-4.2.13.

4.3.2. Linear Stability Analysis

The perturbations in the flow variables are introduced as, $U = U_b + \tilde{U}$, $V = \tilde{V}$, $P = P_b + \tilde{P}$ and $H = 1 + \tilde{H}$. The velocity components are converted into stream function using $\tilde{U} = \partial\tilde{\Psi}/\partial Y$ and $\tilde{V} = -\partial\tilde{\Psi}/\partial X$. The normal mode solutions to the perturbations are considered with small amplitude and with long wavelength ($\lambda_L \gg h_0$) as,

$$\tilde{\Psi}(X,Y,\Theta) = \bar{\Psi}(Y,\Theta)e^{i\alpha X} \tag{4.3.2}$$

$$\tilde{P}(X,Y,\Theta) = \bar{P}(Y,\Theta)e^{i\alpha X} \tag{4.3.3}$$

$$\tilde{H}(X,\Theta) = \bar{H}(\Theta)\,e^{i\alpha X} \tag{4.3.4}$$

where,$\alpha = 2\pi h_0/\lambda_L$ is the dimensionless wave number and λ_L is the wavelength of the perturbation. Upon substituting the flow variables with the perturbations mentioned above in the Eqs. 4.2.7-4.2.13, linearizing and eliminating pressure the following Orr-Sommerfeld equation is obtained as,

$$\left(\frac{\partial^2}{\partial Y^2} - \alpha^2\right)^2 \bar{\Psi}(Y,\Theta) - \left(Wo^2\frac{\partial}{\partial\Theta} + i\alpha ReU_b\right)\left(\frac{\partial^2}{\partial Y^2} - \alpha^2\right)\bar{\Psi}(Y,\Theta) + i\alpha Re\frac{\partial^2 U_b}{\partial Y^2}\bar{\Psi}(Y,\Theta) = 0 \tag{4.3.5}$$

The boundary conditions using the normal mode representation of the perturbation parameters can be written as,

$$\begin{aligned}
\bar{\Psi}(0,\Theta) = \frac{\partial^2\bar{\Psi}(0,\Theta)}{\partial Y^2} &= 0\\
\left(\frac{\partial^2}{\partial Y^2} + \alpha^2\right)\bar{\Psi}(1,\Theta) + \bar{H}(\Theta)\frac{\partial^2 U_b(1,\Theta)}{\partial Y^2} &\\
-i\alpha\gamma_R E_R\bar{H}(\Theta)\left(\left(\frac{\partial\Phi}{\partial X}\right)^2 - \left(\frac{\partial\Phi}{\partial Y}\right)^2\right) &= 0\\
\left(\frac{\partial^2}{\partial Y^2} - 3\alpha^2\right)\bar{\Psi}(1,\Theta) - Wo^2\frac{\partial^2\bar{\Psi}(1,\Theta)}{\partial\Theta\partial Y} &\\
-i\alpha Re\left[U_b(1,\Theta)\frac{\partial\bar{\Psi}(1,\Theta)}{\partial Y} - \bar{\Psi}(1,\Theta)\frac{\partial U_b(1,\Theta)}{\partial Y}\right] &= i\alpha\bar{H}(\Theta)\left(\frac{\alpha^2}{Ca} - A\right)
\end{aligned} \tag{4.3.6}$$

Using Floquet theory for the above eigen value problem, the solution for the perturbation variables can be expressed as, $\bar{\Psi}(Y,\Theta) = \hat{\Psi}(Y,\Theta)\mathrm{e}^{\sigma\Theta}$ and $\bar{H}(\Theta) = \hat{H}(\Theta)e^{\sigma\Theta}$ where, σ is the Floquet exponent, and $\hat{\Psi}(Y,\Theta)$ and $\hat{H}(\Theta)$ are time periodic functions. Upon using asymptotic expansions in small parameter ($\alpha \ll 1$) and expanding the parameters as,

$$\hat{\Psi} = \hat{\Psi}_0 + \alpha\hat{\Psi}_1 + \alpha^2\hat{\Psi}_2\ldots \tag{4.3.7}$$

$$\hat{H} = \hat{H}_0 + \alpha\hat{H}_1 + \alpha^2\hat{H}_2\ldots \tag{4.3.8}$$

$$\sigma = \sigma_0 + \alpha\sigma_1 + \alpha^2\sigma_2\ldots \tag{4.3.9}$$

Upon solving the resulting set of equations at different orders of α (see Appendix B), the characteristic equation of the system was obtained as,

$$\sigma = f(\alpha, \gamma_R, Z_R, E_R, Wo, Re, Ca, De) \tag{4.3.10}$$

4.3.3. Results and discussions

System Parameters

To estimate the typical values of the dimensionless parameters, an aqueous solution is considered as the working fluid where the transport coefficients are taken to be of water at the normal temperature and pressure, viz. $\rho \sim 10^3 kg/m^3$, $\mu \sim 10^{-3} Pa \cdot s$, $\varepsilon_r \sim 80$, $\varepsilon_0 \sim 8.85 \times 10^{-12}$ is the permittivity of vacuum, $\gamma \sim 0.072 N/m$ is the surface tension between water and air, $a \sim 10^{-20} J$ is the Hamaker constant, the substrate zeta potential is taken as $\zeta_b \sim 10mV$, the applied electric field, $E_{app} \sim 1kV/cm$ with a frequency, ω of 1MHz. The characteristic electro-osmotic velocity, u_{HS} can be therefore estimated as $1mm/s$. For a film thickness, $h_0 \sim 100nm$, the dimensionless Hamaker constant, A is ~ 0.1, the electro-viscous ratio, $\gamma_R \sim 1$, the ratio $E_R \sim 1$, Capillary number, $Ca \sim 10^{-5}$, Reynolds number, $Re \sim 10^{-4}$. The flow control parameters are varied over a range to illustrate the parametric dependence of the free surface stability of the system.

The ionic concentration in the system is considered to be low ($c_0 \sim 0.1mM$) which gives a Debye length (λ_D) of the order of $30nm$. Such a small ionic concentration reduces the non-linear dynamics of ions. The resulting Debye number De varies from $0.01 - 0.1$.

Instability Mechanism

1. Contribution of Capillary and Disjoining Pressure

The stability of a thin film under electro-osmotic flow can be attributed to the competing dynamics between the capillary forces through Laplace pressure, van der Waals forces through disjoining pressure and electrostatic forces through the electro-osmotic pressure. From the right hand side of the Eq. 4.3.6 we can see that the terms representative of respectively, Laplace pressure ($1/Ca$) and disjoining pressure (A) appear together at the free surface boundary condition in a counterbalancing manner, showing the existence of conflicting forces.

When the film surface is perturbed by a small amplitude disturbance, the induced curvature forces the local Laplace pressure to become greater (or smaller) than the forces in the bulk, creating an outflow (or inflow) of liquid restoring the equilibrium configuration of the film. However, the long range nature of the disjoining pressure has a permanent effect on the film dynamics. A negative disjoining pressure ($\Pi < 0$) between the interfaces leads to attraction between them forcing a film breakup while a positive disjoining pressure ($\Pi > 0$) leads to repulsion between the interfaces, causing a film build-up (see Fig. 4.13). Moreover, upon application of an oscillating electric field, the stability characteristics of the film can be modified as compared to the static case (see Fig. 4.13b, c).

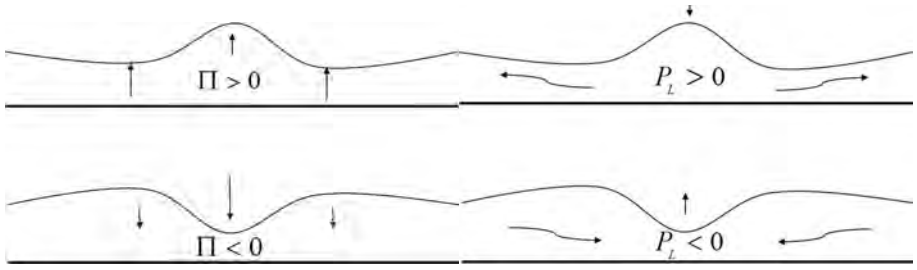

(a)

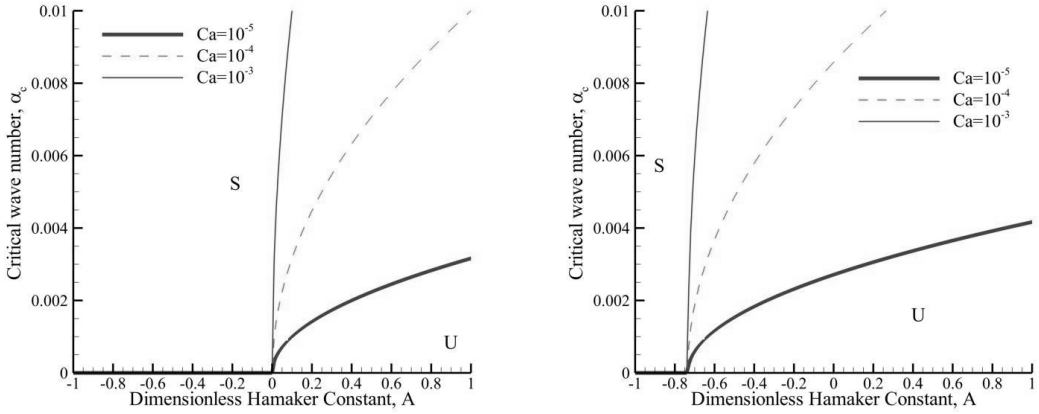

(b) (c)

Figure 4.13.: (a) Interfacial displacement under the influence of disjoining pressure (Π) and Laplace pressure (P_L) under a positive (crest) and negative (trough) perturbation in the interface. Upon fixing the value of the parameters as $De = 0.1$, $Z_R = 0.01$, $Re = 10^{-4}$, $\gamma_R = 1$, $Wo = 1$, Marginal stability curves showing the critical wave number as a function of the dimensionless Hamaker constant, A in the (b) absence of time-periodic electric field, and (c) presence of time-periodic electric field.

2. Contribution of EDL

Within an EDL, two important interactions between the ions can be identified, firstly, the repulsive Coulombic interaction between the counter-ions, and secondly, the configurational entropy of the counter-ion distribution, which resists the configurational change due to the Coulombic repulsion [Israelachvili (2011)]. Such a competition between the two phenomena manifests itself in terms of a pressure, which can be termed as the EDL pressure. The EDL pressure distribution in a thin film can be obtained from the basic state solution of the system (see 3.2.13 and 3.3.14).

In order to identify that out of the two phenomena, entropic and Coulombic, which one has a dominating contribution towards a film stability, the following discussion is presented. The diffused cloud of counter-ions in an EDL is maintained in an equilibrium through mutual repulsions which forces them away from the oppositely charged substrate (or interface) and hence leads to a configurational entropy.

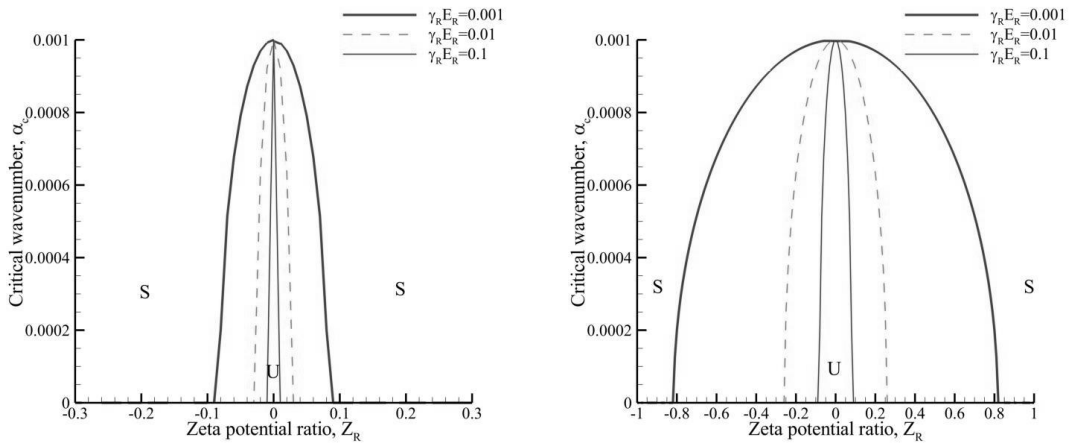

Figure 4.14.: Marginal stability curves showing the critical wave number as a function of the zeta potential ratio (Z_R) with stability trends for different values of substrate zeta potential ($\gamma_R E_R$) in the absence of external electric field at (a) $De = 0.01$ (b) $De = 0.1$ with $Ca = 10^{-5}$ and $A = 0.1$.

When two such ordered charged clouds (EDLs) are brought closer through a perturbation (e.g. EDL near a free surface is brought closer to an EDL near a solid surface), a repulsive force initiates between the two charged clouds, restoring the equilibrium and stabilizing the film. From Fig. 4.14, one can observe that a charged free surface ($Z_R \neq 0$) over a charged substrate ($\gamma_R E_R \neq 0$), is relatively more stable than an uncharged free surface ($Z_R = 0$). The case of a charged free surface over a charged substrate creates two interfaces with diffused charge distribution following the stability dynamics mentioned above. Moreover, the symmetry observed in the marginal stability curves (see Fig. 4.14) about $Z_R = 0$ justifies the entropic rather than Coulombic dominance on the EDL pressure, where the polarity of the free surface charge cloud does not affect the stability of the film.

One of the other important parameters associated with the EDL is the extent of the diffused charge penetration in the bulk. This extent of the diffused charge is characterized by the Debye length (λ_D). The relative extent of the EDL thickness as

compared to the film thickness is represented in this work through the Debye number, De. For thin EDLs (small De) one can imagine a closer packing of diffused ions leading to a higher configurational entropy and hence greater repulsion between the interfaces, leading to a more stable film. This idea is also observed in the Fig. 4.14 where thinner EDL ($De = 0.01$) (Fig. 4.14a) is more stable than a thicker EDL ($De = 0.1$) (Fig. 4.14b).

3. Contribution of the oscillating Electric field

An oscillating electric field acting on a charged interface introduces a time-dependent dispersive field near the interfaces (see Fig. 4.15a). It can be seen that maximum magnitude of the vorticity ($|\omega_{\mathbf{b}}| = |\nabla \times \mathbf{U_b}| = |\partial U_b/\partial Y|$) occurs at both the interfaces (solid-liquid and gas-liquid). It can be understood the deformation of the free surface is dependent upon the strength of this vortex which is a function of various parameters like De, which accounts for the diffusive extent of the electrical effects in the bulk, the strength of the applied electric field (γ_R/E_R) and the strength of interfacial polarity ($\gamma_R E_R$ and Z_R). However, it is also known that any deformation in such an interface is countered by a dissipating viscous stress. The strength of this viscous damping mainly depends upon parameters like the coefficient of viscosity and Wo, which accounts for the diffusive extent of the viscous effects in the bulk. The two competing mechanisms mentioned above contribute to the neutral stability characteristics of the system. Upon changing the Reynolds number by keeping all the other parameters fixed, which is equivalent to changing the dynamic viscosity, one observes from the marginal stability curves (α_c, Wo) that more viscous fluids (smaller Re) are more stable as compared to less viscous fluids (larger Re) (see Fig. 4.15c). Thin EDLs (smaller De) owing to their smaller spatial extent of charge have high velocity gradients as compared to thicker EDLs (larger De). This is also observed in Fig. 4.15a. Hence, for thin EDLs (smaller De) the film is expected to be more unstable as compared to films with thicker EDLs (see Fig. 4.15b). The electro-osmotic velocity distribution in the film is directly proportional to the strength of the applied electric field. Hence, upon increasing the strength of the applied electric field, the strength of the free surface vortex is enhanced thus leading to a more unstable system (see Fig. 4.15d).

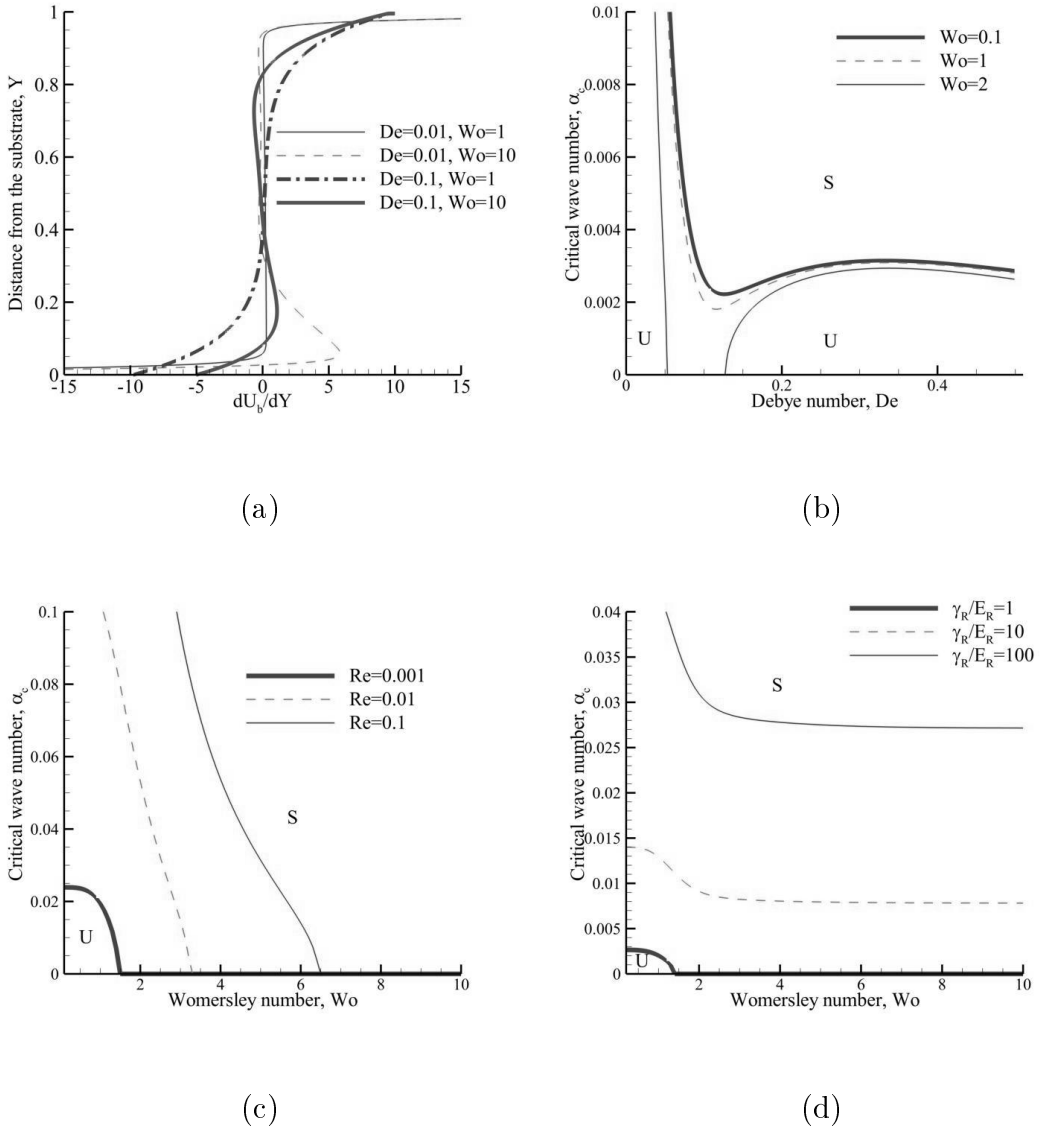

Figure 4.15.: (a) Base state vorticity ($|\omega_\mathbf{b}| = |\nabla \times \mathbf{U_b}|$) distribution over the film thickness at $\gamma_R = 1$, $Z_R = 1$ (b) Marginal stability curves showing the critical wave number as a function of the Debye number (De) with stability trends for different values of Womersley number (Wo). Marginal stability curves showing the critical wave number as a function of the Wo with stability trends for different values of (c) Reynolds number (d) Electric field strength (γ_R/E_R).

4.4. Conclusion

In this chapter, a detailed analysis of the stability of a free surface of an ultra thin liquid film under steady and time-dependent electro-osmotic flow conditions was presented. Through long wave asymptotic analysis of the Orr-Sommerfeld equations, parametric stability thresholds of a thin aqueous film has been explored with a focus on parameters like surface tension, Hamaker's constant for fluid-substrate interaction, magnitude of the externally applied electric field, substrate and free surface zeta potential. It was observed that ignoring the free surface Maxwell stress under electro-osmotic flow, over-estimates the free surface instability. The presented characteristic stability curve helps to identify the critical values of various parameters presented in this chapter, which can be effective in designing thin film flow process in microfluidic devices. Some of the parameter dependent stability trends are summarized as,

(a) The phenomena which are observed to have a stabilizing effect on the film dynamics are surface tension, repulsive disjoining pressure ($A < 0$), osmotic pressure due to the EDL at the interfaces and viscous dissipation.

(b) The phenomena contributing towards the instability of the film are attractive disjoining pressure ($A > 0$), thin EDLs ($De \ll 1$), external electric field driving the electro-osmotic flow and low frequencies. The film stability decreases upon increasing the magnitude of the applied electric field, which is due to an increase in the tangential Maxwell stresses at the interface.

(c) The increase in the value of substrate zeta potential tends to stabilize the flow which in turn enhances the osmotic pressure component.

However, due to a complex interaction of all the above phenomena together, the individual stability thresholds overlap, generating interesting stability trends which are tunable over a wide range of the above mentioned parameters. Such a generalized analysis helps identifying parametric boundaries for sustaining thin films over a wide range of fluid properties and operating conditions.

Part III.

Experimental Studies

5. Microfabrication and Experimental Setup

5.1. Overview

In order to observe and parametrize the interfacial instability between two miscible and immiscible fluids, an experimental setup was established to create a microfluidic two fluid interface, with a possibility of imposing controlled flow rate and electro-osmotic flow. To that end, various microfluidic chips were fabricated, which were interfaced with syringe pumps for pumping liquids and electric potential generator to actuate the electro-osmotic flow. Another objective of the electro-osmotic experimental setup was to correlate the substrate zeta potential to the electro-osmotic velocity, which by virtue of its non-dispersive nature is easy to measure by velocimetry techniques. Although, this is one of the classical approaches to quantify the substrate zeta potential, it was used as a validation case towards assuring a working electro-osmotic flow setup.

In this chapter an overview of microfluidic device fabrication and the details of the experimental apparatus used to create a two fluid electro-osmotic flow is provided. Experimental microfluidics has been a widely explored field which basically starts with fabrication of the microdevices, setting up of the sample injection and control, image acquisition setup and analysis of the results. Although, each of the mentioned steps requires a high degree of precision and control, for each of them, a wide range of choices are available depending upon one's research objective and the resources. One can either mount a very basic microfluidic setup to perform exploratory research or build up an extremely controlled and isolated microfluidic environment for critical applications such as in the bio-medical field.

The first step towards fabrication of a microfluidic device is the choice of the material which embeds the motif of the channel. Grossly, one can categorize the existing materials into soft materials such as Elastomers (e.g. PolyDiMethylSiloxane (PDMS), PolyMethylMethAcrylate (PMMA), NOrland Adhesive 81 (NOA), etc.), Thermoplastics [Tsao and DeVoe (2008)], paper [Li et al. (2012)] and hard materials like glass, silicon, etc. As each of the mentioned materials have different physico-chemical properties, the methodology of microfabrication also varies accordingly. Among the mentioned microfabrication materials, one of the most commonly used materials is PDMS, an elastomer which is well-known for its rapid prototyping, low cost and

good optical properties. All the mentioned characteristics of PDMS elastomer make it a good candidate for exploratory research. In this work, the microfabrication was carried out on using PDMS elastomer and hence the methodologies specific to PDMS elastomer will be discussed. Further, the details leading to sample injection in the microchannel are provided where the sample consists of a set of miscible fluids namely, aqueous electrolyte and de-ionized water and a set of immiscible fluids namely, an aqueous electrolytic solution and an oil. Finally, the details of the image acquisition system is provided which included a basic micro-PIV measurement and a phase-contrast observation of the interface between two fluids.

5.2. Microfabrication

In order to build microchannels using a PDMS elastomer by the help of soft lithography [Xia and Whitesides (1998)], one has to strictly follow a well defined protocol in order to enhance the reproducibility. During the experimental studies, a number of microchip designs were fabricated with variable shapes and sizes and experiments were performed. Although the basic fabrication process of all the microchips remained the same, the fabrication process of a representative chip is discussed further. The representative chip is a cross shaped channel with reservoirs at its ends for inserting the liquids and the electrodes. This kind of chip facilitates the creation of two-fluid interface which is exposed to an AC electric field by the electrodes (see Fig. 5.1).

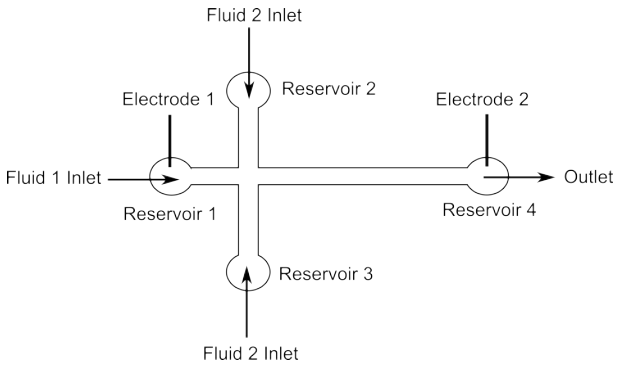

Figure 5.1.: A representative microchannel design.

The various steps followed in this work leading to a microchip fabrication can be enumerated as below and shown in the Fig. 5.2.

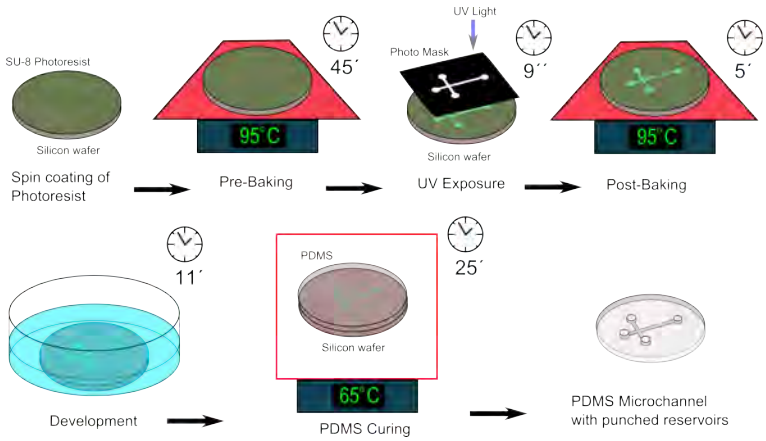

Figure 5.2.: Basic steps used for Microfabrication.

- **Microchannel Design and Photo-Mask:** The first step towards creating a microchannel is by designing the required channel motif using a computer-aided-design (CAD) software. The software used to design microchannel motifs in this study is *CleWin* v3.2. This design is used to create a photo-mask (just like a negative in photography). The microchannel design is imprinted on this photo-mask, where the channel design is transparent (which allows the passage of light) and the surrounding area is dark (which blocks the passage of light) (see Fig. 5.3).

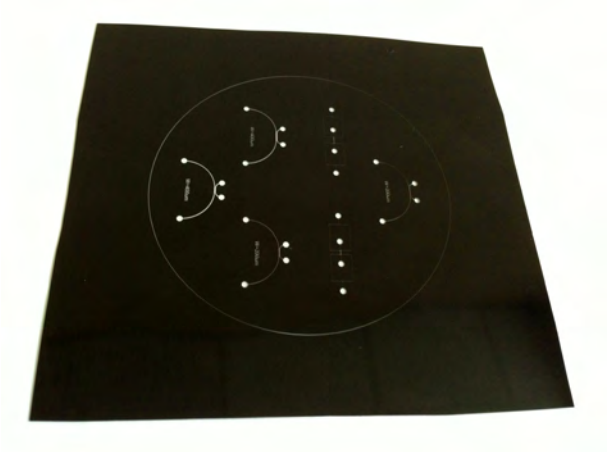

Figure 5.3.: A sample photo mask with microchannel motifs

- **Mold Substrate Preparation:** The next step involves the preparation of the mold substrate. The substrate used in this study is a Silicon wafer, 3″ in

diameter. The Silicon wafer is washed with Acetone and Iso-Propanol respectively and then dried under a jet of Nitrogen gas. The dried wafer is exposed under plasma for 1 minute. Exposing the Silicon wafer to plasma activates the surface and enhances the binding of a photo-sensitive material on its surface.

- **Spin-coating of the photo-resist**: A photo-resist is a light sensitive material which is used to create patterned structures in soft-lithography. There are two kinds of photo-resists - positive and negative. When a positive photo-resist is exposed to powerful Ultra-Violet (UV) rays, it becomes soluble in a solvent (also called the developer solvent) while when a negative photo-resist is exposed to UV rays, it polymerizes and becomes insoluble in the developer solvent. This characteristic feature of a photo-resist can be used to create controlled patterns in a microchannel design. A negative photo-resist is spin-coated on the activated wafer as mentioned in second step as the channel motif in the photo-mask in first step is transparent and hence allows the passage of the UV light through it. The spin-coating protocol depends upon the thickness of the photo-resist one wants on the wafer, which is eventually determined by the requirements of the channel height. In this work, the channels were fabricated with a height of $100\mu m$ in order to keep the channel aspect ratio $1:1$ and $1:2$. So to obtain a height of $100\mu m$, SU8-3050 photo-resist was spin-coated on the Silicon wafer in two steps. During the first step, the wafer was spin-coated at $500rpm$ for $10s$ at the angular acceleration of $100rpm/s$ and then at $1000rpm$ for $30s$ at the angular acceleration of $300rpm/s$.
- **Pre-Exposure Bake/Soft Bake:** Now, this spin-coated wafer is baked on a hot-plate at the temperature of $95°C$ for $45mins$. This pre-baking step densifies the photo-resist by evaporating the coating solvent.
- **Mask Alignment and UV Exposure:** After pre-baking, the spin-coated wafer is exposed under uniform UV illumination using an aligner masked by the photo-negative which contains the microchannel design. Since the photo-resist SU8-3050 is a negative photo-resist, which means that the photo-resist is photopolymerized where it is exposed to the UV radiation and hence is rendered insoluble in the photo-resist developer solution. In this work, SUSS MicroTec aligner was used for the UV exposure, where the power of the UV lamp was $36mW/cm^2$ Next, spin-coated and baked wafer is covered by the photo mask containing the channel design through the holding mechanism in the aligner and exposed to the UV light for $9s$.
- **Post-Exposure Bake/Hard Bake:** Next, the UV exposed wafer is placed on the hotplate at a temperature of $95°C$ for $5mins$.
- **Development:** In this process, the exposed (and hence polymerized) photo-resist on the wafer is put in a solvent (developer) which dissolves the non-polymerized part of the photo-resist leaving behind the polymerized photo-resist in the shape of the microchannel motif as printed on the photo-mask. The developer solution used here is Propylene Glycol Mono-methyl Ether Ac-

etate (PGMEA) which specifically dissolves the non-polymerized SU8 and leaves behind the photopolymerized SU8 on the wafer. The exposed and baked wafer is soaked in a bath of PGMEA for 11 minutes. Further, the wafer is rinsed by Iso-Propanol and blow dried by a jet of Nitrogen gas. If some white traces remain on the wafer, it is soaked again in the bath of the PGMEA and the process is repeated until a clean wafer with the embossed microchannel design is obtained. This henceforth will be referred as the "master mold".

- **Preparation of the PDMS elastomer:** For preparing the microchip, around $30 grams\,(g)$ of SYLGARD 184 PDMS elastomer was mixed with $3g$ curing agent ($10:1$ w/w ratio and referred to as PDMS-1 later) and degassed using a vacuum chamber until no bubbles were visible anymore. Similarly, around $20g$ of SYLGARD 184 PDMS elastomer was mixed with $4g$ of curing agent ($5:1$ w/w ratio and referred to as PDMS-2 later) and degassed. The PDMS-2 preparation is used for sealing off the PDMS-1 microchannel reservoirs (see Fig. 5.4) and coating a glass microscope slide on which the finished PDMS-1 microchip was to be placed. Using a different concentration of curing agent-PDMS leads to a better bonding between the layers. The glass slide provides rigidity to the microchip and facilitates its placement on the microscope chip-holder. Using a glass slide coated with PDMS-2 also leads to an all-PDMS wall of the microchannel for having a consistent and symmetric zeta-potential profile (see Chapter 6 for details).

- **Preparation of the glass slide:** The glass slide was cleaned with Iso-Propanol and Acetone and blow dried by a jet of Nitrogen gas. It was exposed to plasma for $1min$ and was then spin-coated by the PDMS-2 solution. The spin-coating was performed at $1750rpm$ for $30s$ at an angular acceleration of $300rpm/s$.

- **PDMS curing:** The master mold was placed in a Petri dish and the resulting PDMS-1 solution was poured over it. The master mold with the PDMS-1 solution was degassed again to remove any remaining trapped air bubble. Then it was placed in an oven at a temperature of $65°C$ for $25mins$ along with the spin-coated glass slide. The remaining PDMS-2 solution was poured on an empty Petri dish and placed in the oven along with the other solutions.

- **Preparation of the microchip:** The cured PDMS-1 is peeled off from the master mold and the microchannel design is cut-off from it. Now, holes are punched in the microchannel to create the reservoirs and the surface is cleaned using an adhesive tape (Scotch tape). Both of reservoirs attached to the microchannel were $5mm$ is diameter with a height of $\sim 7mm$ (see Fig. 5.4). There were two holes punched in the top PDMS layer, one for the liquid carrying tube and another for the *Platinum* electrode. Both, the PDMS-1 microchannel and the PDMS-2 coated glass chip are exposed to the plasma for $45s$ and bonded together (see Fig. 5.4). Finally, the cured PDMS-2 layer in the Petri-dish was cutout in order to cover the reservoirs on the PDMS-1 channel. For

each reservoir, two $1mm$ holes were punched on the PDMS-2 cover, one for the inlet tube and another for the electrode. This PDMS-2 cover was exposed to plasma and placed on the top of the PDMS-1 layer, covering the reservoirs. This final assembly of a microchip was placed in an oven at $65°C$ for 48 hours to enhance bonding between the layers before being used for the experiments.

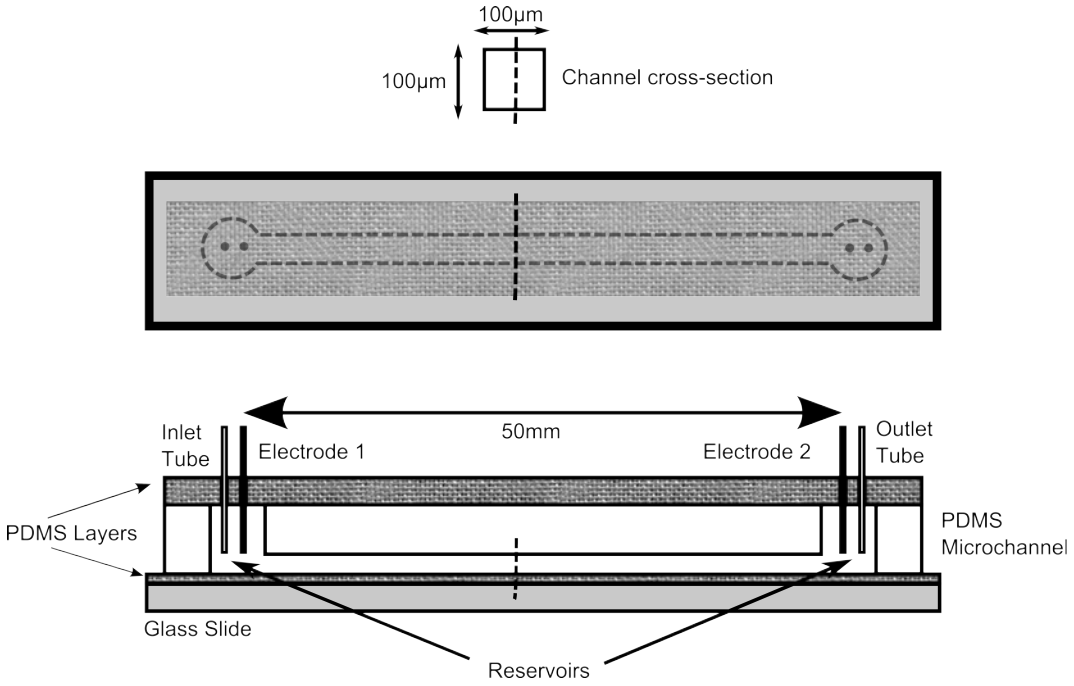

Figure 5.4.: Schematics of the a sample microchip with rectangular cross section and connections

5.3. Experimental setup

The objective of the experimental setup was two fold. Firstly, to determine the flow velocity distribution in a microchannel under the influence of a combined pressure driven and electro-osmotic flow. Secondly, to observe the interfacial dynamics between two immiscible fluids under a time-dependent electro-osmotic flow. In order to fulfill the first objective, an aqueous electrolytic solution was injected in the microchannel which was seeded with tracer particles (the details of which will be provided in Chapter 6). The motion of the tracer particles was recorded by the help of a phase-contrast microscope (see sec. 5.3.2). Similarly, for attaining the second objective, the two immiscible fluids were injected with the help of two syringe pumps and the time-dependent electric field was applied using an AC generator (see

sec. 5.3.3). Details of the various components used are provided below (see Fig. 5.5 and Fig. 5.6 for the schematics and the real setup).

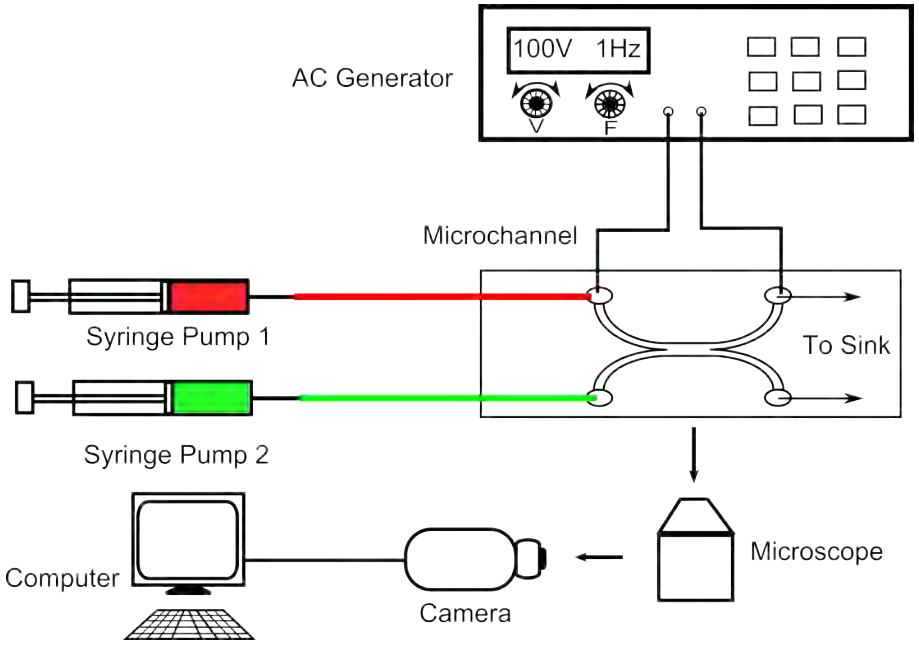

Figure 5.5.: Schematics of the experimental setup

5.3.1. Sample injection setup

For the two immiscible fluid system, the fluid samples were injected into the microchip using two infusion type syringe pumps with different flow rates. The syringe pumps used were of the model *Legato100* by *KD Scientific* with a minimum flow rate of $2.551nl/min$ and a maximum flow rate of $2.649ml/min$. The syringes used were *Glass Gas Tight 1mL Fixed Luer Lock Tip* syringes by *SGE Analytical Science*. The syringes were connected to the microchip reservoirs using Teflon (PTFE) Tubing with $1/16"OD \times 0.5mmID$.

5.3.2. Image acquisition system

A phase-contrast microscope was used to distinguish the two phases in the experiments, namely, the tracer particles and the solvent in the first set of experiments and the oil-phase and the aqueous phase in the second. The microscope used was

(a)

(b)

Figure 5.6.: The experimental setup including the (a) Phase-Contrast microscope, Syringe pump, micro chip and (b) ac generator.

of the model *IX51* made by *Olympus* (see Fig. 5.6a). It had two objectives of the model *LUCPLAN FL N* by *Olympus*, the first one with a magnification of 10× with a numerical aperture of 0.25 and the second one with a magnification of 60× with a numerical aperture of 0.70. The illumination was provided by a $30W$ halogen lamp. The microscope was interfaced to a computer by a USB camera. The images and the videos made for this study were of the resolution 508×384 pixels with a minimum exposure time of $45.28\mu s$ (for 10×) and $90.56\mu s$ (for 60×) at a frame rate of $26fps$.

5.3.3. Electric Field Generator

The electric field was applied to the microfluidic system by an *Agilent 6811B AC* power source which had a power rating of $325VA$ with a RMS voltage of $300V$ (see Fig. 5.6b). For the first part of the experiments, a DC voltage in the range of $50-400V$ was applied and for the second part of the experiments, an AC voltage in the range of $50-300V$ was applied along with frequencies varying from $0.1-20Hz$. A platinum wire was used to apply electric field to the reservoirs attached to the

microchannel. The Platinum wires were soldered to copper wires connected to the AC power source.

6. Experimental Investigation of the Electrokinetic Instability

6.1. Overview

In this chapter the experimental investigation of the electro-kinetically induced interfacial instability between two immiscible liquids is studied. To that end, firstly, the EOF setup was tested for a velocity of a combined pressure-driven and electroosmotic flow field obtained using the Micro-Particle Tracking Velocimetry (μ-PTV) technique. This helps to identify the liquid-substrate zeta potential, which is one of the most important parameters required to characterize the EOF in a system. The substrate zeta potential is a function of the various parameters such as, electrolytic concentration, pH of the solution, ionic affinity of the substrate, etc. One of the most popular methods used to estimate the substrate zeta potential is by obtaining the velocity field in an EOF. As, EOF has a plug type velocity profile for thin Debye layers, one can use the Helmholtz-Smoluchowski relationship to obtain the substrate zeta potential after having known the magnitude of the velocity and magnitude of the applied electric field. Next, an extensive study of electro-kinetic interfacial instability between two immiscible liquids is presented.

6.2. Combined Pressure-driven and Electro-Osmotic Flow

One of the most important parameters in order to characterize the EOF in a microchannel, is the substrate zeta potential. One way to obtain this parameter is to measure the EOF velocity in a channel and using Helmholtz-Smoluchowski relationship (see Chapter 2) [Saville (1977)] with known liquid properties such as permittivity ($\varepsilon_r\varepsilon_0$), dynamic viscosity ($\mu$), and the magnitude of the applied electric field (E_{app}).

However, obtaining an ideal EOF in an experimental scenario is not easy and multiple factors influence the measured velocity profile such as, back pressure due to non-similar reservoirs, softness of the substrate material and variation in the liquid properties due to Joules heating etc. Investigating a combined pressure-driven and electro-osmotic flow serves a two-fold purpose, firstly, one can estimate the effect

of an induced back-flow on the EOF velocity distribution and secondly, it helps to understand the role of the imposed flow rate during the electro-kinetic interfacial instability of liquids. Hence, an analytical model was developed to explore the fluid flow in a rectangular microchannel under a combined effect of an electric field (E_{app}) and a applied flow rate (Q_P). The channel under study has a rectangular cross-section ($2H \times 2W$) and all the walls are assumed to be at a constant zeta potential, ζ_b (see Fig. 6.1).

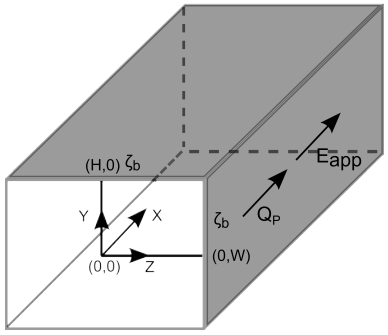

Figure 6.1.: Schematics of a rectangular channel under a combined pressure driven and EOF.

6.2.1. The electric potential distribution

The electric potential distribution in the microchannel is a combination of the electric potential due to the ionic space-charge distribution and the electric potential due to the applied potential bias. The potential distribution due to the ionic space-charge distribution in a rectangular channel can be obtained by the 2D form of the Poisson-Boltzmann equation (see 2.3.11), which for low substrate zeta potential (i.e. with Debye-Hückel approximation) (see 2.3.14) in the non-dimensional form can be written as,

$$\frac{\partial^2 \Phi_{sc}}{\partial Y^2} + \frac{\partial^2 \Phi_{sc}}{\partial Z^2} = \frac{\Phi_{sc}}{De^2} \tag{6.2.1}$$

As the system is symmetric across $Y = 0$ and $Z = 0$, the symmetry boundary conditions can be written as,

$$\frac{\partial \Phi_{sc}}{\partial Y}(0, Z) = \frac{\partial \Phi_{sc}}{\partial Z}(Y, 0) = 0 \tag{6.2.2}$$

The channel walls are assumed to be at a constant zeta potential, so the respective boundary conditions are,

$$\Phi_{sc}(H, Z) = \Phi_{sc}(Y, W) = 1 \tag{6.2.3}$$

Upon solving Eqs.6.2.1-6.2.3, the resulting ionic space charge induced potential distribution can be written as,

$$\Phi_{sc}(Y,Z) = \begin{array}{l} \sum_{m=1}^{\infty} \frac{2(-1)^{m-1} cosh\left(\sqrt{\frac{1}{De^2}+\lambda_m^2} Z\right) cos(\lambda_m Y)}{H\lambda_m cosh\left(\sqrt{\frac{1}{De^2}+\lambda_m^2} L\right)} \\ + \sum_{n=1}^{\infty} \frac{2(-1)^{n-1} cosh\left(\sqrt{\frac{1}{De^2}+\lambda_n^2} Y\right) cos(\lambda_n Z)}{W\lambda_n cosh\left(\sqrt{\frac{1}{De^2}+\lambda_n^2} H\right)} \end{array} \tag{6.2.4}$$

Now the electric potential field due to the externally applied electric field can be written as,

$$\frac{d\Phi_{app}}{dX} = -\frac{E_{app} D_h}{\zeta_b} = -\frac{1}{E_R} \tag{6.2.5}$$

6.2.2. The velocity distribution

The momentum conservation equation for a Newtonian electrolytic solution with steady, incompressible, laminar and fully developed dynamics, and under the combined influence of an externally applied pressure gradient and electric field can be written as (see Chapter 2),

$$0 = -\frac{dp}{dx} + \mu\left(\frac{\partial^2 u}{\partial y^2} + \frac{\partial^2 u}{\partial z^2}\right) + \varepsilon_r \varepsilon_0 \frac{\partial \phi}{\partial x}\left(\frac{\partial^2 \phi}{\partial y^2} + \frac{\partial^2 \phi}{\partial z^2}\right) \tag{6.2.6}$$

$$\frac{\partial^2 U}{\partial Y^2} + \frac{\partial^2 U}{\partial Z^2} = \frac{dP}{dX} + \gamma_R\left(\frac{\partial^2 \Phi}{\partial Y^2} + \frac{\partial^2 \Phi}{\partial Z^2}\right) \tag{6.2.7}$$

where, $P = \frac{D_h p_{ref}}{\mu u_{ref}}$ is the dimensionless pressure. Upon using the symmetry conditions at the channel centerlines, the boundary conditions at the channel symmetry lines, $Y = 0$ and $Z = 0$ can be written as,

$$\frac{\partial U}{\partial Y}(0,Z) = \frac{\partial U}{\partial Z}(Y,0) = 0 \tag{6.2.8}$$

and no slip condition at the channel walls, $Y = H$ and $Z = W$ as,

$$U(H,Z) = U(Y,W) = 0 \tag{6.2.9}$$

The above system of equations is linear and hence once can split the velocity field as a combination of the pressure-driven velocity field (U_P) and the electro-osmotic velocity field (U_E). The net velocity field is then, $U(Y,Z) = U_P\left(Y, Z, \frac{dP}{dX}\right) + U_E(Y, Z, \gamma_R)$. Since, a syringe pump is used in the experiments, which imposes a known flow rate

rather than a pressure gradient, the pressure gradient term, $\frac{dP}{dX}$ can be expressed in the terms of the flow rate by calculating the dimensionless flow rate as,

$$Q_P = 4\int_0^W \int_0^H U_P\left(Y,Z\right) dY\, dZ \tag{6.2.10}$$

The resulting velocity field for a combined pressure-driven and EOF can be obtained as,

$$\begin{aligned} U\left(Y,Z\right) =& Q_P \frac{H^2}{2} \frac{1-\frac{Y^2}{H^2}+\sum_{m=1}^{\infty}\frac{4(-1)^n cosh(\lambda_m Z)cos(\lambda_m Y)}{\lambda_m^3 H^3 cosh(\lambda_m W)}}{\frac{4H^3W}{3}-\sum_{m=1}^{\infty}\frac{8sinh(\lambda_m W)}{\lambda_m^5 H cosh(\lambda_m W)}} \\ &+ \gamma_R \sum_{n=1}^{\infty}\frac{2(-1)^n}{\lambda_n H}\left\{\frac{cosh\left(\lambda_n Z\right)}{cosh\left(\lambda_n W\right)}-\frac{cosh\left(\sqrt{\frac{1}{De^2}+\lambda_n^2}Z\right)}{cosh\left(\sqrt{\frac{1}{De^2}+\lambda_n^2}W\right)}\right\} cos\left(\lambda_n Y\right) \\ &+ \gamma_R \sum_{q=1}^{\infty}\frac{2(-1)^q}{\lambda_q W}\left\{\frac{cosh\left(\lambda_q Y\right)}{cosh\left(\lambda_q H\right)}-\frac{cosh\left(\sqrt{\frac{1}{De^2}+\lambda_q^2}Y\right)}{cosh\left(\sqrt{\frac{1}{De^2}+\lambda_q^2}H\right)}\right\} cos\left(\lambda_q Z\right) \end{aligned} \tag{6.2.11}$$

where, $\lambda_{n|m} = \frac{(2(n|m)-1)\pi}{2H}$ and $\lambda_q = \frac{(2q-1)\pi}{2W}$. Here, the first term of the velocity field is due to the imposed pressure gradient through an applied flow rate (Q_P) and the second and third terms are the contributions from the EOF (γ_R).

6.3. Velocity characterization using μ-PTV

The objective of these set of experiments was to create a basic EOF in a straight microchannel with a rectangular cross-section, and characterize the velocity profile in order to predict the PDMS-aqueous solution zeta potential. To that end a basic EOF setup was established (see Chapter 5 for details) and an EOF was created while seeding the fluid by micro-particles. Further, Particle Tracking Velocimetry (PTV) was used to obtain the velocity distribution in the system.

PTV is a velocimetry technique which can be understood as a "low particle density" Particle Image Velocimetry (PIV) [Malik et al. (1993)]. This technique measures the Lagrangian velocity of the medium by tracking the displacement of isopycnic (same density) particles over a period of time. The velocity is computed by analyzing two consecutive image frames for the displacement of a particle and dividing it by the time interval between the two frames. Although it is not as accurate as PIV to reproduce velocity fields with high spatial distribution, because the velocity distribution information obtained is quite sparse. It is however quite fast and easy

to setup. In order to get the particle images, the liquid seeded with the particles is introduced in the microchannel and is illuminated by a light source. The image sequence is recorded by a camera and then analyzed by *PTV Lab* [Brevis et al. (2010)], a *MATLAB* based open-source PTV toolbox.

6.3.1. Experimental Procedure

Preparation of the liquid sample

The EOF of an aqueous electrolyte is very sensitive to the electro-chemistry of the system, specifically, the salt solubility and ionic conductivity, which in turn are strongly affected by the ambient parameters such as room temperature and pressure. Moreover, the application of an external electric field sets off a series of Faradaic reactions, changing the ionic concentration in the reservoirs and hence creating a concentration and pH gradient in the electrolyte. Such properties in turn affect the flow parameters such as substrate zeta potential, Debye length, solvent permittivity and viscosity. So, in order to enhance the reproducibility, one has to ensure constant ionic conductivity, constant pH and constant ambient conditions. To that end, one can prepare the electrolytic solution in bulk and store it in controlled ambient conditions.

The first step towards preparing an electrically conductive solution for EOF is to prepare a base buffer solution. This base buffer solution is used to set the pH of the solution and stabilize the electro-chemistry of the solution by maintaining its pH and ionic conductivity during the course of the experiments [Persat et al. (2009a)]. The choice of a buffer depends upon the specific application of the system under study. One of the most commonly used buffers which mimic a biological system (pH $5.5 - 8.6$) as well as have minimum experimental side-effects are listed by Good et al. (1966) and are commonly known as *Goods Buffers.* During this study a weakly basic *HEPES Hemisodium* buffer (Sigma-Aldrich) was used which has a pH of 7.5 and works within a pH range of $6.8 - 8.2$. A $300ml$ of $10mM$ *HEPES* Hemisodium (Molar mass: $249.30g/mol$) buffer was prepared by mixing $0.7979g$ of the buffer salt into $300ml$ of de-ionized water. In order to enhance the electrical conductivity of the liquid, a neutral ionic salt was added to this base buffer solution and the ionic conductivity of the solution was measured. The ionic salt that was used in the experiments was *Potassium Chloride (KCl)* (Sigma-Aldrich). A $200ml$ solution of $0.1M$ *KCl* (Molar mass: $74.56g/mol$) was prepared by mixing $1.4936g$ of *KCl* in $200ml$ of de-ionized water. Two solutions with different electrical conductivities ($750\mu S/cm$ and $1500\mu S/cm$) were prepared by slowly adding this *KCl* solution to the *HEPES* buffer.

Seeding particles

In order to perform the PTV, small particles were introduced in the liquid sample. As the ideal particles for PTV should have the same density and shear behavior as the liquid medium, it is almost impossible to find such particles. So, in order to minimize the distinction between the seeding particles and the liquid media, one has to identify various specific forces acting on the particles. One of the most common forces acting on a solid particle in a solid media are buoyancy, drag and Coulombic (Electrophoretic) forces in electrodynamic situations. One can reduce the effect of buoyancy on the particle dynamics by choosing the particles material to have a density matching that of the liquid media. In order to reduce the effect of drag, one can choose spherical particles with very small diameter. Finally, to reduce the electrophoresis one can choose particles with very low surface charge density.

Another aspect regarding the particle sizes is that they have to be large enough to scatter light while small enough to clearly resolve their displacement between two frames. So a balance has to be struck in between drag reduction, light scattering and displacement resolution with respect to particle sizes. Further, the particle distribution in the liquid media has to be chosen such that there is very negligible influence of velocity field around. In the present study, *Carboxylate modified Polystyrene (latex) beads* (Sigma-Aldrich) were used as seeding particles where particle diameter was $0.9 - 1.1\mu m$, density was $1.045 - 1.055 g/l$ and charge density was $\leq 0.008 milliequivalents\,(mEq)$. The particles were provided in an aqueous suspension where the solid concentration was 2.5%, which corresponds to about $5 \times 10^9 particles/ml$. To prepare the liquid sample with seeded particles, $10ml$ of the liquid sample prepared above was mixed with $20\mu l$ of the particle suspension which lead to approximately $10^7 particles/ml$ of the liquid sample.

Filling and cleaning of the microchannel

The PDMS microchannel that was used in this study was a $5cm$ long microchannel with a rectangular cross-section of $100\mu m \times 100\mu m$ (see Fig. 5.4). It was prepared by the soft lithography technique as detailed in Chapter 5. During the filling process of the microchannel with the liquids, it was made sure that no visible air bubbles are present in the syringe and the connecting tube. The first reservoir was allowed to fill until the liquid started coming out from the hole for the first electrode. Then that hole was closed by inserting the electrode and the second reservoir was allowed to fill keeping the sink tube blocked and second electrode hole open. Similarly, when the liquid started coming out of the hole for the second electrode, it was closed by inserting the second electrode after opening the sink tube to the atmosphere. The same process was repeated for each of the subsequent filling process to ensure that both the reservoirs are completely filled with the liquid pumped. In order to clean the microchannel, firstly, the microchannel was washed with de-ionized water for $20 mins$ and then with $0.1M\ NaOH$ for $20 mins$. Finally, the sample solution was

introduced in the microchannel and images were recorded for various combinations of applied electric field and flow rates.

Image acquisition

A phase-contrast microscope (for details see Chapter 5) was used in order to obtain a sequence of images for the PTV. The microscope objective with a magnification of $60\times$ and a numerical aperture of 0.7 was used in these experiments (see Chapter 5). The depth of field hence calculated lied in the range of $1.2 - 1.7\mu m$. The small depth of field (which approximately corresponds to the particle diameter) is good to image particles in a thin focused plane, nevertheless, out of focus plane traversal of particles was also observed, leading to few blurred particle images. Since particles were imaged against the light source, the maximum amount of light scattered by the particles was in the direction perpendicular to the plane of imaging and hence the images show actually a shadow of the particles. For each reading of the different combinations of the flow rate and electric field, a video of 500 frames was recorded by a CCD camera with a frame rate of $26fps$ and exposure time of $90.56\mu s$. Although recording images provide a better spatial resolution, they need special apparatus for pulsed illumination and synchronization of various imaging components. While recording a video, a fixed time interval between two frames is used, eliminating the need of a pulsed source. Each image had a resolution of 508×384 in $8-bit$ grayscale.

Post-processing

The post-processing steps include image frame extraction from the raw video, removal of background noise, correlative analysis of the image frame sequence, calibration of pixel to distance and finally, extraction of the mean velocity distribution. In order to extract image frames from the raw video, *VirtualDub v1.9.11* software was used, where 100 frames were extracted out of 500 recorded frames. Later, the image sequence was imported to *ImageJ v1.47* software where the image colors were inverted so that particle shadows appear as bright particles on a dark background (a requirement for using *PTV Lab* software) (see Fig. 6.2). Next, a background image was chosen to subtract noise from each of the images from the image sequence. Then, a contrast enhancement was carried out and the image sequence was exported.

Now, these images were imported into *PTV Lab* and a region of interest (ROI) encompassing the particles bounded by the channel walls was selected. In order to detect the particles, *Gaussian Mask algorithm* (a fast algorithm for low density particles) was chosen [Brevis et al. (2010)] with the particle correlation threshold set as 0.5, sigma (particle diameter) as $3pixels\ (px)$, and intensity threshold as 25/255 on a $8-bit/px$ grayscale. The cross-correlation parameters for consecutive image frames were fixed by setting the interrogation area (mesh size) as $40px$, and a minimum image correlation value as 0.1. After setting up the processing parameters, the PTV

analysis was allowed to run. After the PTV analysis run was finished, in order to filter out the spurious velocity data, a vector validation step was carried out. By applying a cutoff on the obtained velocity magnitudes (such as $u > 0$ and $v \sim 0$) the spurious velocity data was filtered out. The next step involved the calibration of the image in order to convert pixel information into geometric distance, which for the present system corresponds to $\sim 2.5 px/\mu m$. Finally, a mean of the velocity profile is calculated and exported as a .dat file.

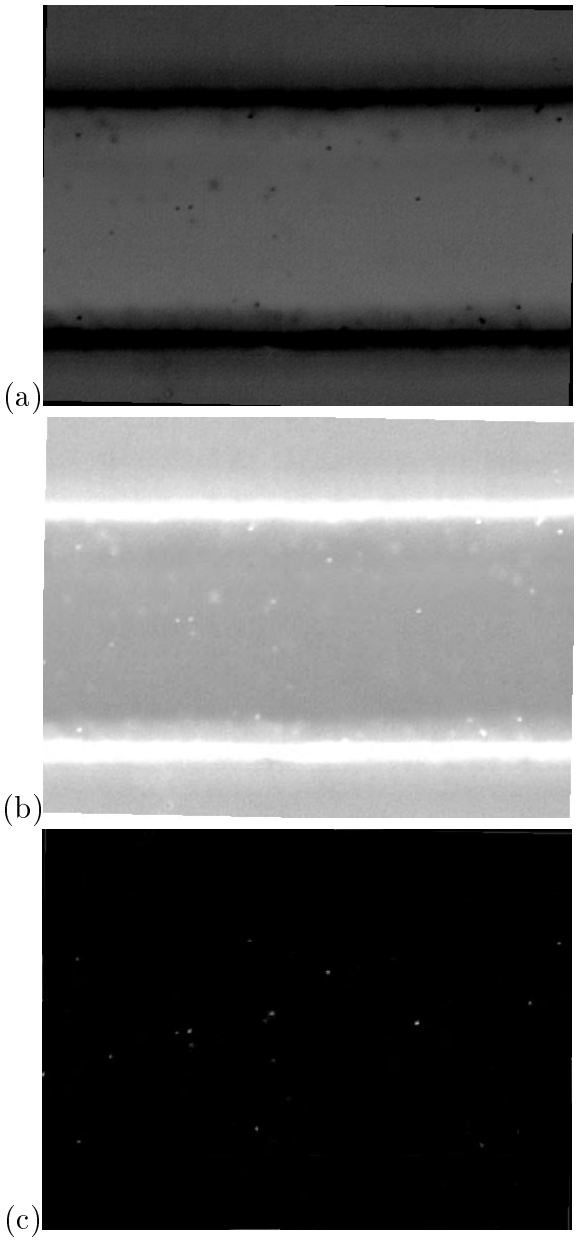

Figure 6.2.: PTV Image pre-processing steps - (a) Image as obtained by the CCD camera, (b) Color inverted image, and (c) Image after background removal.

6.3.2. Results and Discussions

The reported values of PDMS-aqueous electrolyte surface zeta potential at a pH of 7.5 lies in the range of $-20mV$ to $-40mV$. In order to compare the experimentally obtained velocity profile with the theoretically obtained velocity profile (see Eq. 6.2.11) one has to estimate the mentioned dimensionless parameters. The

values of the fluid properties were taken as, dielectric constant of the aqueous solution, $\varepsilon_r \sim 80$, permittivity of vacuum, $\varepsilon_0 \sim 8.85 \times 10^{-12} F/m$, dynamic viscosity, $\mu \sim 1 centi Poise\,(cP)$ with the ambient temperature at $293K$ and pressure at $1atm$. With the surface zeta potential varying from $20mV$ to $40mV$ and the applied electric field varying from $10V/cm$ to $80V/cm$, one can estimate the electro-osmotic reference velocity $u_{E,ref}$ as,

$$\begin{aligned} u_{E,ref} = u_{HS} &= -\frac{\varepsilon_r \varepsilon_0 \zeta_{wall} E_{app}}{\mu} \\ &= \frac{80 \times 8.85 \times 10^{-12} \times [20, 40] \times 10^{-3} \times [10, 80] \times 10^2}{10^{-3}} m/s \\ &= [0.014, 0.227]\, mm/s \end{aligned} \tag{6.3.1}$$

where, $[x, y]$ represents the range of the parametric variation. The imposed flow rates used in the following study ranged from $25nl/min$ to $1000nl/min$. The reference velocity estimate as created by an imposed flow rate for a channel cross-sectional area of $100\mu m \times 100\mu m$ can be calculated as,

$$\begin{aligned} u_{P,ref} &= \frac{Imposed\, Flow\, Rate}{Area} = \frac{[25, 1000] \times 1.67 \times 10^{-11}}{10^{-8}} mm/s \\ &= [0.042, 1.67] mm/s \end{aligned} \tag{6.3.2}$$

Different velocity profiles were obtained from the PTV for different combinations of flow rates and applied electric fields. For a pure EOF, i.e. in the absence of an imposed flow rate ($\bar{Q}_p = 0$), the EOF velocity profile as obtained by the PTV analysis can be compared to the theoretical velocity distribution (see Eq. 6.2.11) to estimate the PDMS-electrolyte zeta potential (see Fig. 6.3). The estimated values of PDMS-electrolyte zeta potential were found to be within the range of reported values in the existing literature [Kirby and Hasselbrink (2004b)].

6.4. Electrokinetically Induced Interfacial Instability

In order to study the impact of electrokinetic effects on the interfacial stability of immiscible liquids, a set of experimental investigations were performed over a varied set of electric field strengths, frequencies, imposed flow rates and surface tension.

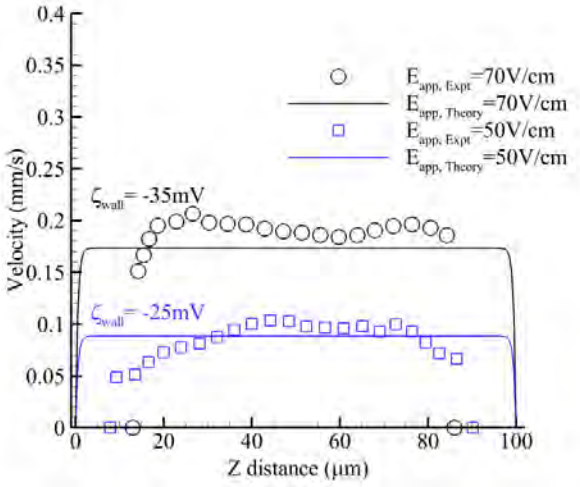

Figure 6.3.: Estimate of PDMS-aqueous electrolyte zeta potential by matching the EOF velocity profiles.

The objective of this study was to observe the interfacial behavior of immiscible liquids under time-periodic electric fields and to characterize the critical parameters such as the imposed flow rate, amplitude of the electric field and its frequency. Since the focus of this study was on electrokinetics, one of the two immiscible liquids was necessarily electrically conductive (an aqueous electrolyte).

It is known that surface tension effects are quite dominant over body forces on microscales where the surface to volume is very high. So in order to observe the effect of surface tension also, two different liquid combinations were used, namely, oil and electrolyte, a case of finite surface tension, and de-ionized water and electrolyte, a case of zero surface tension (miscible fluids). Further, two different fluid-fluid configurations were tested for interfacial instability, namely, one-interface case and two-interface case (see Fig. 6.4). In the one-interface case, the conductive fluid is geometrically bounded by a non-compliant wall which participates in the EOF dynamics by providing a sustained viscous dissipative layer and hence enhancing the stability of the system. The two-interface case presents a case of relatively non-constrained liquid-liquid interface where capillary effects dominate over viscous dissipation. In order to observe the interfacial dynamics in both of the cases, the phase-contrast microscope with a CCD camera was used to record the interfacial dynamics under various combinations of mentioned control parameters. Each of the mentioned setup step is detailed subsequently.

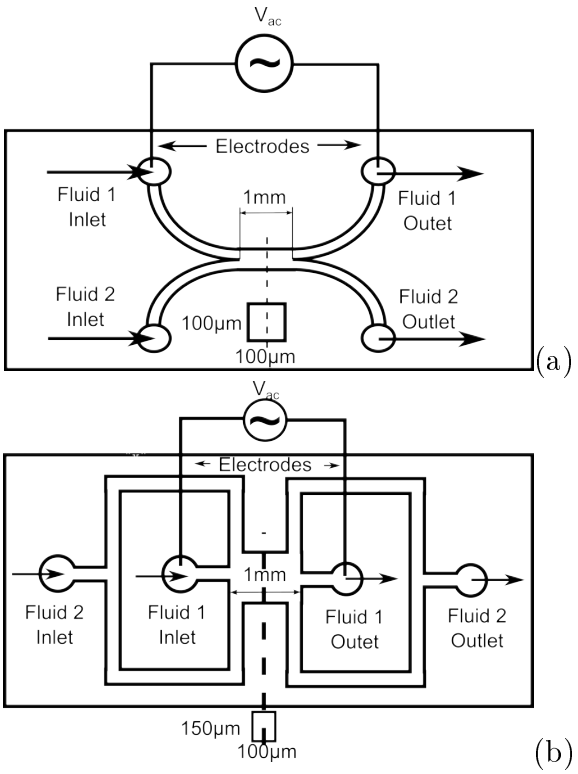

Figure 6.4.: Schematics of the microchannel used for interfacial instability studies (a) channel schematics for 1-interface configuration (b) channel schematics for 2-interface configuration.

6.4.1. Experimental Procedure

Preparation of the liquid samples

In this experimental study of two-phase flow, three distinct liquid samples were created. The first liquid sample (henceforth referred to as FS-1) was an aqueous electrolyte, which had a *HEPES* buffer base while $0.1M$ *KCl* was used to enhance the conductivity of the solution similar to the previous study (see sec. 6.3.1). The second liquid sample (henceforth referred to as FS-2) consisted of *Hexadecane* ($C_{16}H_{34}$, *Sigma Aldrich*) mixed with $3\%w/w$ of *SPAN-80* (*Sigma Aldrich*) surfactant. This leads to a surface tension of $4.05 \pm 0.29mN/m$ [Hashimoto et al. (2008)]. The mentioned concentration of SPAN-80 is its critical micelle concentration (CMC) in *Hexadecane* and hence the value of the surface tension obtained is the corresponding limiting value. So, in order to prepare the FS-2, $100g$ of Hexadecane (Molar mass: $226.44g$) was mixed with $3g$ of SPAN-80 (Molar mass: $428.62g$). The choice of SPAN-80 as a surfactant to reduce Hexadecane-water surface tension is due to insolubility of SPAN 80 in water and hence it does not interfere with the EOF. The third liquid sample (henceforth referred to as FS-3) was de-ionized (DI) water

mixed with *Rhodamine-B* (*Sigma-Aldrich*) dye. This solution was used along with the FS-1 for a two-fluid flow experiment with zero surface tension. Rhodamine-B dye, which has a low diffusivity in water ($D_{RB} \sim 3.7 \times 10^{-6} cm^2/s$), was used to highlight the non-conductive phase i.e. the DI water. A $100ml$ solution of $0.01M$ of Rhodamine-B (Molar mass: $479.01g$) was made by mixing $0.479g$ of Rhodamine-B powder in $100ml$ of DI water.

Filling and cleaning of the microchannel

The PDMS microchannel that was used in this study has $1mm$ long two-phase interfacial region along with a cross-section of $100\mu m \times 100\mu m$. It was prepared by the soft lithography technique as detailed in the Chapter 5. During the filling process of the microchannel with the liquids, it was made sure that no visible air bubbles are present in the syringe and the connecting tube. Firstly, all the Platinum electrodes were disconnected from the reservoirs and the liquid 1 inlet reservoir was allowed to fill the inlet reservoir until the liquid started coming out from the hole for the first electrode. Then, the electrode hole of the first reservoir was closed by inserting the electrode. Then, the outlet reservoir was allowed to fill while keeping the outlet tube blocked and the second electrode hole open. Similarly, when the liquid started coming out of the electrode hole of the outlet reservoir, the hole was plugged by inserting the second electrode and the outlet tube was opened. The same process was repeated for each of the subsequent filling process to ensure that both the reservoirs are completely filled with the liquid pumped. In order to clean the microchannel, firstly, the microchannel was washed with de-ionized water for $20mins$ and then with $0.1M$ $NaOH$ for $20mins$. Finally, the FS-1 solution was introduced in the microchannel and then FS-2 (or FS-3) were introduced in the liquid 2 inlet using another syringe pump. The flow rates of the FS-1 and FS-2 (or FS-3) were adjusted in order to have a flat and stable interface. Then, the AC electric field was applied for different combinations of electric field magnitude and frequency and they were varied along with the imposed flow rate until the interface broke or oscillated vigorously.

Image acquisition

The phase-contrast microscope (for details see Chapter 5) was used to record videos of the two-phase interfacial dynamics. The microscope objective with a magnification of $10\times$ and a numerical aperture of 0.7 was used. For each reading of the different combination of the flow rate, amplitude and frequency of the electric field, a video of 500 frames was recorded by a CCD camera with a frame rate of $26fps$ and exposure time of $45.28\mu s$. Each video had a resolution of 508×384 in $8 - bit$ grayscale.

Post-processing

The post-processing steps include processing of the raw video in order to extract amplitude and frequency of the interfacial perturbation. In order to process the raw video, *Virtual Dub v1.9.11* software was used, where 200 frames were extracted out of 500 recorded frames. Later, the image sequence was imported to *ImageJ v1.47* software and the following procedure was followed. In order to extract the maximum amplitude of the interfacial waves at a x-location, a distribution of pixel intensities was plotted over the 200 frames. Since there was a jump in pixel intensity across the interface, the time taken (number of frames) between two consecutive peaks of pixel corresponded to the frequency of the interfacial vibrations and the difference between the crest and the trough gave the displacement of the interface at that x-location. The images were calibrated by using a factor of $\sim 1.25\mu m/px$ for the one-interface system and $\sim 1.67\mu m/px$ for the two-interface system. Finally, this distribution of interfacial displacement is exported as a .dat file.

6.4.2. Results and Discussions

Miscible liquids (without surface tension)

In this set of experiments, the interfacial behavior between two miscible liquids with a conductivity gradient was studied under three major tunable parameters, namely, the imposed flow rate, the amplitude and the frequency of the AC applied electric field. In order to have a distinct and planar phase boundary (interface) between the two liquids, it was necessary to minimize the diffusion length of Rhodamine B in the transverse direction by imposing a convective flux of the solution. This convective flux was achieved by imposing a flow rate with the help of a syringe pump. In all cases, the direct contact surface between the two fluids was $L = 10^3\mu m$ in length and $H = 100\mu m$ in depth. The diffusive length of Rhodamine B can be estimated from the Fick's law as, $\delta = 2\sqrt{Dt}$, where D is the diffusion coefficient of Rhodamine B, and t is the time taken by the Rhodamine B to diffuse over a length of δ. The time taken by the liquid to traverse the channel length (L) can be estimated as $t = LS/Q_P$, where Q_P is the imposed flow rate, $S = W \times H$ is the half cross-sectional area of the channel with the channel half-width, $W = 50\mu m$. So, upon equating the two time spans,

$$Q_P = \frac{4DLS}{\delta^2} \tag{6.4.1}$$

For $D = 3.7 \times 10^{-10} m^2/s$ and $\delta \leq W$, one can estimate a limiting flow rate, $Q_P \geq 178nl/min$. Another limitation on flow rate is that the magnitude of electro-osmotic velocity ($u_{E,ref}$) and the pressure driven velocity ($u_{P,ref}$) should be of comparable magnitudes. For a maximum applied electric field of $80V/cm$, one can estimate the corresponding pressure driven flow rate (see Eqs. 6.3.1 and 6.3.2) as $\sim 68nl/min$.

In the following sets of experiments, we choose to work with a wide range of Q_P $(25 - 1000nl/min)$ thus going from a flatter interface and dominant pressure driven flow, to a relatively diffused interface and a dominant electro-osmotic flow.

After doing a series of experiments with various combinations of flow rate, electric field magnitude and frequencies, it was observed that the maximum amplitude of interfacial oscillation decreases with increasing the flow rate but increases with the magnitude of the electric field (see Fig. 6.5a). Upon increasing the frequencies, it was observed that the interfacial oscillation follows the applied frequency but at higher frequencies ($> 10Hz$) the viscous relaxation dominates over the imposed electro-temporal dynamics and hence the interfacial displacement behaves independently of the applied electric field (see Fig. 6.5b). The interfacial oscillation of a miscible liquid-liquid interface is observed to be a function of the amplitude of the applied electric field (see Fig. 6.6) as well as the frequency too (see Fig. 6.7). Such an observation establishes the role of electrokinetic origin of interfacial dynamics in a miscible fluid system.

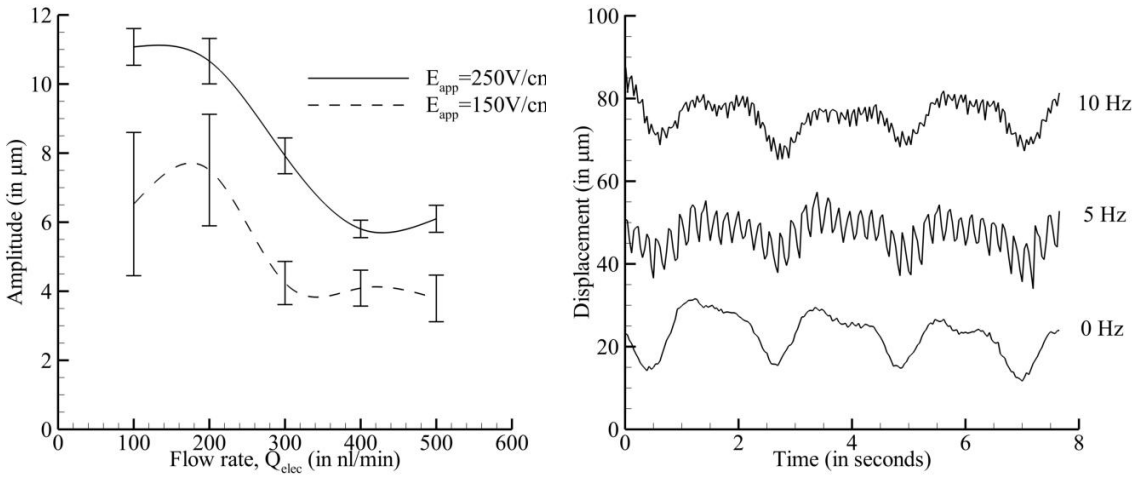

(a) (b)

Figure 6.5.: Interfacial oscillations for miscible liquids case under time periodic electric field. (a) Amplitude of interfacial oscillations as a function of imposed electrolyte solution flow rate for different time-periodic electric fields at a frequency of $1Hz$, (b) Interfacial displacement over time at an imposed flow rate of $Q_{elec} = 500nl/min$, under a time periodic electric field, $E_{app} = 300V/cm$ and different frequencies.

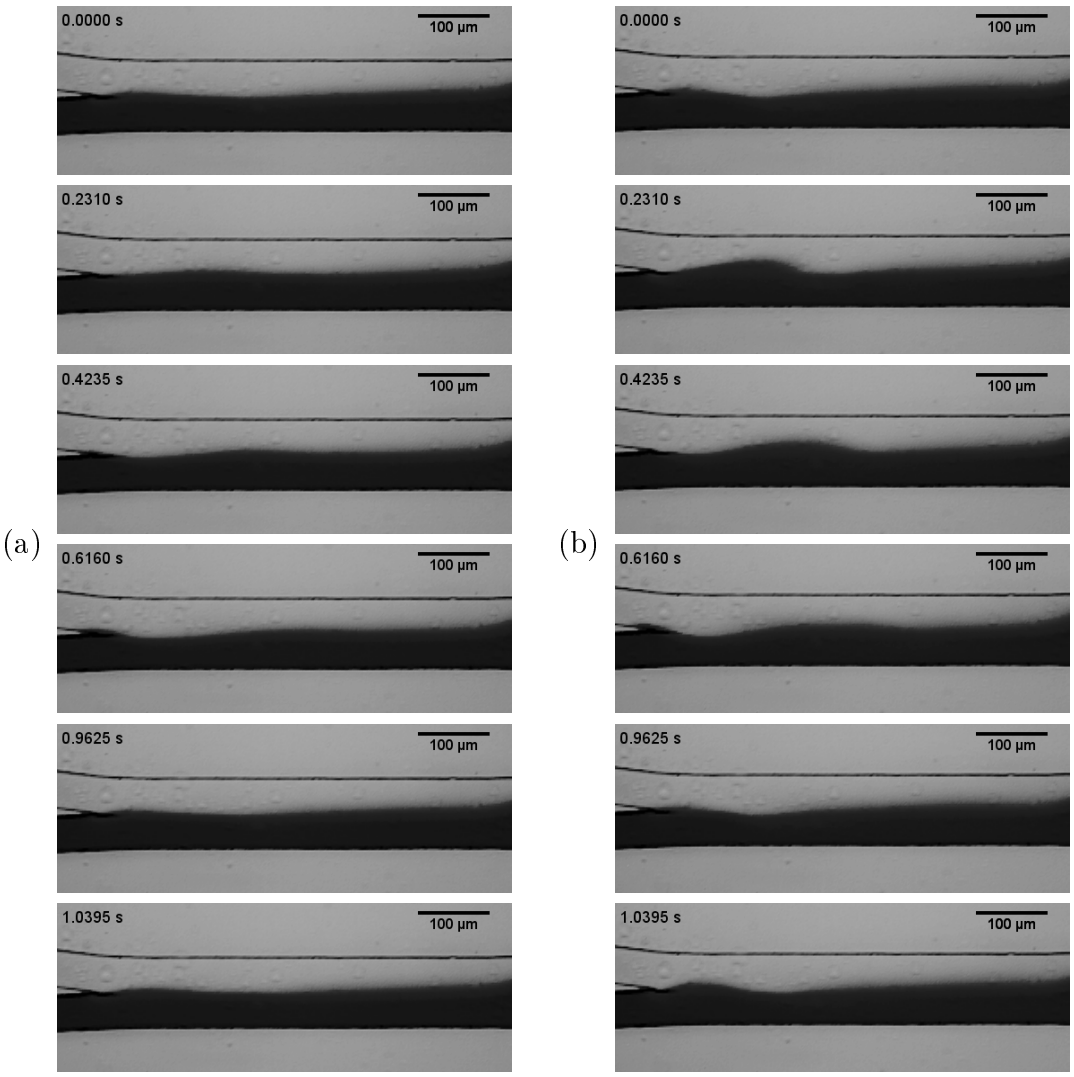

Figure 6.6.: Interfacial evolution between two miscible liquids under an AC electric field of (a)$150V/cm$ and (b) $250V/cm$ and a frequency of $1Hz$. The dark liquid is a solution of $0.01M$ Rhodamine B in DI water and the clear liquid is an aqueous electrolyte (see text for details) with a conductivity of $1500\mu S/cm$. Both liquids have an additional imposed flow rate of $300nl/min$.

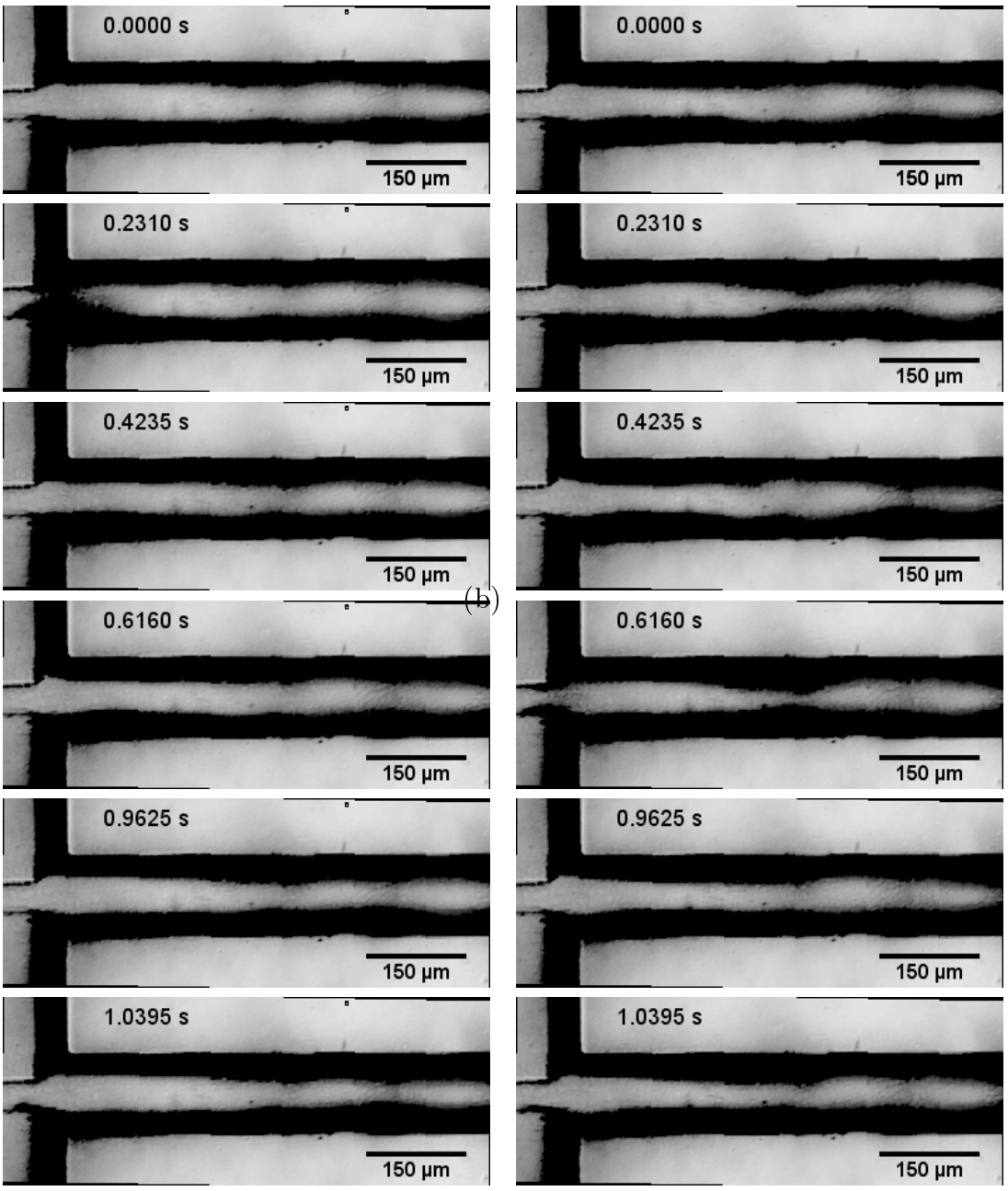

Figure 6.7.: Interfacial evolution between two miscible liquids under an AC electric field of $3000V/cm$ and a frequency of (a)$1Hz$ and (b) $2Hz$. The dark liquid is a solution of $0.01M$ Rhodamine B in DI water and the clear liquid is an aqueous electrolyte (see text for details) with a conductivity of $1500\mu S/cm$. Both liquids have an additional imposed flow rate of $500nl/min$.

Immiscible liquids

In this set of experiments, the interfacial behavior between two immiscible liquids was studied under three major tunable parameters, namely, the imposed flow rate, the amplitude and frequency of the applied AC electric field. Due to the hydrophobicity of PDMS, the aqueous electrolyte-Hexadecane ($\rho_{Hexa} = 0.773g/ml$, $\mu_{Hexa} = 3.34cP$ at $25°C$) and SPAN-80 solution system acts as a liquid-liquid jet system (see Fig. 6.8). So, in such a case, a surface-tension driven instability is highly likely leading to the breaking of the interface into droplets. It is known that in high Reynolds number flows, minimizing the droplet formation can be avoided by suppressing the Rayleigh-Plateau instability [Lasheras and Hopfinger (2000); Guillot et al. (2007)]. So, in order to have a planar interface between the two liquids, a flow rate was slowly imposed in both liquids until a flat interface was achieved. In all of the studied cases, the direct contact surface between the two fluids was $L = 10^3 \mu m$ long. These set of studies were performed over a wide range of applied AC electric fields $(50 - 300V)$, frequencies $(1 - 10Hz)$ and imposed flow rates $(100 - 1000nl/min)$. The most prominent amplitudes of oscillations of the interface were observed for a frequency of $1 - 5Hz$.

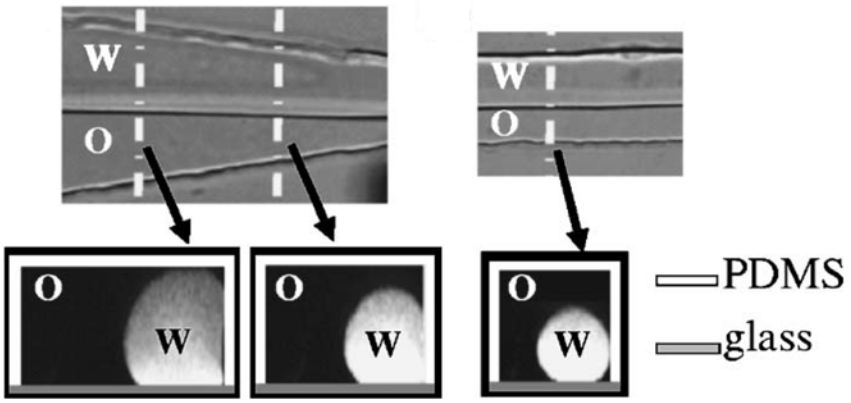

Figure 6.8.: The oil(O)-water(W) interfacial structure in a PDMS-glass microchannel as shown by Guillot and Colin (2005).

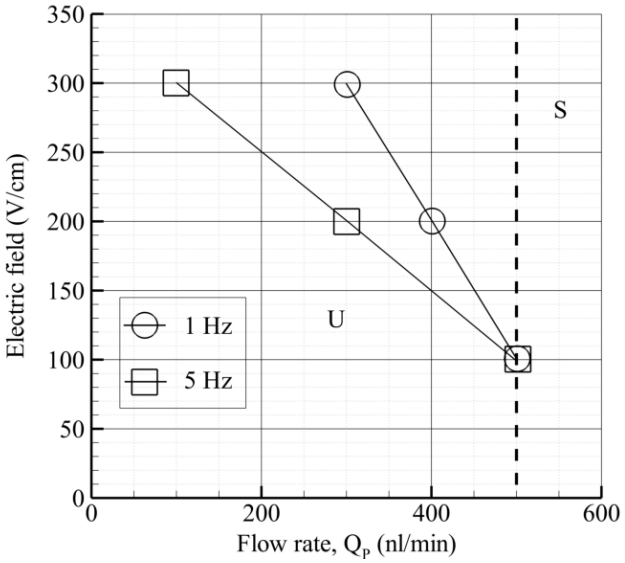

(b)

Figure 6.9.: Stability characteristics of aqueous electrolyte and Hexadecane system under various combinations of electric field magnitude, frequency and imposed flow rates. The dashed line represents the stability boundary of the system in the absence of an applied electric field. This result is for the case of one interface case between the aqueous electrolyte and Hexadecane with SPAN 80.

To characterize the stability of the system and identify the critical values of applied electric field and flow rates leading to interfacial instability, the following approach was used, Firstly, the electric field was switched off and the applied flow rate was fixed at $1000nl/min$ in each of the fluids. Then, the flow rate was reduced slowly (in the steps of $100nl/min$) until the liquid-liquid interface started oscillating and broke into droplets. Then, the same step was repeated for different values of the magnitudes of the applied electric field and frequencies. Finally, the critical magnitudes of the flow rates obtained for different values of electric field and frequencies were plotted (see Fig. 6.9).

Further, it was observed that there exists a threshold value of imposed flow rate for the interfacial stability of the immiscible fluids. This highlights the competitive dynamics between the convective inertia and the capillary forces. In the presence of a fixed value of surface tension, it is observed that the high flow rates ($> 500nl/min$) are relatively stable. It was also observed that the two-liquid system becomes more stable at higher frequencies (see Fig. 6.9 and Fig. 6.10), which leads to the inference that the time-periodic electric field induced dynamics dampen the interfacial waves prohibiting their growth.

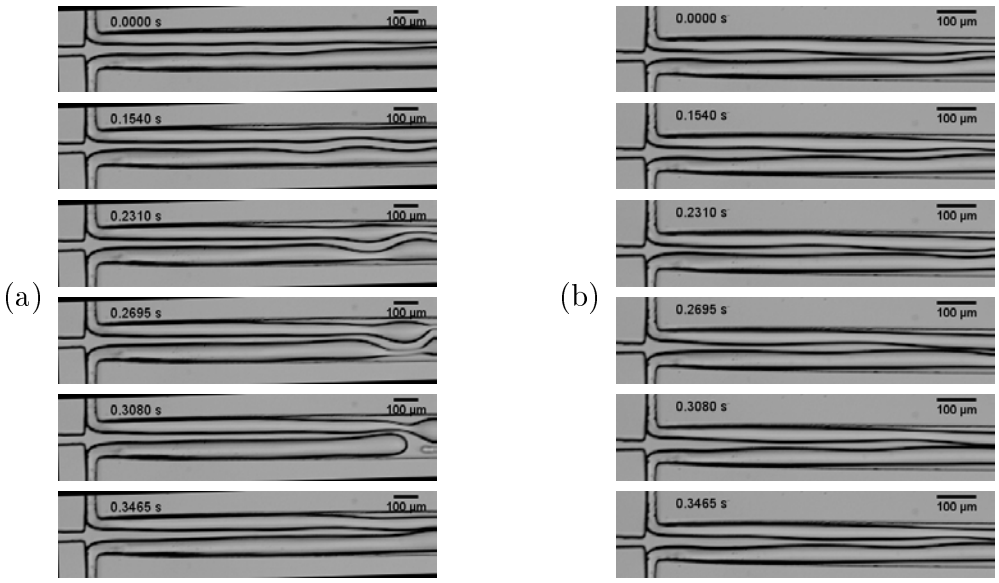

Figure 6.10.: Interfacial evolution under an AC electric field of $300V/cm$ at a frequency of (a) $2Hz$ (b) $5Hz$. The central liquid is an aqueous electrolyte (see text for details) with a conductivity of $1500\mu S/cm$ and the top and the bottom liquids are a solution of Hexadecane with SPAN 80 at $3\%w/w$. Both of the liquids have an imposed flow rate of $1000nl/min$.

6.4.3. Conclusions

The study of interfacial instability due to electrokinetics requires an understanding of the complex interactions of various physical phenomena such as capillary forces, convective and temporal inertia, diffusion, and Maxwell stresses. In this study, the interfacial instability was explored through two cases, namely, a miscible fluids case i.e. in the absence of surface tension, and an immiscible fluids case i.e. in the presence of surface tension.

In the miscible fluids case, the objective was to study the liquid-liquid interfacial deformation under a time-periodic EOF in the presence of convective and diffusive transport. To obtain a non-perturbed (flat) interface against a finite diffusion of miscible fluids, a flow rate was imposed on the liquids so that the ensuing convective flow can hinder the mixing of the two fluids by interfacial diffusion. The flow rate was kept the same in both the liquids to avoid shear induced (Kelvin-Helmholtz) instability. It was observed that for a given magnitude of applied electric field, the amplitude of the interfacial deformations decreased with increasing imposed flow rate, which ascertains the stabilizing effect of the imposed flow rate. Further, it was also observed that the responsiveness of the interface (i.e. the amplitude of the perturbed interface) to the frequency of the applied electric field, was most noticeable in the range of $1 - 5Hz$.

In the immiscible fluids case, the objective was to study the liquid-liquid interfacial deformation under a time-periodic EOF in the presence of capillary force and convective transport. To obtain a non-perturbed (flat) interface against an interface breaking capillary force, a flow rate was imposed on the liquids to counter the surface tension driven instability. It was observed that a critical value of flow rate exists above which the system remains stable for the applied range of electric fields. This suggested the existence of a competing dynamics between the convective inertia and Maxwell stresses. For a given value of flow rate, the stability of the system decreases upon increasing the magnitude of the electric field. Finally, it was observed that high frequency AC electric fields tend to stabilize the flow at a given flow rate.

6.5. Sources of Errors and Uncertainties

6.5.1. Microchannel

The defects in the microchannel can be attributed to the soft lithography technique used to fabricate the channel. Although the channel dimensions corresponding to the motif design were quite accurate (variations in dimension$< 1\mu m$), the height of the channels, which is controlled by the spin coating of the photo-resist and the further pre-exposure processes (see Chapter 5), was found to be varying over $95 - 105\mu m$ for a target height of $100\mu m$. These irregularities in the channel cross-section can lead to an expanding-contracting channel design thus affecting the flow. Moreover, the use of PDMS chips which is soft in nature and thus compliant to changes in the pressure, can further deform the channel geometry. So, in order to avoid such geometrical uncertainties, glass channels are used commonly, which have a relatively rigid construction but are costly with greater fabrication time. This, however, can be envisaged as a future development of the present experimental setup.

6.5.2. Apparatus

One of the main components of the experimental apparatus is the syringe pump. The step motor which allows the rotation of the infinite screw of the syringe pump produces periodic vibrations. Those vibrations are transmitted to the syringe piston translation and then generate periodic variations of the flow rate. In order to overcome these undesirable pulsations, one can use pressure generators, which do not generate vibrations since pressure is regulated through a pressure controller. The next important component is the AC power generator. For the current model of the AC power generator (Agilent 6811B) used, it was recommended to have the operating frequency $> 45Hz$. However, in order to obtain perceivable interfacial oscillations, we had to operate in the frequency range $\leq 10Hz$. In that range of operating frequency, the precision on the output voltage was not assured by the

manufacturer. It was found that the error in voltage output can range from 2% at $10Hz$ to $\sim 10\%$ at $1Hz$.

6.5.3. Electro-chemical

The EOF parameters such as surface zeta potential and Debye length are very sensitive to the electro-chemical reactions, which in turn are sensitive to the ambient temperature and pressure. So, in order to have a reproducible electro-osmotic system, a climate-controlled environment is required. Most of the solutions were prepared in bulk in order to have consistent concentration of the species while performing the experiments. The experiments of which the results are presented in this work, were performed over a period of two months at various times during a day in a non-climate controlled room. The key parameters such as solution pH and conductivity were measured every time before starting the experiments, but, a noticeable variation was observed in those parameters (for e.g. conductivity reduced by a value of $200\mu S/cm$ over two days). During the experiments, the Faradaic reactions at the electrodes also create an ionic concentration gradient across the channel which finally results into a pH and conductivity gradients. Such reactions also cause hydrolysis leading to gas formation in the reservoirs thus changing the reservoir pressure dynamically. Also, there are Ohmic losses in the connecting wires and electrodes which affects the actual electric potential reaching the liquids. All these issues could be addressed in future developments by putting a feedback system in the reservoirs changing the reservoir pressure and electrode potential dynamically.

7. Conclusions and Perspectives

7.1. Conclusions

The present work focuses on the role of steady and time-dependent Maxwell stress, capillary force and disjoining pressure on interfacial instability. A comparative base state analysis with the previous studies, which did not account for interfacial Maxwell stress, showed that considering Maxwell stress generated dynamics introduces significant velocity gradients at the liquid-liquid interface. Such gradients are instrumental in the interfacial instability under a time-periodic actuation as they can either attenuate or amplify the interfacial waves. The bulk penetration of near wall oscillations was found to be inversely proportional to the forcing frequency. At lower frequencies, a significant suppression of velocity dispersion was observed which asymptotes to the classical dispersion free velocity in a DC electro-osmotic flow. By the variation of interfacial polarity it was found that, one can not only control the interfacial velocity and the rate of shear transfer, but also establish a significant phase difference in fluid velocity at different transverse locations in the fluid which enhances the dispersion effects and can be effectively used in controlled species transport in microfluidic devices.

Further, in order to study the effect of interfacial Maxwell stresses in realistic rectangular channels, the solution of a free surface EOF in a microchannel of rectangular cross-section was achieved analytically. By taking into account a complete expression of the boundary condition at the free surface that includes the Maxwell stress at this interface, a parametric analysis of the flow in terms of the EDL thickness, channel aspect ratio and different fluid-fluid and solid-fluid interfacial zeta potential was carried out. With the help of two-dimensional velocity contours, it was shown that the bounding walls have a significant effect on the velocity distribution in a rectangular microchannel. The flow controlling parameters in an EOF were not only the electro-chemical properties of electrolytes which controls the EDL thickness and wall and interfacial zeta potentials, but also the geometry of the channel through the channel aspect ratio. Such a study helps identifying proper control parameters for achieving a desired flow rate and velocity distribution in a microfluidic device.

A linear stability analysis of interfacial perturbation was performed for the thin film of electrolyte under DC and AC electric fields. Through long wave asymptotic analysis of the Orr-Sommerfeld equations, parametric stability thresholds of a thin aqueous film explored with a focus on surface tension, disjoining pressure for

gas-fluid-substrate interaction, magnitude and frequency of the externally applied electric field, substrate and free surface zeta potential was highlighted.

(a) The phenomena which are observed to have a stabilizing effect on the film dynamics are surface tension, repulsive disjoining pressure ($A < 0$), osmotic pressure due to the EDL at the interfaces and viscous dissipation.

(b) The phenomena contributing towards the instability of the film are attractive disjoining pressure ($A > 0$), thin EDLs ($De \ll 1$), external electric field driving the electro-osmotic flow and low frequencies. The film stability decreases upon increasing the magnitude of the applied electric field, which is due to an increase in the tangential Maxwell stresses at the interface.

(c) The increase in the value of substrate zeta potential tends to stabilize the flow which in turn enhances the osmotic pressure component.

A set of experiments were performed in order to characterize the EOF in a rectangular microchannel. With the help of a PTV analysis, velocity distributions were obtained which agreed well to the theoretical values. This was used to estimate PDMS zeta potential, which was found to be within the reported values in the existing literature. Further, in order to study the liquid-liquid interfacial instability under time-periodic electric field, two sets of cases were considered.The first set of cases consisted of miscible fluids and the second one consisted of immiscible fluids.

In the miscible fluids case, the objective was to study liquid-liquid interfacial deformation under a time-periodic EOF in the presence of convective and diffusive transport. To obtain a non-perturbed (flat) interface against a finite diffusion of miscible fluids, a flow rate was imposed on the liquids so that the ensuing convective flow can hinder the mixing of the two fluids by interfacial diffusion. The flow rate was kept the same in both the liquids. It was observed that for a given magnitude of applied electric field, the amplitude of the interfacial deformations decreased with increasing imposed flow rate, which ascertains the stabilizing effect of the imposed flow rate. Further, it was also observed that the responsiveness of the interface (i.e. the amplitude of the perturbed interface) to the frequency of the applied electric field, was most noticeable in the range of $1 - 5Hz$.

In the immiscible fluids case, the objective was to study liquid-liquid interfacial deformation under a time-periodic EOF in the presence of capillary force and convective transport. To obtain a non-perturbed (flat) interface against an interface breaking capillary force, a flow rate was imposed on the liquids to counter the surface tension driven instability. It was observed that a critical value of flow rate exists above which the system remains stable for the applied range of electric fields. This suggested the existence of a competing dynamics between the convective inertia and Maxwell stresses. For a given value of flow rate, the stability of the system decreases upon increasing the magnitude of the electric field. Finally, it was observed that high frequency ac electric fields tend to stabilize the flow at a given flow rate.

7.2. Perspectives

The analytical modeling of the interfacial stability of a gas-liquid (liquid film) system provided interesting insights into the marginal stability characteristics of an interface under steady and time-periodic Maxwell stress while including a complex interaction of capillary and van der Waals forces. This subject has however an immense possibility to expand the scope of the present analysis to a more generalized set of by considering the following additions,

- **Space-Charge Potential Distribution:** It was obtained as a result of an quasi equilibrium between charge diffusion due to localized concentration gradients, Coulombic interactions, and thermal motion of ions. The convective motion was assumed to have negligible influence on the charge relaxation due to the above mentioned phenomena. This observation is valid for low concentration electrolytes which is common in the naturally occurring biological fluids. But for systems like ion exchange membranes, and near electrode surfaces, a complete solution of the charge transport equation (Nernst-Planck equation) might give further insights into ensuing the non-linearity of the system.
- **Two-liquid System:** Although gas-liquid systems occur in many real life systems as bubbles, foams, biological structures such as tear film, gas exchange in lung alveoli and blood capillaries, mucous lining on internal organs etc. Modeling a generalized two-liquid system will give a detailed insight into the stability of such interfaces while highlighting the role of density, viscosity and, permittivity gradients across the interface. A gas-liquid system can be considered as a limiting case of a two-liquid system undergoing interfacial dynamics.
- **Interfacial Dynamics:** The linear stability analysis provides the critical value of control parameters leading to neutral stability. Studying the interfacial growth and dynamics provides an interesting insight into film rupture and subsistence. Also, the use of frozen wave instability of polymer substrates in order to create precisely controlled patterned structures Verma et al. (2005), is a very interesting application of electrokinetic instability in dielectric liquids.

The experimental study of the interfacial instability of both miscible fluids and immiscible fluids provided interesting insights into the critical values of applied parameters such as magnitude and frequency of the electric field, applied flow rate and electrochemistry (e.g. ionic concentration, pH, conductivity etc.) of the system.on interfacial instability. Considering the wide range of involved parameters which are sensitive to the changes in the environmental conditions, following steps can be performed to reduce the experimental error and explore the interfacial stability in a greater detail,

- **Microchannel Fabrication:** Use of hard materials like glass microchannels to reduce the geometric variations in the channel profile. Also, the glass zeta

potential has been found to be more consistent and uniform, which helps to validate experimental results with theoretical results much easily.

- **More precise variation of parameters:** Most of the parametric variations such as the magnitude and frequency of the electric field and flow rate were manually controlled. In order to have a more precise variation of the control parameters, a computer controlled parametric variation can be used.
- **Feedback Control and Device Calibration:** Since all fluid and electric connections are exposed to losses some of which are head loss, potential loss etc. A feedback based parametric control can be established in order to minimize losses in the tubing and electrode connections leading to the microchannel.

Bibliography

Bazant, M., Thornton, K., Ajdari, A., 2004. Diffuse-charge dynamics in electrochemical systems. Phys. Rev. E 70, 021506.

Bird, R.B., Stewart, W.E., Lightfoot, E.N., 2007. Transport Phenomena. 2nd ed., John Wiley & Sons, New York.

Borukhov, I., Andelman, D., Orland, H., 1995. Polyelectrolyte Solutions between Charged Surfaces. Europhys. Lett. 32, 499–504.

Bose, N., Das, T., Chakraborty, D., Maiti, T.K., Chakraborty, S., 2012. Enhancement of static incubation time in microfluidic cell culture platforms exploiting extended air-liquid interface. Lab Chip 12, 69–73.

Brevis, W., Niño, Y., Jirka, G.H., 2010. Integrating cross-correlation and relaxation algorithms for particle tracking velocimetry. Exp. Fluids 50, 135–147.

Campbell, C.J., Grzybowski, B.A., 2004. Microfluidic mixers: from microfabricated to self-assembling devices. Philos. Trans. A. Math. Phys. Eng. Sci. 362, 1069–86.

Cash, J.R., Moore, G., Wright, R.W., 2001. An automatic continuation strategy for the solution of singularly perturbed nonlinear boundary value problems. ACM Trans. Math. Softw. 27, 245–266.

Cetin, B., Li, D., 2008. Effect of Joule heating on electrokinetic transport. Electrophoresis 29, 994–1005.

Chakraborty, J., Ray, S., Chakraborty, S., 2012. Role of streaming potential on pulsating mass flow rate control in combined electroosmotic and pressure-driven microfluidic devices. Electrophoresis 33, 419–25.

Chakraborty, S., Ray, S., 2008. Mass flow-rate control through time periodic electroosmotic flows in circular microchannels. Phys. Fluids 20, 083602.

Chakraborty, S., Srivastava, A.K., 2007. Generalized model for time periodic electroosmotic flows with overlapping electrical double layers. Langmuir 23, 12421–8.

CHEN, C.H., LIN, H., LELE, S.K., Santiago, J.G., 2005. Convective and absolute electrokinetic instability with conductivity gradients. J. Fluid Mech. 524, 263–303.

Choi, W., Sharma, A., Qian, S., Lim, G., Joo, S., 2010. Is free surface free in micro-scale electrokinetic flows? J. Colloid Interface Sci. 347, 153–5.

Choi, W., Sharma, A., Qian, S., Lim, G., Joo, S., 2011. On steady two-fluid electroosmotic flow with full interfacial electrostatics. J. Colloid Interface Sci. 357, 521–6.

Craster, R.V., Matar, O.K., 2009. Dynamics and stability of thin liquid films. Rev. Mod. Phys. 81, 1131–1198.

Davis, S.H., 1976. The Stability of Time-Periodic Flows. Annu. Rev. Fluid Mech. 8, 57–74.

Debye, P., Huckel, E., 1923. Zur Theorie der Elektrolyte. I. Gefrierpunktserniedrigung und verwandte Erscheinungen. Phys. Zeitschrift 24, 185–206.

Deshmukh, S., Vlachos, D., 2005. Novel micromixers driven by flow instabilities: Application to post-reactors. AIChE J. 51, 3193–3204.

Dufreche, J., Bernard, O., Turq, P., 2005. Transport in electrolyte solutions: are ions Brownian particles? J. Mol. Liq. 118, 189–194.

Dutta, P., Beskok, A., 2001. Analytical Solution of Time Periodic Electroosmotic Flows: Analogies to Stokes' Second Problem. Anal. Chem. 73, 1979–1986.

Favati, P., Lotti, G., Romani, F., 1991. Algorithm 691- Improving QUADPACK automatic integration routines. ACM Trans. Math. Softw. 17, 218–232.

Fedorov, M.V., Kornyshev, A.A., 2008. Towards understanding the structure and capacitance of electrical double layer in ionic liquids. Electrochim. Acta 53, 6835–6840.

Gao, Y., Wong, T., Yang, C., 2005a. Transient two-liquid electroosmotic flow with electric charges at the interface. Colloids Surfaces A 266, 117–128.

Gao, Y., Wong, T.N., Yang, C., Ooi, K.T., 2005b. Two-fluid electroosmotic flow in microchannels. J. Colloid Interface Sci. 284, 306–14.

Gonzalez, A., Ramos, A., Green, N., Castellanos, A., Morgan, H., 2000. Fluid flow induced by nonuniform ac electric fields in electrolytes on microelectrodes. II. A linear double-layer analysis. Phys. Rev. E 61, 4019–28.

Good, N., Winget, G., Winter, W., 1966. Hydrogen ion buffers for biological research. Biochemistry 5, 467–477.

Graciaa, A., Morel, G., Saulner, P., Lachaise, J., Schechter, R., 1995. The ζ-Potential of Gas Bubbles. J. Colloid Interface Sci. 172, 131–136.

Gray-Weale, A., Beattie, J.K., 2009. An explanation for the charge on water's surface. Phys. Chem. Chem. Phys. 11, 10994–11005.

Green, N.G., Ramos, A., Gonzalez, A., Morgan, H., Castellanos, A., 2000. Fluid flow induced by nonuniform ac electric fields in electrolytes on microelectrodes. I. Experimental measurements. Phys. Rev. E 61, 4011–8.

Griffiths, S.K., Nilson, R.H., 2006. Charged species transport, separation, and dispersion in nanoscale channels: autogenous electric field-flow fractionation. Anal. Chem 78, 8134–41.

Guillot, P., Colin, A., 2005. Stability of parallel flows in a microchannel after a T junction. Phys. Rev. E 72, 066301.

Guillot, P., Colin, A., Utada, A., Ajdari, A., 2007. Stability of a Jet in Confined Pressure-Driven Biphasic Flows at Low Reynolds Numbers. Phys. Rev. Lett. 99, 1–4.

Haiwang, L., Wong, T.N., Nguyen, N.T., 2010. Time-dependent model of mixed electroosmotic/pressure-driven three immiscible fluids in a rectangular microchannel. Int. J. Heat Mass Transf. 53, 772–785.

Hashimoto, M., Garstecki, P., Stone, H.a., Whitesides, G.M., 2008. Interfacial instabilities in a microfluidic Hele-Shaw cell. Soft Matter 4, 1403.

Israelachvili, J., 2011. Intermolecular and Surface Forces. 3rd ed., Elsevier.

Jang, J.H., Yoon, S., Ka, B.H., Jung, Y.H., Oh, S.M., 2005. Complex Capacitance Analysis on Leakage Current Appearing in Electric Double-layer Capacitor Carbon Electrode. J. Electrochem. Soc. 152, A1418.

Joo, S., 2008. A new hydrodynamic instability in ultra-thin film flows induced by electro-osmosis. J. Mech. Sci. Technol. 22, 382–386.

Kim, H., Bankoff, S.G., Miksis, M.J., 1992. The effect of an electrostatic field on film flow down an inclined plane. Phys. Fluids A Fluid Dyn. 4, 2117.

Kirby, B.J., Hasselbrink, E.F., 2004a. Zeta potential of microfluidic substrates: 1. Theory, experimental techniques, and effects on separations. Electrophoresis 25, 187–202.

Kirby, B.J., Hasselbrink, E.F., 2004b. Zeta potential of microfluidic substrates: 2. Data for polymers. Electrophoresis 25, 203–13.

Kötz, R., 2000. Principles and applications of electrochemical capacitors. Electrochim. Acta 45, 2483–2498.

Lambert, J.D., 1992. Numerical Methods for Ordinary Differential Systems. Wiley, New York.

Lasheras, J.C., Hopfinger, E.J., 2000. Liquid Jet Instability and Atomization in a Coaxial Gas Stream. Annu. Rev. Fluid Mech. 32, 275–308.

Lee, J.S.H., Barbulovic-Nad, I., Wu, Z., Xuan, X., Li, D., 2006. Electrokinetic flow in a free surface-guided microchannel. J. Appl. Phys. 99, 054905.

Lee, J.S.H., Li, D., 2006. Electroosmotic flow at a liquid-air interface. Microfluid. Nanofluidics 2, 361–365.

Li, C., Somasundaran, P., 1991. Reversal of bubble charge in multivalent inorganic salt solutions-Effect of magnesium. J. Colloid Interface Sci. 146, 215–218.

Li, X., Ballerini, D.R., Shen, W., 2012. A perspective on paper-based microfluidics: Current status and future trends. Biomicrofluidics 6, 11301–1130113.

Lin, H., 2009. Electrokinetic instability in microchannel flows: A review. Mech. Res. Commun. 36, 33–38.

Lorenz, C.D., Travesset, A., 2007. Charge inversion of divalent ionic solutions in silica channels. Phys. Rev. E 75, 061202.

Lyklema, J., 2001. Fundamentals of Interface and Colloid Science Vol II: Solid-Liquid Interfaces. Academic Press, London.

Malik, N., Dracos, T., Papantoniou, D., 1993. Particle tracking velocimetry in three-dimensional flows. Exp. Fluids 15-15.

Manciu, M., Ruckenstein, E., 2012. Ions near the air/water interface: I. Compatibility of zeta potential and surface tension experiments. Colloids Surfaces A Physicochem. Eng. Asp. 400, 27–35.

Mayur, M., Amiroudine, S., Lasseux, D., 2012. Free-surface instability in electro-osmotic flows of ultrathin liquid films. Phys. Rev. E 85, 046301.

Melcher, J.R., 1981. Continuum Electromechanics. MIT Press.

Oddy, M.H., Santiago, J.G., 2005. Multiple-species model for electrokinetic instability. Phys. Fluids 17, 064108.

Oddy, M.H., Santiago, J.G., Mikkelsen, J.C., 2001. Electrokinetic instability micromixing. Anal. Chem 73, 5822–5832.

Oron, A., Bankoff, S.G., 1997. Long-scale evolution of thin liquid films. Rev. Mod. Phys. 69, 931–980.

Pascall, A.J., Squires, T.M., 2011. Electrokinetics at liquid/liquid interfaces. J. Fluid Mech. 684, 163–191.

Persat, A., Chambers, R.D., Santiago, J.G., 2009a. Basic principles of electrolyte chemistry for microfluidic electrokinetics. Part I: Acid-base equilibria and pH buffers. Lab Chip 9, 2437–53.

Persat, A., Suss, M.E., Santiago, J.G., 2009b. Basic principles of electrolyte chemistry for microfluidic electrokinetics. Part II: Coupling between ion mobility, electrolysis, and acid-base equilibria. Lab Chip 9, 2454–69.

Posner, J.D., Santiago, J.G., 2006. Convective instability of electrokinetic flows in a cross-shaped microchannel. J. Fluid Mech. 555, 1.

Qian, S., Joo, S.W., Jiang, Y., Cheney, M.a., 2009. Free-surface problems in electrokinetic micro- and nanofluidics. Mech. Res. Commun. 36, 82–91.

Ramos, A., Morgan, H., Green, N., Castellanos, A., 1999. AC Electric-Field-Induced Fluid Flow in Microelectrodes. J. Colloid Interface Sci. 217, 420–422.

Ramos, A., Morgan, H., Green, N.G., Gonzalez, A., Castellanos, A., 2005. Pumping of liquids with traveling-wave electroosmosis. J. Appl. Phys. 97, 084906.

Rubinstein, B., Leshansky, a., 2011. Rupture of thin liquid films: Generalization of weakly nonlinear theory. Phys. Rev. E 83, 1–13.

Russel, W.B., Saville, D.A., Schowalter, W.R., 1989. Colloidal Dispersions. Cambridge University Press, New York.

Sadiq, I.M.R., Joo, S., 2009. Weakly Nonlinear Stability Analysis of an Electro-Osmotic Thin Film Free Surface Flow. Microgravity Sci. Technol. 21, 331–343.

Santos, J., Storey, B.D., 2008. Instability of electro-osmotic channel flow with streamwise conductivity gradients. Phys. Rev. E 78, 1–10.

Saville, D.A., 1977. Electrokinetic Effects with Small Particles. Annu. Rev. Fluid Mech. 9, 321–337.

Schaeper, J.P., Sepaniak, M.J., 2000. Parameters affecting reproducibility in capillary electrophoresis. Electrophoresis 21, 1421–9.

Sharma, A., Jameel, A.T., 1993. Nonlinear Stability, Rupture, and Morphological Phase Separation of Thin Fluid Films on Apolar and Polar Substrates. J. Colloid Interface Sci. 161, 190–208.

Sheng, P., Wen, W., 2012. Electrorheological Fluids: Mechanisms, Dynamics, and Microfluidics Applications. Annu. Rev. Fluid Mech. 44, 143–174.

Shin, S.M., Kang, I.S., Cho, Y.K., 2005. Mixing enhancement by using electrokinetic instability under time-periodic electric field. J. Micromechanics Microengineering 15, 455–462.

Song, J., Kim, M.W., 2011. Excess charge density and its relationship with surface tension increment at the air-electrolyte solution interface. J. Phys. Chem. B 115, 1856–62.

Sounart, T.L., Baygents, J.C., 2007. Lubrication theory for electro-osmotic flow in a non-uniform electrolyte. J. Fluid Mech. 576, 139.

Squires, T., Messinger, R., Manalis, S., 2008. Making it stick: convection, reaction and diffusion in surface-based biosensors. Nat. Biotechnol. 26, 417–426.

Squires, T.M., Quake, S.R., 2005. Microfluidics: Fluid physics at the nanoliter scale. Rev. Mod. Phys. 77, 977–1026.

Stone, H.A., Stroock, A.D., Ajdari, A., 2004. Engineering Flows in Small Devices. Annu. Rev. Fluid Mech. 36, 381–411.

Takami, N., Ohsaki, T., Hasebe, H., Yamamoto, M., 2002. Laminated Thin Li-Ion Batteries Using a Liquid Electrolyte. J. Electrochem. Soc. 149, A9.

Tsao, C.W., DeVoe, D.L., 2008. Bonding of thermoplastic polymer microfluidics. Microfluid. Nanofluidics 6, 1–16.

Ugaz, V.V.M., Elms, R.D.R., Lo, R.C.R., Shaikh, F.F.a., Burns, M.M.a., 2004. Microfabricated electrophoresis systems for DNA sequencing and genotyping applications: current technology and future directions. Philos. Trans. A 362, 1105.

Verma, R., Sharma, A., Kargupta, K., Bhaumik, J., 2005. Electric field induced instability and pattern formation in thin liquid films. Langmuir 21, 3710–21.

Wei, D., Patey, G.N., 1991. Dielectric relaxation of electrolyte solutions. J. Chem. Phys. 94, 6795.

Xia, Y., Whitesides, G., 1998. Soft lithography. Annu. Rev. Mater. Sci. .

Xu, Z., Miao, J., Wang, N., Wen, W., Sheng, P., 2011. Maximum efficiency of the electro-osmotic pump. Phys. Rev. E 83, 066303.

Yang, C., Dabros, T., Li, D., Czarnecki, J., Masliyah, J.H., 2001. Measurement of the Zeta Potential of Gas Bubbles in Aqueous Solutions by Microelectrophoresis Method. J. Colloid Interface Sci. 243, 128–135.

Yih, C.S., 1963. Stability of Liquid Flow down an Inclined Plane. Phys. Fluids 6, 321.

Yossifon, G., Mushenheim, P., Chang, Y.C., Chang, H.c., 2009. Nonlinear current-voltage characteristics of nanochannels. Phys. Rev. E 79, 046305.

Zaltzman, B., Rubinstein, I., 2007. Electro-osmotic slip and electroconvective instability. J. Fluid Mech. 579, 173.

Zhang, D.L., Liu, S., Puerto, M., Miller, C.a., Hirasaki, G.J., 2006. Wettability alteration and spontaneous imbibition in oil-wet carbonate formations. J. Pet. Sci. Eng. 52, 213–226.

Zheng, Q., Wei, G.W., 2011. Poisson-Boltzmann-Nernst-Planck model. J. Chem. Phys. 134, 194101.